الجـــمـــهـــوريـــة الجـزائـريـة الديمـــقـراطيـة الـشـــعـبيـة

PEOPLE'S DEMOCRATIC REPUBLIC OF ALGERIA

وزارة التـــعـــليـــم العـــــالي والبــــحث العـــــلـــمـــي

MINISTRY OF HIGHER EDUCATION AND SCIENTIFIC RESEARCH

جــــــــــامعة سعيدة – د. الطاهر مولاي –

University of Saïda – Dr. Tahar Moulay –

Faculty of Mathematics, Computer Science and Telecommunications

DISSERTATION

Submitted in partial fulfillment of the requirements for the **Master's Degree in Telecommunications**

Specialty: Networks and Telecommunications

By: Miss. HALIMI Fatima
Miss. MOKEDDEM Khadidja

Design and Analysis of Electronically Tunable Multiband Microstrip Filter

Defended on June 17th, 2025, before the jury composed of:

Dr. BOUHMIDI Rachid	MCA	President
Dr. BOUBAKAR Hichem	MCB	Supervisor
Dr. BOURAS Bouhafs	MCA	Examiner

2024 / 2025

Dedication

To My Mother

Stand still, O Time — do you not see her near? The moon of all ages has come to us, smiling and clear. She leaves behind her the breath of life in grace, And in her hands, a thousand souls drift in silent chase.O sweet-eyed maiden,

why dost thou frown? Have you not glanced at eyes where dreams have flown? Time itself was honored to cradle your grace, And proud am I, born of a mother with a truthful face.

To my father,

To a father whom no quote could truly define, Nor could any verse his worth confine. My pillar, my light when paths grow dim, He is the virtue, the good, the world within him.

To my brothers,

Peace to those who cared for every hidden ache, Who were balm and healing for every heart that did break. Peace to my strength, my pride when times were grim, Who stood as shields when hope looked thin.

To my sisters

Peace to those who guarded love with silent might, Who were in our days like clouds bearing rain's delight. Peace to those who sowed good and walked away, Leaving behind a scent, a memory, a sacred ray. They were the flower of youth, the breeze of the soul, When longing surged, they made me whole. Peace to the balm that healed each fleeting scar, A gently remedy whether near or far.

To my respected supervisor, Professor Boubakar Hichem

I wrote timeless words of gratitude to a teacher in the field of diodes, praising Allah for his adaptation to the field, considering human needs.

To my dearest friends, Khadidja,Souad,Chahra,Mokhtaria,Meriam,Amel

Peace upon your souls, companions of my dreams, Your memory is a melody flowing in endless streams. And those stories that time shall never unweave, Remain etched in my heart, never to leave.

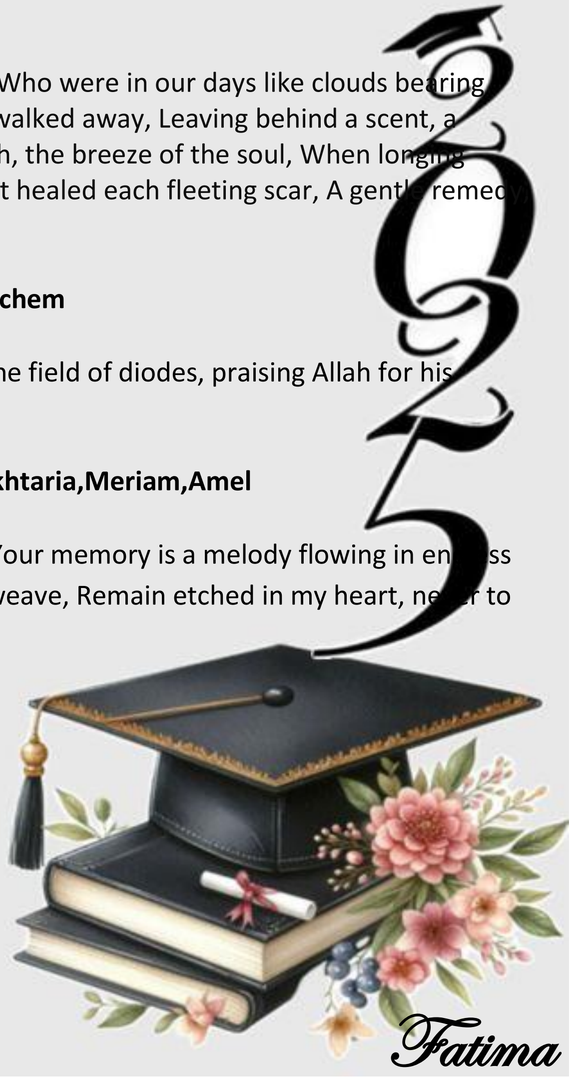

Dedication

In the Name of Allah, the Most Gracious, the Most Merciful. All praise is to Allah for the blessings of knowledge and success. This achievement is the fruit of my efforts and dedication in my Master's program in Telecommunications Networks, and I could not have succeeded without Allah's support and the encouragement of those who stood by me.

I dedicate my success to:

My beloved parents My dear mother and father, thank you for every moment of joy and unwavering support. You are the source of happiness in my life.

To My Two Dear and Beautiful Sisters Nesrine & Rajaa and My Little Brother Abdelmoumen

Thank you for every moment of love and encouragement. You are my strength and joy.

To my dear family (uncles, aunts, and cousins) Thank you! Your endless support and motivation turned my dream into reality.

To my dear grandparents To those still with us, may Allah bless you with long and healthy lives. To those who have passed, may Allah grant them mercy and the highest ranks in Paradise.

To my dear friends My companions on this journey and partners in countless memories—thank you for the laughter, support, and making this path brighter

.To my dear friend Fatima My research partner and late-night study companion, I dedicate this to you with deepest gratitude for every moment we shared.

To my honorable teachers From school to university, to all who taught me a word or guided me a step—may Allah reward you abundantly.

To my respected supervisor, Professor Boubakar Hichem With utmost respect and gratitude, I dedicate this research to you. Your invaluable guidance, patience, and expertise made this work possible. You have been an exceptional mentor—may Allah bless you immensely

And finally… to myself You worked hard, you grew tired, but you never gave up. Today, you reap the rewards of your patience and effort. Praise Allah, be grateful, savor this moment, and take pride in your success.

Lastly, To everyone who contributed to my journey—with a kind word, valuable advice, or even a simple smile—my deepest thanks to you all.

All praise is due to Allah, the Lord of the worlds, who blessed me with the completion of this work. To Him belongs all credit and favor, first and last.

Quranic Verse: "And say, 'Do [as you will], for Allah will see your deeds, and [so will] His Messenger and the believers.'" (At-Tawbah 9:105)

Quote: "Knowledge is the only good that cannot be measured except by itself." — Ibn Sina.

Khadidja

17.06.2025

Acknowledgments

I thank Almighty God for granting us the courage, will, and patience to complete this research.

We would like to especially thank my dissertation supervisor **Boubakar Hichem** Professor of Telecommunications at Dr. Moulay Tahar University, Saida. His continuous support was indispensable in completing our research. His patience was indispensable in completing our research. His valuable advice and professionalism were capable of guiding and enriching our thinking. It was very enjoyable to work with him. Collaborating with him on this project.

Thank you very much.

We thank all our comrades, and our gratitude. Finally, we thank all the teachers who taught us with all The dedication to get here.

Thank you very much.

Abstract

This dissertation addresses the demand for miniaturized and frequency-agile microwave components by presenting the design, optimization, and application of novel metamaterial unit cells culminating in an electronically reconfigurable microstrip stopband filter. The core innovation lies in a newly developed metamaterial unit cell, derived from the Split-Ring Resonator (SRR) concept but engineered for enhanced electrical length and superior compactness. Strategic integration of PIN diodes onto these cells enables dynamic control over the filter's operational frequency and mode, achieving reconfigurability while maintaining high performance and a compact physical footprint. The filter's efficacy is demonstrated through its ability to target distinct frequency bands (2.0 GHz, 2.5 GHz, and 3.6 GHz) via various diode switching combinations, showing significant potential for integration into modern wireless communication systems like 5G and IoT, as well as radar and satellite applications.

Keywords: stopband filter, microstrip, metamaterial, SRR, reconfigurability, PIN diodes.

ملخص

تعالج هذه الرسالة الطلب على مكونات الموجات الدقيقة المصغرة والقابلة لضبط التردد من خلال تقديم تصميم وتحسين وتطبيق خلايا وحدوية مبتكرة من المواد الميتا، تتوج بمرشح إيقاف نطاق شريطي دقيق قابل لإعادة التشكيل إلكترونيًا. يكمن الابتكار الأساسي في خلية وحدوية من المواد الميتا مطورة حديثًا، مشتقة من مفهوم مرنان الحلقة المنقسمة (SRR) ولكنها مصممة لطول كهربائي معزز واندماج فائق. يتيح التكامل الاستراتيجي لثنائيات PIN على هذه الخلايا التحكم الديناميكي في تردد التشغيل ونمط المرشح، مما يحقق قابلية إعادة التشكيل مع الحفاظ على أداء عالٍ وبصمة مادية مدمجة. تتجلى فعالية المرشح من خلال قدرته على استهداف نطاقات ترددية متميزة (2.0 جيجاهرتز، 2.5 جيجاهرتز، و 3.6 جيجاهرتز) عبر مجموعات مختلفة من تبديل الثنائيات، مما يُظهر إمكانات كبيرة للتكامل في أنظمة الاتصالات اللاسلكية الحديثة مثل الجيل الخامس (G5) وإنترنت الأشياء (IoT)، بالإضافة إلى تطبيقات الرادار والأقمار الصناعية.

كلمات مفتاحية: بمرشح إيقاف نطاق، شريط دقيق، المواد الميتا،SRR، إعادة التشكيل، الصمام الثنائي PIN.

Résumé

Ce mémoire répond à la demande de composants hyperfréquences miniaturisés et agiles en fréquence en présentant la conception, l'optimisation et l'application de nouvelles cellules unitaires de métamatériau, aboutissant à un filtre coupe-bande microruban électroniquement reconfigurable. L'innovation principale réside dans une cellule unitaire de métamatériau nouvellement développée, dérivée du concept de Résonateur en Anneau Fendu (SRR) mais conçue pour une longueur électrique améliorée et une compacité supérieure. L'intégration stratégique de diodes PIN sur ces cellules permet un contrôle dynamique de la fréquence opérationnelle et du mode du filtre, réalisant la reconfigurabilité tout en maintenant des performances élevées et une empreinte physique compacte. L'efficacité du filtre est démontrée par sa capacité à cibler des bandes de fréquences distinctes (2,0 GHz, 2,5 GHz et 3,6 GHz) via diverses combinaisons de commutation de diodes, montrant un potentiel significatif pour l'intégration dans les systèmes de communication sans fil modernes tels que la 5G et l'IoT, ainsi que dans les applications radar et satellitaires.

Mots clés : filtres coupe-bande, microruban, Métamatériau, SRR, reconfigurabilité, diodes PIN.

Table of Contents

Chapter III: Reconfigurable Metamaterial Stopband Filter

List of Figures

Chapter I: Background and theory of microwave filters

Chapter II: Metamaterials: an overview, process, and applications

Chapter III: Reconfigurable Metamaterial Stopband Filter

List of Tables

Chapter I: Background and theory of microwave filters

Chapter III: Reconfigurable metamaterial stopband filter

List of Abbreviations

4G: Fourth-Generation

5G: Fifth-Generation

6G: Sixth-Generation

BPF: Band-Pass Filter

BW: Bandwidth

CAD: Computer-Aided Design

CPW: Coplanar Waveguide

CRLH: Composite Right/Left-Handed (Transmission Line)

CSRR: Complementary Split-Ring resonators

CST: Microwave Studio

dB: Decibel

DNG: Double Negative

DPS: Double-Positive

ECM: Electronic Countermeasures

EM: Electromagnetic

ENG: Epsilon-Negative

FH: High cutoff frequency

FL: Low cutoff frequency

GCPW: Grounded Coplanar Waveguide

GHz: Gigahertz

GPS: Global Positioning System

HFSS: High-Frequency Structure Simulator

IoT: Internet of Things

IR: Infrared

LC: Inductance-Capacitance

LH: Left-Handed (Materials/Transmission Line)

LHM: Left-Handed Materials

MEMS: Micro-Electro-Mechanical Systems

MHz: Megahertz

MMIC: Monolithic Microwave Integrated Circuits

MMT: Metamaterials

mmWave: Millimeter-Wave

MNG: Mu-Negative

MRI: Magnetic Resonance Imaging

NRW: Nicolson-Ross-Weir

NWB BPF: Notched-Wideband Bandpass Filter

ON/OFF: Diode Biasing States

PIN: Positive-Intrinsic-Negative (Diode)

QA: Quality Factor (Loaded/Unloaded)

Quasi-TEM: Quasi-Transverse Electromagnetic

RC: Resistor-Capacitor

RF: Radio Frequency

RH: Right-Handed (Materials/Transmission Line)

RHM: Right-Handed materials

RHTL: Right-Handed Transmission Line

RLC: Resistor-Inductor-Capacitor

SBF: Stopband Filter

SI: Système International

SNR: Signal-to-Noise Ratio

S-Parameters: Scattering Parameters

SRR: Split-Ring Resonators

TE: Transverse Electric

TEM: Transverse Electromagnetic

THz: Terahertz

TL: Transmission line

TM: Transverse Magnetic

TR: Transition radiation

TZ: Transmission Zero

UV: Ultraviolet

WIFI: Wireless Fidelity

x-ray: X –radiation

General Introduction:

General introduction

Microwave frequencies (300 MHz – 300 GHz) form the foundation for essential modern technologies, including wireless communications, radar systems, and navigation. The effectiveness of these systems hinges on components that efficiently guide electromagnetic waves, often using planar guiding structures like microstrip or coplanar waveguides (CPW) due to their low manufacturing cost, compact size, and ease of integration [1].

Within microwave circuits, filters are critical two-port networks. They play an indispensable role in managing the crowded electromagnetic spectrum by selectively passing desired frequencies (passband) while rejecting unwanted ones (stopband), thereby isolating intended signals [2].

The drive for enhanced performance and device miniaturization has spurred significant interest in metamaterials – artificial structures engineered to exhibit electromagnetic properties not typically found in nature, such as negative permittivity and permeability [3]. Since their practical demonstration using elements like split-ring resonators (SRRs) [4, 5], metamaterials have offered a path towards significantly smaller RF components compared to conventional designs operating at the same frequency.

Furthermore, the rapid proliferation of RF systems necessitates frequency agility. Reconfigurable filters, capable of dynamically adjusting their frequency response, are crucial for developing multi-functional devices, enhancing radar capabilities for applications like electronic countermeasures (ECM), and enabling secure communication techniques like frequency hopping [6]. Electronic tuning is commonly achieved by integrating active components, such as PIN or varactor diodes, directly onto planar filter structures. Loading these components onto metamaterial-based filters has proven effective for tuning resonances or switching filter functions, combining the benefits of compact size with fast electronic control and seamless system integration [7].

This work directly addresses these converging trends by presenting the design and analysis of a novel, miniaturized stopband filter featuring both frequency and mode reconfigurability. Central to this innovation is a newly developed metamaterial unit cell, derived from the SRR concept but specifically engineered for enhanced electrical length and superior compactness compared to traditional designs. This optimized cell forms the basis of the stopband filter, which incorporates strategically placed PIN diodes acting as electronic switches to enable dynamic control over the filter's resonant characteristics and operational modes.

The subsequent chapters delve into the details of this research:

- Chapter 1 provides essential background, covering the fundamentals of microwave filters, the guiding technologies used in their design, and surveying existing approaches to reconfigurable filter implementations.
- Chapter 2 explores the field of metamaterials, including their historical development, core concepts, transmission line theory (RH, LH, CRLH), and notable applications.
- Chapter 3 presents the core contribution: the detailed design, simulation, analysis, and characterization of the proposed novel metamaterial unit cell and the resulting reconfigurable stopband filter incorporating PIN diodes for tuning.

References

[1] **R. E. Collin,** Foundations for Microwave Engineering, 2nd ed. Hoboken, NJ, USA: Wiley-IEEE Press, 2001.

[2] **J.-S. Hong and M. J. Lancaster,** Microstrip Filters for RF/Microwave Applications. New York, NY, USA: Wiley, 2001.

[3] **V. G. Veselago,** “The electrodynamics of substances with simultaneously negative values of ε and μ,” Sov. Phys. Uspekhi, vol. 10, no. 4, pp. 509–514, Apr. 1968, doi: 10.1070/PU1968V010N04ABEH003699.

[4] **J. B. Pendry, A. J. Holden, D. J. Robbins, and W. J. Stewart,** “Magnetism from conductors and enhanced nonlinear phenomena,” IEEE Transactions on Microwave Theory and Techniques, vol. 47, no. 11, pp. 2075–2084, 1999, doi: 10.1109/22.798002.

[5] **D. R. Smith, W. J. Padilla, D. C. Vier, S. C. Nemat-Nasser, and S. Schultz,** “Composite medium with simultaneously negative permeability and permittivity,” Physical Review Letters, vol. 84, no. 18, p. 4184, May 2000, doi: 10.1103/PhysRevLett.84.4184.

[6] **G. Goussetis, R. Lopez-Villarroya, E. Doumanis, O. S. Arowolo, and J. S. Hong,** “Quality factor of E-plane periodically loaded waveguide resonators and filter applications,” IET Microwaves, Antennas & Propagation, vol. 5, no. 7, pp. 818–822, May 2011, doi: 10.1049/IET-MAP.2010.0396.

[7] **A. K. Horestani, Z. Shaterian, J. Naqui, F. Martin, and C. Fumeaux,** “Reconfigurable and tunable S-shaped split-ring resonators and application in band-notched UWB antennas,” IEEE Transactions on Antennas and Propagation, vol. 64, no. 9, pp. 3766–3776, Sep. 2016, doi: 10.1109/TAP.2016.2585183.

CHAPITRE I:

Background and theory of microwave filters

I.1 Introduction

The rapid progress in science and technology has led to significant advancements in the design and miniaturization of passive microwave devices, such as filters, antennas, and duplexers. These devices are crucial in modern communication systems as they enhance electromagnetic properties while reducing component sizes. Recently, various new tunable devices with innovative shapes and techniques have been developed. These new structures offer an optimal solution for creating compact integrated circuits by replacing multiple components with a single device while maintaining equal or superior electromagnetic properties [I.1].

In this chapter, the history of the electromagnetic spectrum and the applications of each frequency band will be explored. Following this, a review of microwave transmission line theory and models will be presented [I.2]. Additionally, the theory of filters will be examined, focusing on their roles, classifications, and the different approximations used to realize these filters [I.3]. Finally, a comprehensive review and comparison will be provided of some of the latest proposed reconfigurable microstrip filters [I.4].

I.2. The electromagnetic spectrum

I.2.1. History

In 1831, the British scientist Faraday began a series of crucial experiments, he discovered the phenomenon of electromagnetic induction, proving to the world that changing the magnetic field will produce an electric field. The law of electromagnetic induction, which is a quantitative representation of this phenomenon, was also discovered by Faraday. Faraday found that if the magnetic field of an electromagnet was made to expand and contract by opening and closing the electrical circuit of which it was a component, an electrical current could be detected in another nearby conductor. Similarly, a wire coil could also induce a current while a permanent magnet was being moved in and out of it. Additionally, whenever a conductor was moved near a stationary permanent magnet and as long as it was in motion, a current flowed in the wire. In his later years, he demonstrated his profound physical ideas by proposing that the electromagnetic force not only exists in conductors, but also extends into nearby space [I.5]. James Clerk Maxwell began to study electromagnetism in 1855, and based on the achievements of his predecessors, through superb mathematical attainment and imagination, published three significant papers- “On Faraday's Lines of Force”, “On Physical Lines of Force”, “A dynamic theory of the electromagnetic field”. This systematic and comprehensive study of electromagnetic phenomena summarizes and summarizes the work of predecessors [I.6]. After being rewritten and organized, these three papers became classic electrodynamic theory. In 1865, Maxwell predicted the existence of electromagnetic waves and concluded through theoretical reasoning that electromagnetic waves can only be laterally conducted waves, and the propagation speed is equal to the speed of light. Maxwell also revealed the connection between light and electromagnetic phenomena, proving that light is a form of electromagnetic waves. In 1873, Maxwell published the well-known General Theory of Electromagnetism, which later deeply impressed the German physicist Heinrich Rudolf Hertz. Studied Maxwell's theory of electromagnetism and experimentally demonstrated the existence of electromagnetic waves in 1888. He also pointed out that electromagnetic waves can be reflected, refracted and polarized at the same speed as the speed of light [I.7]. From 1888 to the present, electromagnetic theory has been deepened and the field of application has been expanded. Electromagnetic waves are widely used as a very important natural resource, such as in medicine, daily life and military applications. In 1895, Russian scientist Popov invented the first wireless telegraph system. In the same year, Wilhelm Roentgen discovered X-ray. In 1914, voice communication became a reality. In 1920, commercial radio broadcasting began to be used. Radar was invented in the 30s of the 20th centuries, and radar and energy information developed rapidly in the 40s. In the 50s, the first artificial satellite was put into the sky, and the satellite communication industry developed rapidly.

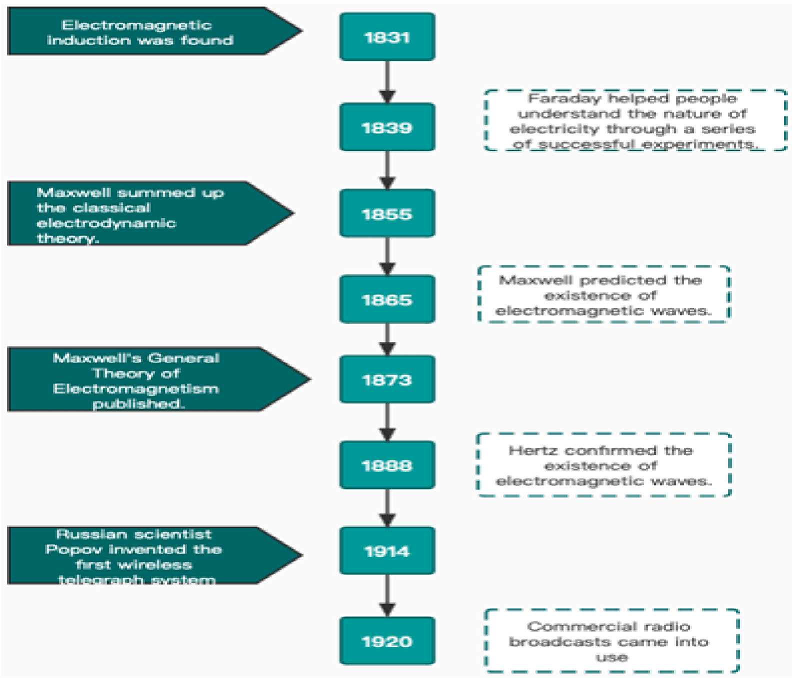

Figure I-1: Chronology of discoveries and developments in electromagnetism.

I.2.2. Electromagnetic waves

Electromagnetic waves may be characterized as oscillatory disturbances exhibiting phase synchrony, where electric and magnetic fields, orthogonal to each other in space, arise from the emission of oscillating particles. These waves propagate as fluctuations in the electromagnetic field, often exhibiting the phenomena of wave-particle duality through the propagation of photon particles [I.8]. However, the intricate relationship between the wave and particle aspects of these electromagnetic phenomena remains an area of active research, especially considering the distinct nature of each aspect. James Clerk Maxwell‘s contributions to electromagnetism have been lauded as „the second great unification in physics.“ Maxwell‘s seminal work integrated the then-disparate theories of electricity, magnetism, and optics, marking a significant advancement since Isaac Newton‘s unification of terrestrial and celestial mechanics. Maxwell‘s formulation of classical electrodynamics, particularly in his 1873 treatise, A Treatise on Electricity and Magnetism,“ laid the foundations for the modern understanding of electromagnetic fields. His introduction of the now-famed Maxwell‘s Equations systematically predicted the existence and properties of electromagnetic waves [I.9]. Electromagnetic waves share common traits with conventional waves, such as diffraction, interference, reflection, and refraction. Unlike mechanical waves, electromagnetic waves do not require a medium for propagation. Electromagnetic radiation within the visible spectrum, ranging from 380 to 780 nanometers, is emitted from objects at temperatures above absolute zero [I.10]. This radiation, perceived by humans as visible light, is a fundamental phenomenon, as the emission of such radiation is a prerequisite for the existence of life as we know it. The cessation of this radiation emission at temperatures equal to or below absolute zero would signify a state where traditional life forms could not exist.

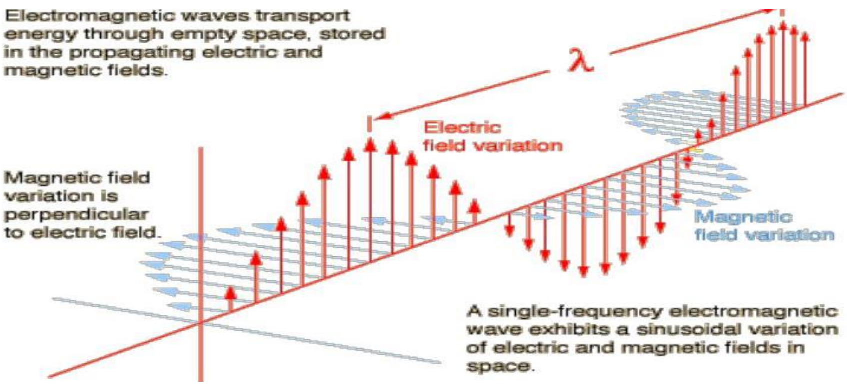

Figure I-2: Example of a plane electromagnetic wave.

I.2.3. Characteristics of electromagnetic waves

Electromagnetic waves are characterized by three primary attributes: intensity, which relates to the wave's amplitude and is perceived as brightness in visible light; frequency, corresponding to the wavelength and perceived as hue; and waveform, or spectral distribution, related to chromaticity. In the case of monochromatic light, such as that emitted by laser sources, the waveform closely approximates a sinusoidal (cosine) curve. The purity of the electromagnetic spectrum is enhanced as the waveform more closely resembles this sinusoidal shape, resulting in a more monochromatic output [I.11]. Further examination reveals the classification of electromagnetic waves based on their wavelengths, leading to diverse applications ranging from low-frequency radio broadcasting and television to nuclear radiation sources. These waves are integral to various aspects of modern life. In classical mechanics, a clear distinction is made between "pure" particles and fluctuations, typically matter and light waves. However, in quantum mechanics, without incorporating the principles of special relativity, it is posited that fundamental particles like photons, electrons, and protons can be described using the Schrödinger equation. The solution to this equation is represented by a wave function, whose absolute value squared denotes the probability density of a particle appearing at a specific location. More broadly, the wave function can be interpreted as the probability amplitude associated with an observation at a given location. These probability amplitudes, akin to waves, can interact through superposition, representing various pathways. The electromagnetic Spectrum is show in Figure I-3 [I.12].

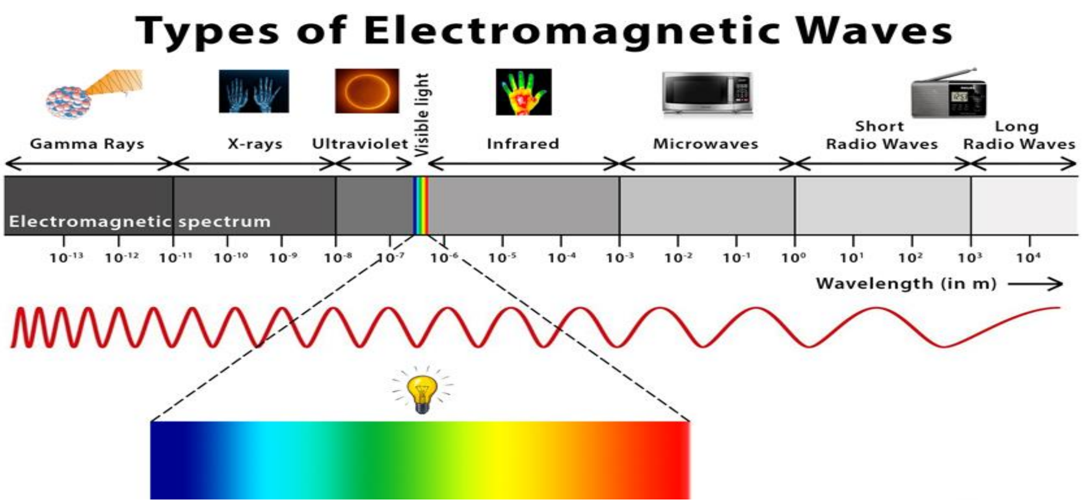

Figure I-3: Types of electromagnetic waves and electromagnetic spectrum.

The polarization, reflection, and refraction of electromagnetic waves are essential properties with significant implications across various fields . Polarization refers to the orientation of the electromagnetic wave‘s electric field vibrations, which can be linear, circular, or elliptical. This property finds applications in communication (including satellite systems), optics (such as polarized lenses for reducing glare), and astronomy (for studying radiation from celestial bodies) [I.13]. Reflection involves electromagnetic waves returning to their original medium upon encountering an interface, following the principle that the angle of incidence equals the angle of reflection. This phenomenon is critical in radar design, antenna planning, and constructing optical instruments like telescopes and microscopes. Refraction, the change in direction of electromagnetic waves due to velocity alterations when transitioning between different media, is governed by Snell‘s Law. This property is extensively utilized in optics (for manufacturing spectacles and telescopes) and communication technologies (such as fiber optic transmission). The implications of refraction are profound, impacting a wide range of applications from optical manufacturing to the design of fiber optic networks.

I.2.3.1. Field configuration

The general expressions for the electric $\vec{E}$ and magnetic fields $\overrightarrow{H}$ in waves that participate in the TR process (see, e.g., [I.14, I.15]), and represent them in the unified form suitable for the further consideration. Let us consider a general model of the EW formation due to the TR of a monochromatic light wave with frequency ω where the electric and magnetic fields behave in time as Re [E exp $(-\mathrm{i}\ \omega t)$] , Re [H exp $(-\mathrm{i}\ \omega t)$]. Let the incident plane wave come from the lower half-space z < 0 (medium 1) with dielectric and magnetic constants ε_1, $\mu_1$and refraction index $n_1 = \sqrt{\mu_1 \varepsilon_1}$, and the boundary z = 0 separates it from the medium 2 (z > 0) with parameters ε_2, μ_2 and $n_2 = \sqrt{\mu_2 \varepsilon_2}$ (see Figure I-4). The wave direction is specified by the wave vector $k_1 = k_1(sin\theta_1 , 0, cos\theta_1)^T, \theta_1$ is the angle of incidence, $k_1 = n_1(\omega/c)$and $k_2 = n_2(\omega/c)$are the wavenumbers in media 1 and 2, respectively, c is the light velocity in vacuum(n = 1 for vacuum, approximately 1.00029 for air under normal conditions, 1.33 for water, and between 1.5 and 1.7 for glass).

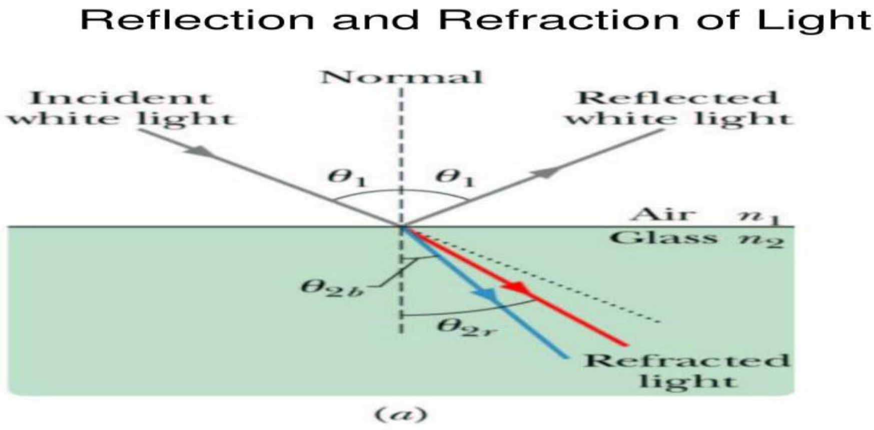

Figure I-4: Refraction of an electromagnetic wave during the passage from medium 1 to medium 2.

Descartes' laws of refraction describe this process:

- **First Law**: The refracted ray lies in the plane of incidence.
- **Second Law**: The relationship for the incidence angle θ_1 and refraction angle θ_1 is:

$$n_1\, sin(\theta_1) = n_2\, sin(\theta_2) \tag{I.1}$$

I.2.4. Field of application of electromagnetic waves

The electromagnetic spectrum (EM) comprises all electromagnetic radiation that can be represented in a corpuscular way as photons or wavily as electromagnetic waves. The electromagnetic spectrum is divided into frequency, wavelength, and energy scales. This continuum technically ranges from zero to infinity (in frequency or in wavelength), with no discontinuity. The electromagnetic radiations that comprise the electromagnetic spectrum are numerous and have various: names, bands, and uses, such as radio waves or Hertzian waves, microwaves, terahertz, infrared radiation, visible light, ultraviolet rays, x-rays, and gamma rays [I.16].

Starting with the most energetic waves, we successively distinguish:

- **Gamma rays (γ)**: these are high-energy rays that emitted radiations from radioactive decay of an unstable nucleus in radioactive elements. It has the shortest wavelengths that range from 10^{-14} m to 10^{-12} m.
- **X-rays:** these rays are known to use in medicine, but they have other applications for example in baggage control in airports. Some scientific research applications like the study of matter. This X-rays radiation covers the wavelengths included between 10^{-12} m and 10^{-8} m.
- **Ultraviolet rays:** these rays' sources are mostly natural, meaning from the

sun and the stars. These rays have considerable energy. Their wavelengths range from 10^{-8} m to 4.10^{-7} m.

- **The visible range:** This narrow part of the EM spectrum is the one that is visible. The wavelength range corresponds to it is around the values [400 nm; 800 nm].
- **Infrared:** In general, all heated bodies emit infrared radiation, even though they are not visible. Their applications include measuring the temperature of ground and ocean surfaces, as well as the temperature of clouds. Cover them with wavelengths ranging from 8.10^{-7} m to a millimeter (10^{-3} m) to one meter. All of the above devices and systems will have a specific band to operate within, and all of these bands fall within the microwave spectrum.
- **Radio waves:** This electromagnetic radiation part is the broadest of the electromagnetic spectrum and is concerned with the waves of the lowest wavelength. Its wavelengths range from a few meters to several kilometers. Radio waves are used for information transmission because they are relatively easy to issue and receive (radio, television, and telephone).

I.3. The theory of transmission line and its modeling

Transmission line (TL) theory can be considered a simplified and consistent framework within general electromagnetic theory, so the governing equations of the line and their solutions can be viewed as more tractable and understandable versions of their corresponding electromagnetic counterparts [I.17]. This is particularly appealing for undergraduate students in electrical engineering since the vector nature of the field vanishes, and the propagation phenomenon in the line can be understood in terms of forward and backward scalar voltage waves. The presentation of the Smith chart [I.18], [I.19] within this context gives a boost to this initial attraction since the chart beautifully replaces all complex calculations involved in TL analysis with mere geometrical considerations.

Any simplification process, however, usually veils the theory that underlies it. This is precisely what, in my opinion, usually happen s whenever an undergraduate student tries to match or relate the theoretical side of the problem, summarized in the extent formulae of TL theory, to its practical side, namely, the chart-based geometrical solution of electromagnetic problems [I.20]. The student does not perceive such relationships, leaving the theory apart, because doing so is considered useless when compared to the powerful chart. After years of lecturing on this subject, we have turned to very simple linear algebra ideas to fill this gap in such a way that the everlasting search for simplicity demanded by students and the teacher's aim to transmit the profound meaning of a subject can be simultaneously satisfied.

Regardless of the actual structure, a segment of uniform transmission line (i.e., a line with constant cross section along its length) as shown in Figure I-5 (a) can be modeled by the circuit shown in Figure I-5 (b) with

- ✓ **Resistance (R)**: Represents the energy loss due to the resistance of the conductors. It is usually expressed in ohms per unit length.
- ✓ **Inductance (L)**: Represents the magnetic field generated by the current flowing through the conductors. It is usually expressed in henries per unit length.
- ✓ **Capacitance (C)**: Represents the ability of the transmission line to store electric energy. It is usually expressed in farads per unit length.
- ✓ **Conductance (G)**: Represents the energy loss due to the dielectric material between the conductors. It is usually expressed in siemens per unit length.

Thus R, L, G and C are also referred to as resistance, inductance, conductance, and capacitance per unit length. (Sometimes p.u.l. is used as shorthand for per unit length.) In the metric system, Ohms per meter (Ω/m), Henries per meter (H/m), Siemens per meter (S/m) and Farads per meter (F/m), respectively, are used. The values of R, L, G and C are affected by the geometry of the transmission line and by the electrical properties of the dielectrics and conductors. C describes the ability to store electrical energy and is mostly due to the properties of the dielectric. G describes loss in the dielectric which derives from conduction in the dielectric and from dielectric relaxation. Most microwave substrates have negligible conductivity so dielectric relaxation loss dominates. Dielectric relaxation loss results from the movement of charge centers which result in distortion of the dielectric lattice (if a crystal) or molecular structure. The periodic variation of the E field transfers energy from the EM field to mechanical vibrations. R is due to ohmic loss in the metal more than anything else. L describes the ability to store magnetic energy and is mostly a function of geometry, as most materials used with transmission lines have μ_r =1 (so no more magnetic energy is stored than in a vacuum).

For most lines the effects due to L and C dominate because of the relatively low series resistance and shunt conductance. The propagation characteristics of the line are described by its loss-free, or lossless, equivalent line, although in practice some information about R or G is necessary to determine power

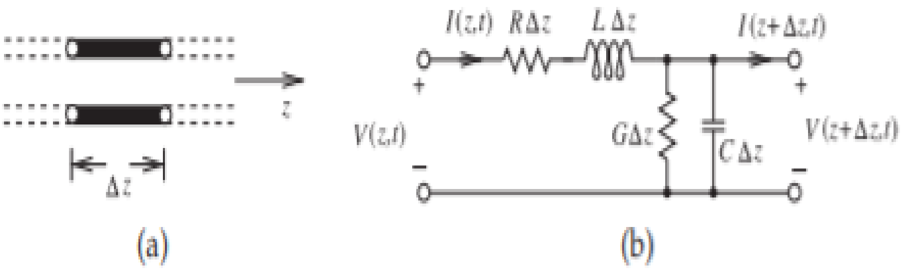

Figure I-5: Transmission line segment: (a) of length Δz; and (b) lumped-element model.

Losses. The lossless concept is just a useful and good approximation [I.21].

Different types of transmission lines have been developed to meet specific requirements in Figure I-6:

Stripline is quite bulky as it involves two ground planes.

The coplanar line (CPW) [I.22] has three metallic bands and two slots: a signal conductor separated by an air gap from two ground lines. A variant of this line is the coplanar line with a lower ground plane (GCPW) [I.23].

The slot line [I.24] consists of two conductors forming the transmission line, which are deposited on the same face of the dielectric substrate.

The microstrip line [I.25] (also known as microband or microstrip) features a dielectric substrate with a metallized back side (the ground plane) and a metallized circuit on the front side.

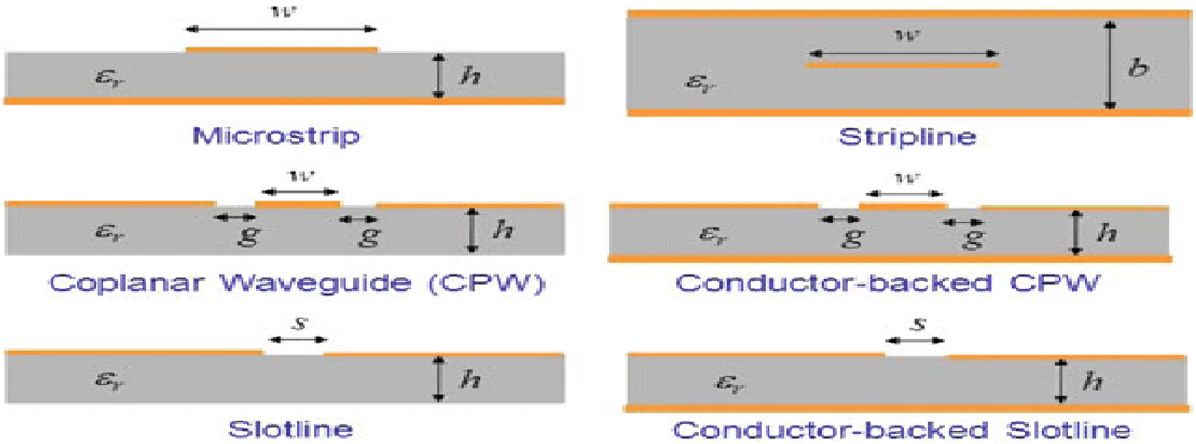

Figure I-6: The different types of planar lines.

We will focus more specifically on microstrip lines and coplanar lines, which will be used to excite our systems. At high frequencies, these lines will be treated in a specific manner to prevent parasitic modes that may arise. The major drawbacks of these lines compared to waveguides are the maximum power they can support and the insertion losses they cause.

I.3.1. Derivation of transmission line properties

In this section the differential equations governing the propagation of signals on a transmission line are derived. These are coupled first-order differential equations and are akin to Maxwell's Equations in one dimension. Solution of the differential equations describes how signals propagate, and leads to the extraction of a few parameters that describe transmission line properties.

Applying Kirchhoff's laws applied to the model in Figure I-7 and taking the limit as $\Delta z \rightarrow 0$ the transmission line equations are

$$\frac{\partial V(z,t)}{\partial z} + L\frac{\partial I(z,t)}{\partial z} + RI(z,t) = 0 \qquad (I.2)$$

$$\frac{\partial I(z,t)}{\partial z} + C\frac{\partial V(z,t)}{\partial z} + GV(z,t) = 0 \qquad (I.3)$$

V(z) is a phasor and $V(z,t) = \Re\{V(z)e^{j\omega t}\}$. $\Re\{\omega\}$.denotes the real part of ω , a complex number In sinusoidal steady-state using cosine-based phasors these become

$$\frac{\partial V(z)}{\partial z} = -(R + j\omega L)I(z) \qquad (I.4)$$

And

$$\frac{\partial I(z)}{\partial z} = -(G + j\omega C)V(z) \qquad (I.5)$$

Eliminating $I(z)$ in the above yields the wave equation for $V(z)$

$$\frac{\partial V(z)^2}{\partial z} - \gamma^2 V(z) = 0 \qquad (I.6)$$

Similarly

$$\frac{\partial I(z)^2}{\partial z} - \gamma^2 I(z) = 0 \qquad (I.7)$$

Where the propagation constant is

$$\gamma = \alpha + j\beta \qquad (I.8)$$

with SI units of m^{-1} and where α is the attenuation coefficient and has units of Nepers per meter (Np/m), and β is the phase-change coefficient, or phase constant, and has units of radians per meter (expressed as rad/m or radians/m) Nepers and radians are dimension less units, but serve as prompts for what is being referred to [I.21].

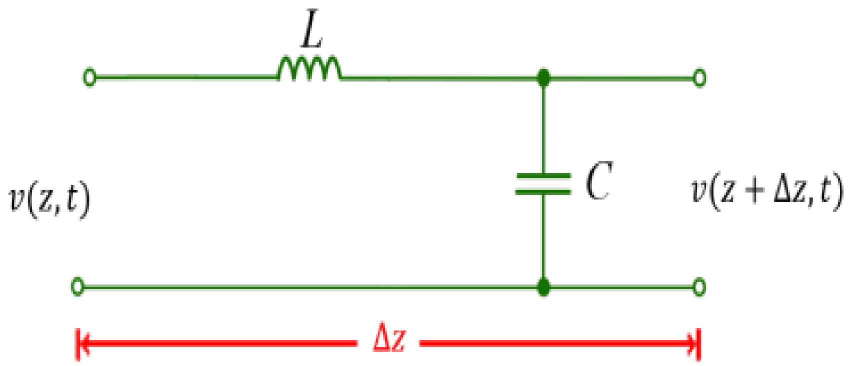

Figure I-7: Equivalent circuit of a transmission line.

I.3.2. Coplanar lines

The coplanar waveguide (CPW) is composed of a conductor and two ground planes located on each side of the conductor with a separation, mounted on a dielectric on the same plane [I.26].

I.3.2.1. Structure

- **Central conducting strip**: The primary conductor that carries the signal.
- **Ground planes**: Two conductive planes placed on either side of the central strip, providing a return path for the signal.
- **Dielectric substrate**: The insulating material on which the central strip and ground planes are placed [I.1].

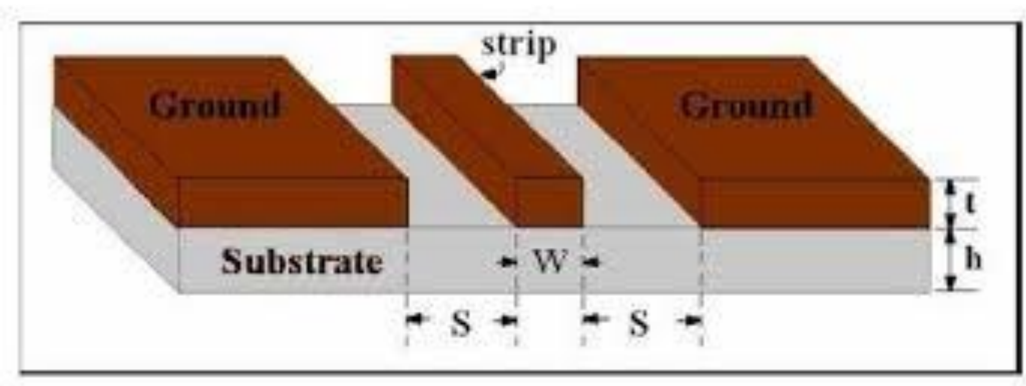

Figure I-8: A cross section of a coplanar line

The coplanar line is widely used as a transmission line in monolithic microwave integrated circuits (MMICs) due to its electromagnetic and technological properties. With the miniaturization of circuits and their increasing frequency, the use of MMIC devices proves to be relevant. In the context of characterization techniques, particularly for transmission line methods, the coplanar line generates significant interest because it serves as a measurement cell. Indeed, the coplanar line facilitates a simple method for electromagnetic characterization of thin-film materials since the line itself becomes a measurement cell directly integrating the sample.

To establish the electromagnetic behavior of the coplanar line, its S-parameters (reflection parameters S11 and S22; transmission parameters S12 and S21) are determined within the desired frequency range (up to 110 GHz). These parameters are measured using a vector network analyzer, allowing us to determine, from analytical relations, the propagation constant and the characteristic impedance of the coplanar line. Consequently, we can deduce the electromagnetic properties of the substrate or a thin-film material placed between the substrate and the coplanar line.

The advantage of this type of line is that it offers broadband characterization and is well-suited for thin-film measurements. Additionally, the coplanar line is a waveguide that is easy to manufacture, incurs low technological costs, and operates in a quasi-TEM mode with minimal dispersion, despite the medium's non-homogeneity (air + substrate). This means that the electric and magnetic fields can be considered perpendicular to the axis of the line along which propagation occurs. The dimensions of the line can be optimized to propagate the dominant mode (quasi-TEM) [I.27] and achieve better accuracy of the measured S-parameters (Figure I-9).

To validate our analytical model for extracting electromagnetic properties, we chose to create coplanar lines on an Alumina substrate, whose characteristics are as follows [I.28].

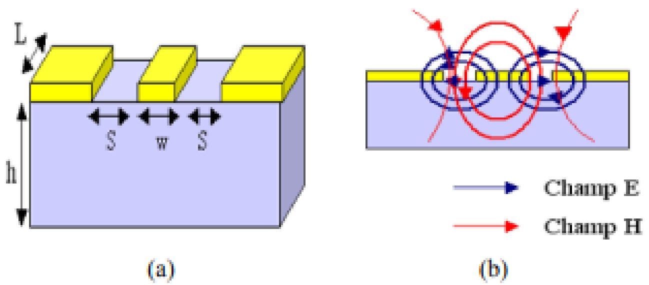

Figure I-9: Coplanar line (a) and distribution of electric and magnetic field lines (b).

I.3.2.2.Applications

- **Filters:** Coplanar lines can be applied to filters [I.29].
- **Adapting impedance:** Coplanar lines can be used in networks for impedance adaptation.
- **Power dividers**: Coplanar lines can be applied to power dividers.
- **Directional couplers**: Coplanar lines can be used in directional couplers.
- **Choke circuits:** Coplanar lines can be applied to choke circuits that induce polarization of active components.
- **Measurement cell:** Coplanar lines can be used as a measurement cell that directly integrates the sample for simple electromagnetic characterization of thin-layer materials [I.28].

I.3.2.3. Advantages

The advantages of the coplanar line are the possibility of characterization over a wide frequency range in a non-destructive manner and a topology suitable for thin film structures. Moreover, the coplanar line is an easy-to-manufacture waveguide that incurs low technological costs and operates in a quasi-TEM mode, which is not very dispersive despite the non-homogeneity of the medium (air + substrate), meaning that the electric and magnetic fields are perpendicular to the axis of the line along which propagation occurs. Figure I-10 illustrates a coplanar line as well as its equivalent electrical circuit for a line element of infinitesimal length. It is possible to optimize the dimensions of the line (substrate thickness > central strip width + 2 times.

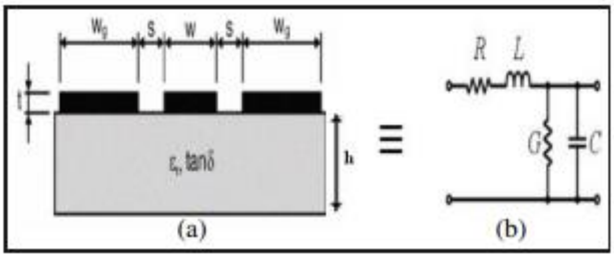

Figure I-10: Coplanar line (a) and its equivalent electrical circuit (b).

The slot separating the central strip and the ground plane) in order to propagate the dominant mode (quasi-TEM) [I.30], and to achieve better accuracy of the measured S parameters.

I.3.3. Microstrip lines

Microstrip line is one of the most popular types of planar transmission lines primarily because it can be fabricated by photolithographic processes and is easily miniaturized and integrated with both passive and active microwave devices. The geometry of a microstrip line is shown in Figure I-11(a). A conductor of width W is printed on a thin, grounded dielectric substrate of thickness d and relative permittivity ε_r ; a sketch of the field lines is shown Figure I-11(b).

If the dielectric substrate were not present (ε_r= 1), we would have a two-wire line consisting of a flat strip conductor over a ground plane, embedded in a homogeneous medium (air). This would constitute a simple TEM transmission line with phase velocity v_p= c and propagation constant $\beta = k_0$.

The presence of the dielectric, particularly the fact that the dielectric does not fill the region above the strip (y > d), complicates the behavior and analysis of microstrip line.

Unlike stripline, where all the fields are contained within a homogeneous dielectric region, microstrip has some (usually most) of its field lines in the dielectric region between the strip conductor and the ground plane and some fraction in the air region above the substrate. For this reason microstrip line cannot support a pure TEM wave since the phase velocity of TEM fields in the dielectric region would $c/\sqrt{\varepsilon_r}$, while the phase velocity of TEM fields in the air region would be c, so a phase-matching condition at the dielectric–air interface would be impossible to enforce.

In actuality, the exact fields of a microstrip line constitute a hybrid TM-TE wave and require more advanced analysis techniques than we are prepared to deal with here. In most practical applications, however, the dielectric substrate is electrically very thin (d << λ), and so the fields are quasi-TEM. In other words, the fields are essentially the same as those of the static (DC) case. Thus, good approximations for the phase velocity, propagation con-stant, and characteristic impedance can be obtained from static, or quasi-static, solutions.

Then the phase velocity and propagation constant can be expressed as

$$v_p = \frac{c}{\sqrt{\varepsilon_e}} \tag{I.9}$$

$$\beta = k_0\sqrt{\varepsilon_e} \tag{I.10}$$

Where ε_e is the effective dielectric constant of the microstrip line. Because some of the field lines are in the dielectric region and some are in air, the effective dielectric constant satisfies the relation [I.1].

$$1 < \varepsilon_e < \varepsilon_r \qquad (I.11)$$

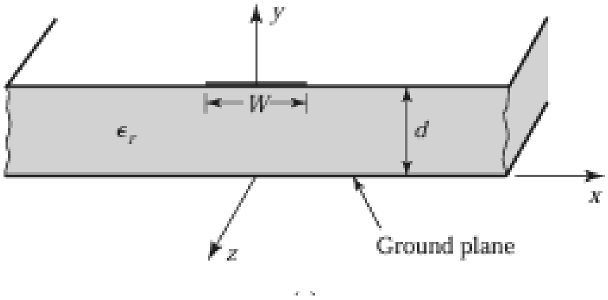

(a)

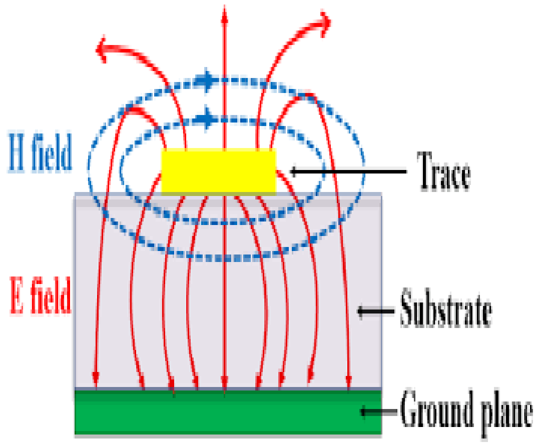

(b)

Figure I-11: Microstrip transmission line. (a) Geometry. (b) Electric and magnetic field lines.

I.4. Modeling of the transmission line

Transmission line model refers to modeling the distributed nature of electrical transmission lines using circuits consisting of lumped parameter elements. An accurate transmission line consists of continuously distributed parameters like resistance, inductance, capacitance, and conductance along the line.

The transmission line is modelled with a resistance (R) and inductance (L) in series with a capacitance (C) and conductance (G) in parallel. The resistance and conductance contribute to the loss in a transmission line [I.31].

I.4.1. Distributed parameter model

For a lossy transmission line, we parameterize the distributed circuit in terms of a resistance (R) inductance (L), capacitance(C), and conductance (G) per unit length.

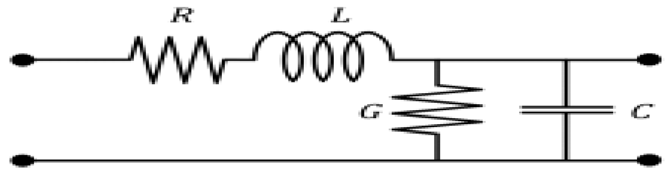

Figure I-12: The distributed circuit for a transmission line modeled by a resistance (R), inductance (L), capacitance(C), and conductance (G) per unit length.

In the most general sense R, L, C and G depend on frequency (Fig. I-12). Applying Kirchhoff's point and loop rules to Figure I-12, we obtain the Telegrapher's equations,

$$\frac{\partial}{\partial x}\tilde{V}(x) = -L\frac{\partial}{\partial t}\tilde{I}(x) - R\tilde{I}(x) \quad (\text{I}.12)$$

$$\frac{\partial}{\partial x}\tilde{I}(x) = -C\frac{\partial}{\partial t}\tilde{V}(x) - G\tilde{V}(x) \quad (\text{I}.13)$$

Next, we assume a sinusoidal time dependence,

$$I(x,t) = \tilde{I}(x) = I(x)e^{j\omega t} \quad (\text{I}.14)$$

$$V(x,t) = \tilde{V}(x) = V(x)e^{j\omega t} \quad (\text{I}.15)$$

Then, we insert $(\text{I}.14)$ into $(\text{I}.15)$, and solve the wave equation to define the propagation constant,

$$\gamma = \sqrt{(R + j\omega L)}\sqrt{(G + j\omega C)} \quad (\text{I}.16)$$

And the characteristic impedance,

$$Z_0 = \sqrt{\frac{R+j\omega L}{G+j\omega C}} \quad (\text{I}.17)$$

Where ω is the angular frequency [I.32].

I.4.2. Smith chart

The Smith chart, shown in Figure I-13, is a graphical aid that can be very useful for solving transmission line problems. Although there are a number of other impedance and reflection coefficient charts that can be used for such problems [I.33], the Smith chart is probably the best known and most widely used. It was developed in 1939 by P. Smith at the Bell Telephone Laboratories [I.34]. The reader might feel that, in this day of personal computers and computer-aided design (CAD) tools, graphical solutions have no place in modern engineering. The Smith chart, however, is more than just a graphical technique. Besides being an integral part of much of the current CAD software and test equipment for microwave design, the Smith chart provides a useful way of visualizing transmission line phenomenon without the need for detailed numerical calculations. A microwave engineer can develop a good intuition about transmission line and impedance-matching problems by learning to think in terms of the Smith chart [I.1].

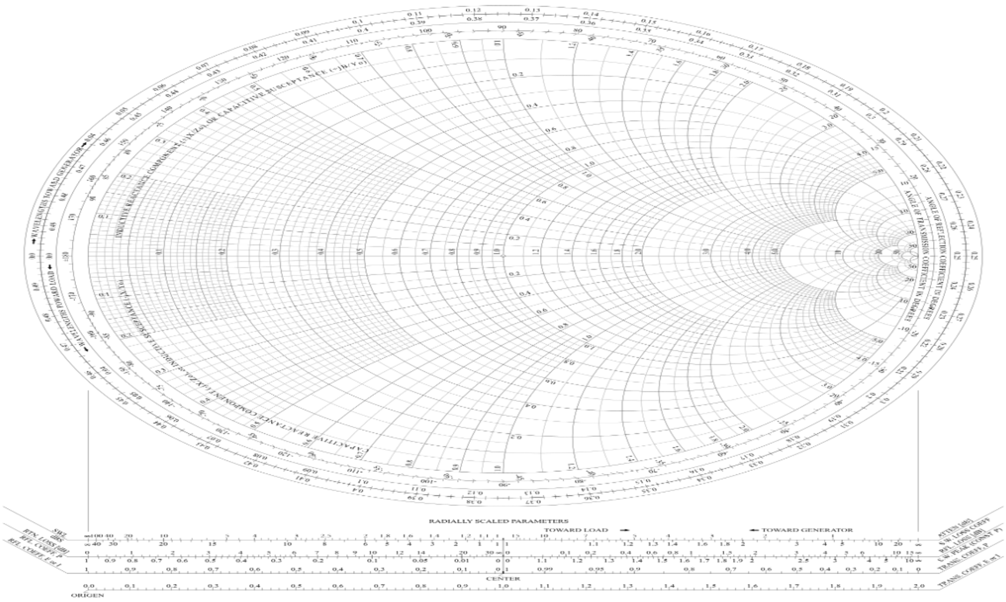

Figure I-13: The Smith chart.

I.5. Microwave filtering

Filtering is the action used to eliminate a frequency or a frequency band, or conversely, to favor a frequency or a frequency band. In other words, it is the action of modifying the spectral components of an electrical signal.

Filters are the most frequently used components in telecommunications, with their main application being the frequency multiplexing of signals.

The design of microwave filters is complex because the elements used have distributed parameters. There is no fully general synthesis method, and the frequency behavior of microwave circuit elements (such as transmission lines, cavities, etc.) is intricate, making it impossible to develop a comprehensive and universal synthesis method.

Despite additional complications due to high frequencies, numerous techniques for designing microwave filters have been developed.

Microwave filters can be used in combination with other passive elements or devices, as is the case with multiplexers or duplexers, which are frequently employed in telecommunications. Microwave filters are also utilized in active circuits, such as amplifiers, oscillators, etc.

Microwave resonators are used in applications that include filters, oscillators, frequency meters, tuned amplifiers, and microwave sensors. The functioning of microwave resonators is, in many respects, similar to the operation of tuned circuits with localized elements [I.35].

I.5.1. The role of the filter

The role of the filter in systems is fundamental as it involves removing unwanted components from a useful signal, which can be considered as noise. This noise, very important in telecommunications systems, can come from various sources. It can be external, that is, brought by the channel, or internal, brought by the passive and active elements constituting the system itself. The signal-to-noise ratio, which defines the ratio of the useful signal power to that of the noise, is therefore an essential parameter in systems. From another perspective, the emitted and received signals are parasitic to each other, and as a result, a good separation of these signals is necessary. Finally, depending on the architecture chosen for the system, the appearance of spurious frequencies, known as images, is also a problem. In both cases, filtering techniques are used [I.36, I.37].

I.5.2. Filter classification

Filters can be grouped into four main categories based on how they handle the different frequencies of a signal. These major families are low-pass, high-pass, band-pass, and band-stop filters [I.38].

- **Low-pass Filters**: Low-pass filters retain the part of the signal with frequencies lower than a cutoff frequency and eliminate the rest of the spectrum. Figure I.4 represents the gain of a low-pass filter.
- **High-pass Filters**: A high-pass filter allows the passage of frequencies that are above a cutoff frequency and eliminates frequencies below it. It is the opposite of the low-pass filter; these two filters combined create a band-pass filter.
- **Band-pass Filters**: Unlike the first types of filters, the band-pass filter allows the passage of the part of the signal whose frequencies are between a low cutoff frequency and a high cutoff frequency and rejects other frequencies.
- **Band-stop Filters (Notch Filters)**: Band-stop filters, for their part, are the opposite of band-pass filters. They allow all frequencies to pass except those between the low and high cutoff frequencies.

Figure I-14 illustrates ideal filter templates for each type: (a) low-pass, (b) high-pass, (c) band-pass, and (d) band-stop filters.

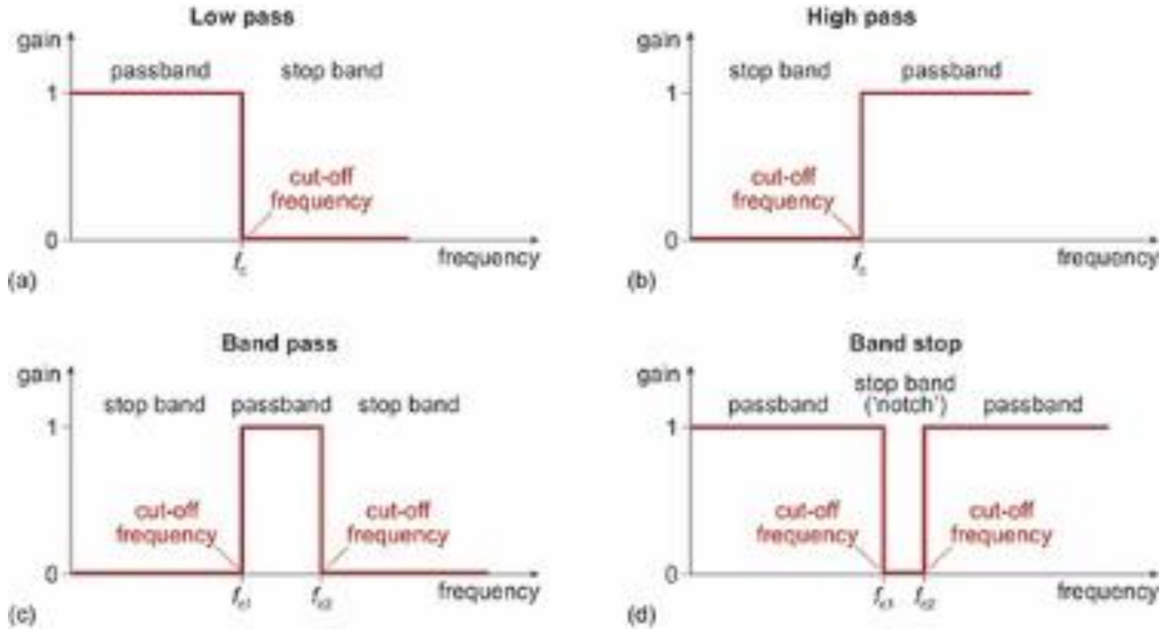

Figure I-14: Ideal filter templates: (a) low pass (b) high pass (c) band pass (d) stop band.

I.5.3. The two families of filters

Filters are generally categorized into two main families:

- **Passive filters**: Passive filters are filtering circuits formed solely by a resistor, an inductor, and a capacitor as the main components. They are currently used for high frequencies. The so-called passive filters, namely RC and RLC filters, are made using components that dissipate or store electrical energy [I.39]. They do not require any external power supply for their operation.
- **Active filters**: Active filters are made up of active components (transistors, operational amplifiers). Unlike passive filters, active filters consume more and require a power source due to the active components (amplifiers and operational transistors).

I.5.3.1. Filter Realization Methods

The method chosen to realize a filter depends on whether amplification is needed and the desired cutoff frequency. Common technologies used to implement filters include:

- **Passive RLC filters**: These filters use combinations of resistors, inductors, and capacitors to achieve the desired filtering characteristics. They are suitable for low-frequency and high-frequency applications depending on the components used [I.40].
- **RC and LC filters**: RC and LC that use configurations resistor-capacitor or inductor-capacitor networks for specific applications depending on the frequency [I.41].

- **Quartz crystal filters**: allows some frequencies to pass through an electrical circuit while attenuating undesired frequencies [I.42].
- **Distributed element filters**: A distributed-element filter is an electronic filter in which the elements of the circuit (capacitance, inductance, and resistance) are not localized in discrete capacitors, inductors, and resistors as they are in conventional filters [I.43].

I.5.3.2. Criteria for selecting filter structures

There are many criteria to choose the best technology and topology to design a filter which are:

- ✓ Electrical criteria: in terms of the cutoff frequency, the bandpass, and rejection bands losses. Along with the in-band ripple, the width of the passband, and the attenuation out of the band.
- ✓ Physical criteria: the size, the weight, and the volume of the device. Additionally, there is mechanical stability, temperature sensitivity, and resistance to power.
- ✓ Economic criteria: it involves the cost from the design to the production to the ongoing adjustment. Along with the filter compatibility with the multiple standers.

I.5.4. Different approximation functions

In the design of filters, various mathematical approximations are utilized to achieve desired frequency responses. The most common approximations are the Butterworth**,** Chebyshev, and Elliptic approximations.

I.5.4.1. Butterworth approximation

The Butterworth approximation is the simplest approximation. This type of filter has no ripple in the passband, but on the other hand, it offers poor out-of-band rejection. The latter can be improved by increasing the number of poles, but it remains, however, inferior to that of other types of filters. It is used in the case of low insertion losses [I.44].

The attenuation function in decibels is defined as:

$$A_{db} = 10\log_{10}\left[1+\left(\frac{\omega}{\omega c}\right)^{2n}\right] \quad (\mathrm{I.}\,18)$$

This corresponds to the amplitude response of the transmission coefficient:

$$|S_{12}\,(j\omega)|^2 = \left[1+\left(\frac{\omega}{\omega_c}\right)^{2n}\right]^{-1} \quad (\mathrm{I.}\,19)$$

Where:

- $\omega_c = 2\pi f_c$ is the cutoff angular frequency

- n is the filter order.

At ω =ωc, the attenuation A is 3 dB, indicating that the output power is half of the input power at the cutoff frequency since $20\log_{10}|S_{12}| = -3dB$.

Figure I-15 illustrates the transmission responses of the Butterworth approximation for different orders *n*. This approximation yields a very flat response in the passband, with increased flatness as the filter order rises.

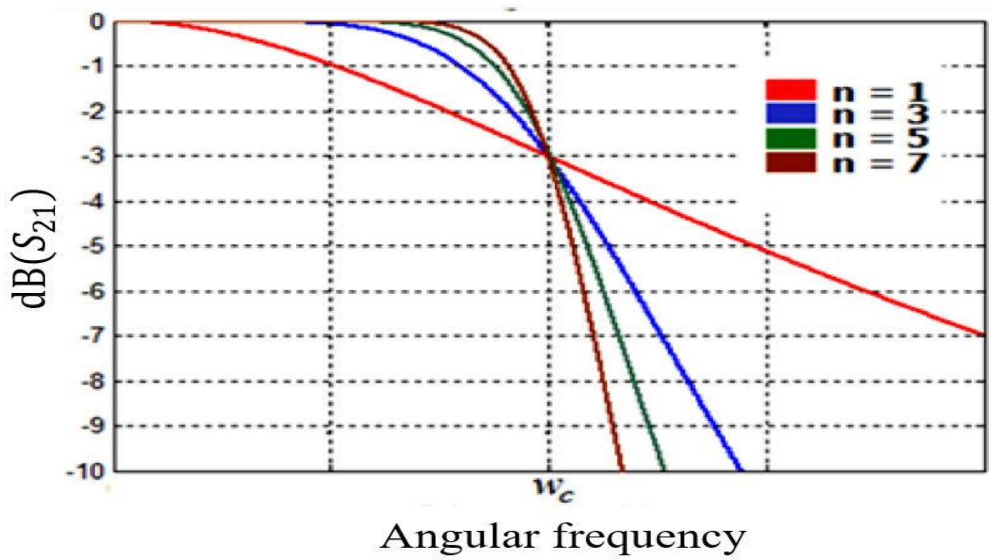

Figure I-15: Transmission responses of the Butterworth approximation for different n orders.

I.5.4.2. Chebyshev approximation

Chebyshev filters tolerate a slight ripple in the passband, but have better rejection than Butterworth filters.

The attenuation function is given by:

$$A_{db} = 10\log_{10}\left[1+\varepsilon^2 {T_n}^2\left(\frac{\omega}{\omega_c}\right)\right] \quad (I.20)$$

Which corresponds to the amplitude response of the transmission coefficient:

$$|S_{12}(j\omega)|^2 = \left[1+\varepsilon^2 {T_n}^2\left(\frac{\omega}{\omega c}\right)\right]^{-1} \quad (I.21)$$

Where:

- T_n is the Chebyshev polynomial of the first kind of order n.
- ε relates to the passband ripple level L_S by :

$$\varepsilon = \sqrt{10^{\frac{L_S}{10}}-1} \quad (I.22)$$

The Chebyshev polynomials are defined as:

$$T_n(x) = \begin{cases} \cos(n\cos^{-1}(x)), & |x| \leq 1 \\ \cosh(n\cosh^{-1}(x)), & |x| \geq 1 \end{cases} \qquad (I.23)$$

Figure I-10 shows the transmission responses of the Chebyshev approximation for different orders *n*. The ripple in the passband and the sharper cutoff compared to the Butterworth filter are evident.

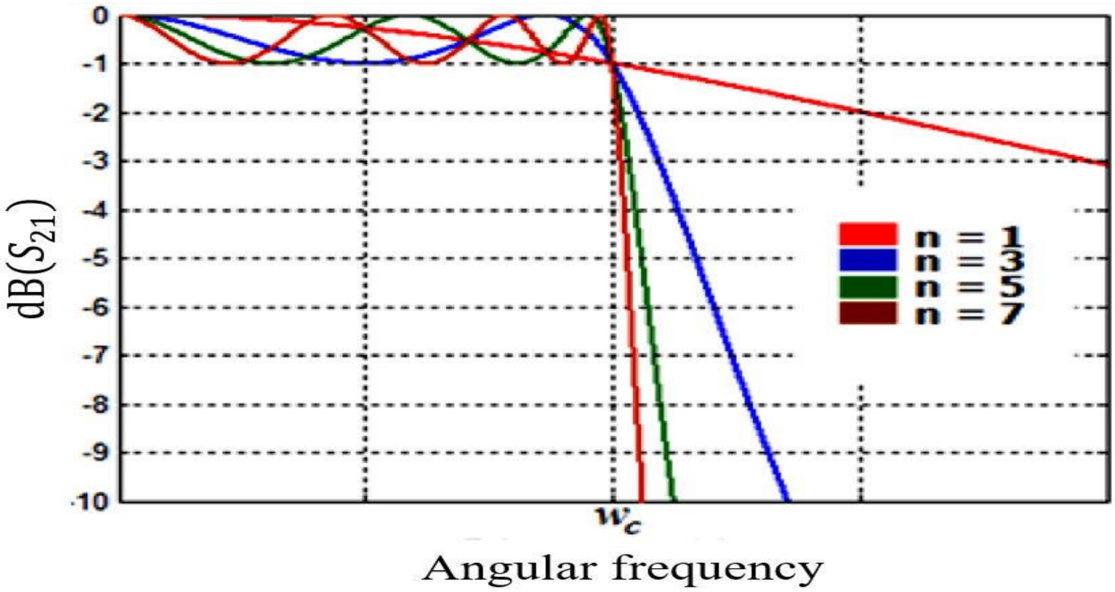

Figure I-16: Transmission responses of the Chebyshev function for different orders n.

I.5.4.3. Elliptic approximation

The Elliptic approximation is characterized by an equiripple in both the passband and the stopband [I.1], [I.45, I.46]. Moreover, it has transmission zeros in its electrical response that allow achieving a good level of selectivity for a limited filter order. Although these filters are efficient, they are more delicate in terms of design and physical implementation [I.44]. A comprehensive presentation on the theory of elliptic functions is provided in reference [I.44], [I.47].

The attenuation function is expressed as:

$$A_{db} = 10\log_{10}\left[1 + \varepsilon^2 \mathrm{R_n}^2(\omega)\right] \qquad (I.24)$$

Where:

- ε is a parameter defining the passband ripple at the cutoff frequency ω_C.
- $\mathrm{R_n}(\omega)$ is the Elliptic rational function of order n.

Figure I-17 presents the Magnitude response showing parameters used to specify an elliptical filter.

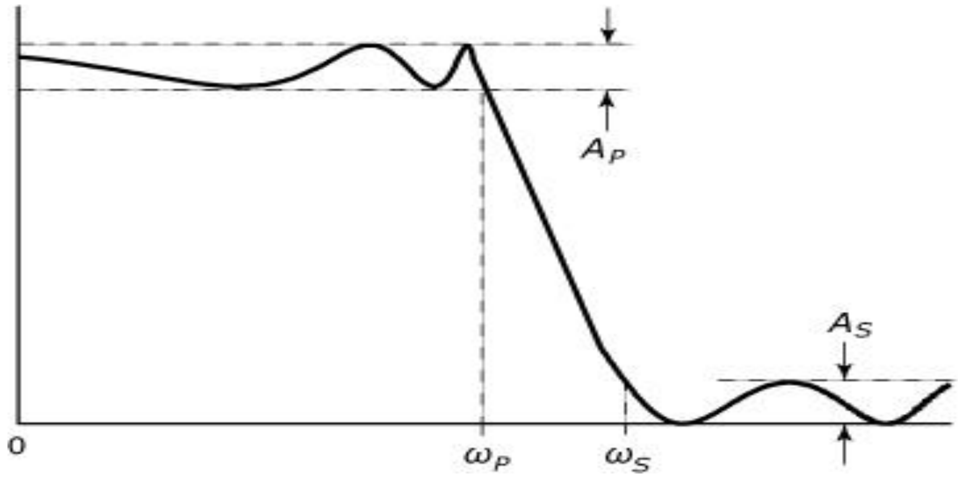

Figure I-17: The Magnitude response showing parameters used to specify an elliptical filter.

I.5.5. Template of a band pass filter

The bandwidth limits are generally the frequencies where the gain decreases by 3 dB (to $1/\sqrt{2}$ of its maximum voltage gain). These frequencies are called the 3 dB frequencies or cutoff frequencies. The bandwidth of a band-pass filter is the interval between the low cutoff frequency (FL) and the high cutoff frequency (FH).

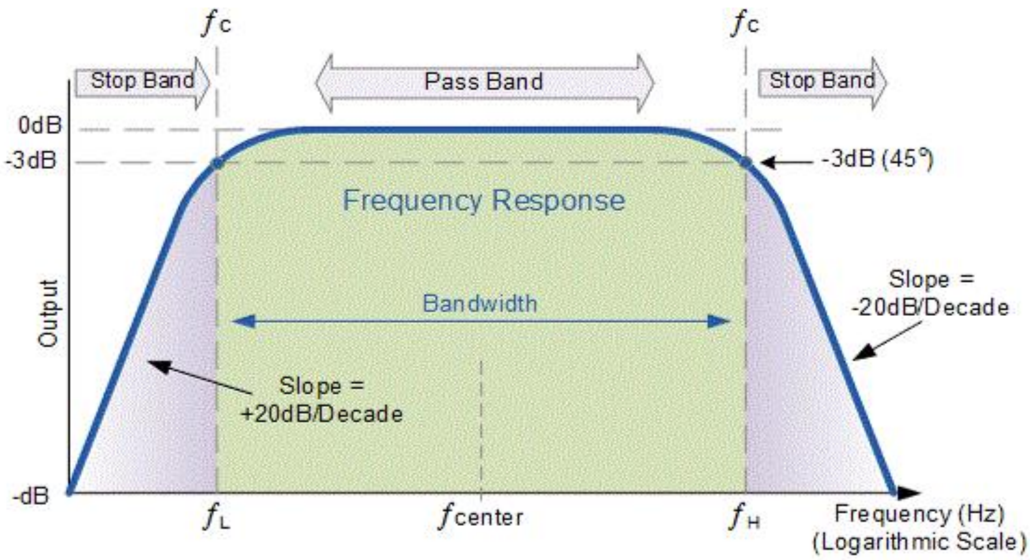

Figure I-18: The frequencies and the bandwidth of a band-pass filter.

- **Center frequency (f_c)**: The midpoint frequency of the passband.
- **Bandwidth (Δf)**: The width of the passband where the filter allows signals to pass with minimal attenuation.

- **Insertion loss**: The loss of signal power resulting from the insertion of the filter in the signal path, ideally minimized within the passband.

These electromagnetic parameters can be calculated by transforming a low-pass filter prototype into a bandpass filter through frequency mapping techniques, which will be discussed in the following sections [I.1].

I.5.6.Bandpass filter synthesis

Bandpass filter synthesis involves several critical steps. It begins with determining the equivalent low-pass prototype of the desired filter, followed by the selection of the appropriate filter topology based on electrical specifications such as center frequency, bandwidth, and insertion loss. The filter response type-whether Chebyshev, Butterworth, elliptical, or pseudo-elliptical-must also be chosen [I.48].

Figure I-19 shows the equivalent diagram of a low-pass prototype with localized elements.

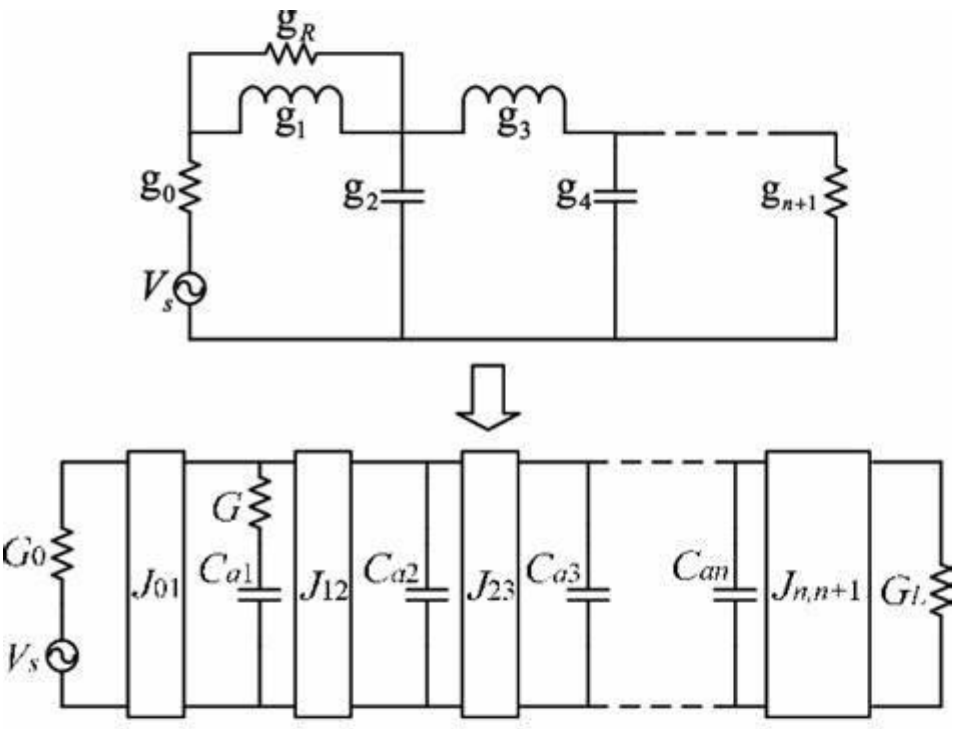

Figure I-19: Equivalent diagram of a low-pass prototype with localized elements.

I.5.6.1. Low-pass prototype elements

The elements of a normalized low-pass filter are calculated using classical recurrence formulas:

$$g_0 = 1 \tag{I.25}$$

$$g_k = \frac{2a_k}{\gamma} \ Pour \ K = 1 \tag{I.26}$$

$$g_k = \frac{4a_{k-1} . a_k}{b_{k-1} . g_{k-1}} \quad for\ K = 2, 3 \dots . n \tag{I.27}$$

$$a_k = \sin\left|\frac{(2K-1)\pi}{2n}\right| for\ K = 1, 2 \dots , n \tag{I.28}$$

$$b_k = \gamma^2 + sin^2\left(\frac{K\pi}{n}\right) \tag{I.29}$$

$$\gamma = sh\left(\frac{\beta}{2n}\right) for\ K = 1, 2 \dots . n \tag{I.30}$$

$$\beta = Ln\left(coth\frac{A_m}{17.37}\right) \tag{I.31}$$

A_m is the amplitude of the ripple.

I.5.6.2. Converting to band pass filter

The process of creating filters that attenuate frequencies outside of a given range while permitting signals within that range to pass is known as bandpass filter synthesis. Bandpass filters can be synthesized using a variety of approaches, such as prototype-based designs, coupling matrix rotation, and frequency transformation algorithms [I.49].

$$\Delta = \frac{\omega_H - \omega_L}{\omega_0} \tag{I.32}$$

$$\omega_0 = \sqrt{\omega_L \omega_H} \tag{I.33}$$

Series elements become series resonant circuits:

$$C'_{bp} = \frac{C}{\omega_0 \Delta} = \frac{g_k}{\omega_0 \Delta} \tag{I.34}$$

$$L'_{bp} = \frac{\Delta}{C\omega_0} = \frac{\Delta}{g_k \omega_0} \tag{I.35}$$

$$\omega \rightarrow \frac{1}{\Delta}\left(\frac{\omega_0}{\omega_{bp}} - \frac{\omega_{bp}}{\omega_0}\right) \tag{I.36}$$

Figure I-20 illustrates the equivalent bandpass diagram using localized elements.

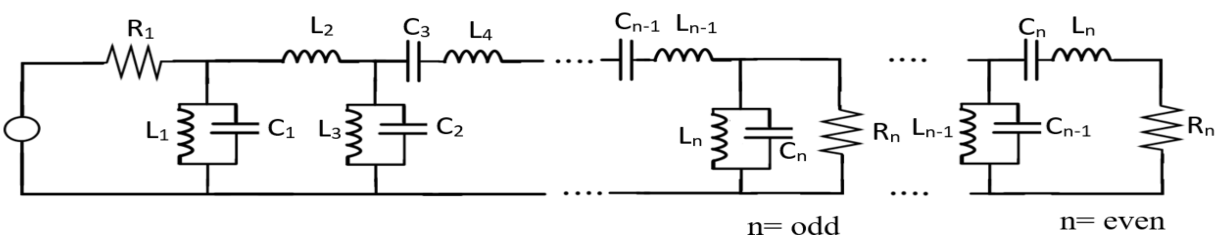

Figure I-20: A localized element bandpass prototype's equivalent diagram.

I.5.7. Distributed element filters

Filters using localized elements cannot be directly implemented in the microwave band due to the low values of components. Therefore, it is necessary to transform these elements into their equivalents in transmission lines. Microwave filters often employ dynamic reactive parameters and impedance (or admittance) inversion parameters to define the resonators and connections between them, respectively.

Knowing the values of the elements $g_k$of the standardized low-pass prototype, the synthesis process involves determining the coupling parameters $K_{i,i+1}$ and the lengths of the resonators. These resonators are typically half-wave or quarter-wave lines. When designing filters with series resonators connected by impedance inverters, the following equations are used:

$$K_{01} = \sqrt{\frac{\pi\omega_\lambda}{2*\Omega_c* g_0 g_1}} \tag{I.37}$$

$$K_{i,i+1\left\{\begin{smallmatrix} i=1 \\ i=n+1 \end{smallmatrix}\right.} = \frac{\pi\omega_\lambda}{2*\Omega_c}\sqrt{\frac{1}{g_i g_{i+1}}} \tag{I.38}$$

$$K_{n,n+1} = \sqrt{\frac{\pi\omega_\lambda}{2*\Omega_c* g_n g_{n+1}}} \tag{I.39}$$

Where:

- λ=$\frac{c}{\sqrt{\varepsilon f}}$ is the wavelength in the medium.
- θ Represents the electrical length of the resonators.

The dynamic reactance of a series resonator at the central frequency $x_i(\omega_0)$ is given by [I.3]:

$$x_i = \omega_0 L_i = \frac{\omega_0}{2}\frac{dX_{i(\omega)}}{d\omega}|\omega = \omega_0 \tag{I.40}$$

I.5.7.1.Practical implementation

To achieve acceptable results, half-wave and quarter-wave resonators are typically used for relative bandwidths up to 20% and 40%, respectively. The electrical length of resonators is calculated using:

$$\theta_i = \pi - \frac{1}{2}\left(\tan^{-1}\left(\frac{2X_{i-1,i}}{Z_0}\right) + \tan^{-1}\left(\frac{2X_{i,i+1}}{Z_0}\right)\right) \tag{I.41}$$

Where Z_0 = 50 Ω is the characteristic impedance.

Figure I-21 illustrates an impedance inverter-based bandpass filter circuit.

The length of a waveguide cavity is given by:

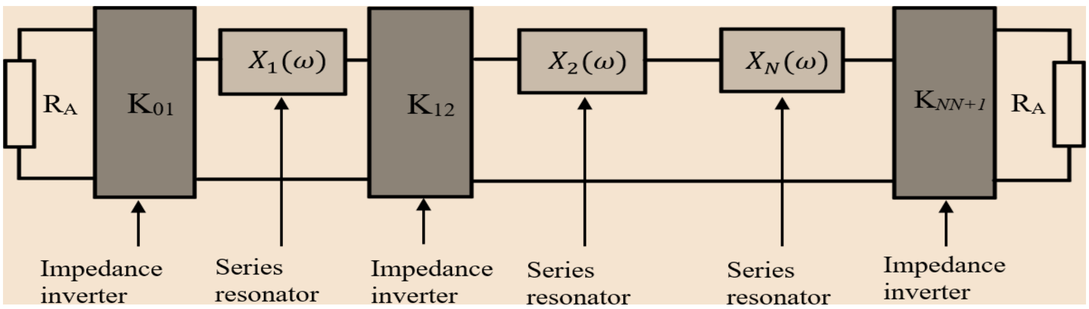

Figure I -21: An impedance inverter-based band pass filter circuit.

The length of a waveguide cavity is given by:

$$L = \frac{\lambda\theta}{2\pi} \tag{I.42}$$

Where:

$$\lambda = \frac{c}{\sqrt{\varepsilon} f} \tag{I.43}$$

I.5.8. Filter characterization

The performance of a filter is primarily determined by the performance of its resonators. This section explores the properties that can be used to evaluate a resonator's performance based on its electrical response.

I.5.8.1. Cutoff frequency and center frequency

A filter's cutoff frequency is the frequency at which it begins to attenuate the signal significantly. Specifically, it is the frequency at which the signal's amplitude decreases by 3 dB. Depending on the type of filter, the frequencies that are affected by the filter lie either before or after the cutoff frequency. The center frequency, on the other hand, is defined as the midpoint frequency where the filter operates symmetrically within the frequency spectrum [I.1] [I.3].

I.5.8.2. Insertion losses

Insertion loss refers to the attenuation of the signal resulting from the insertion of a filter into a signal path. It is defined as the difference in power before and after the filter insertion. Insertion losses are crucial in analyzing the performance of a resonator and understanding losses due to radiation, ohmic effects, and dielectric materials [I.50].

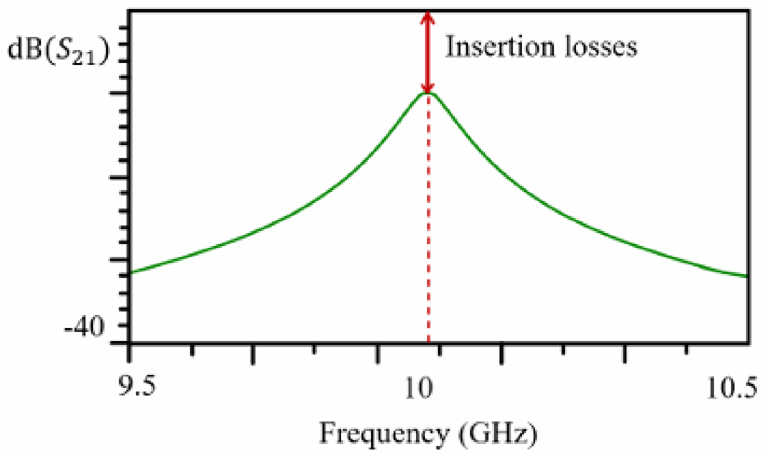

Figure I-22: An illustration of a resonator's insertion losses.

I.5.8.3. Loaded quality factors

The loaded quality factor (Q_L) is a dimensionless metric that quantifies a resonator's selectivity. It is determined by the resonant frequency (f_r) and the -3 dB bandwidth frequencies ($f_0 and f_1$) [I.51]:

$$Q_L = \frac{f_r}{f_2 - f_1} \tag{I.44}$$

Figure I-23 demonstrates how to extract the parameters f_c,f_0 and f_1 from the transmission S_{21} response. A higher Q_L indicates better selectivity. However, Q_L does not account for the resonator's intrinsic performance, as it is dependent on frequency and does not consider insertion losses.

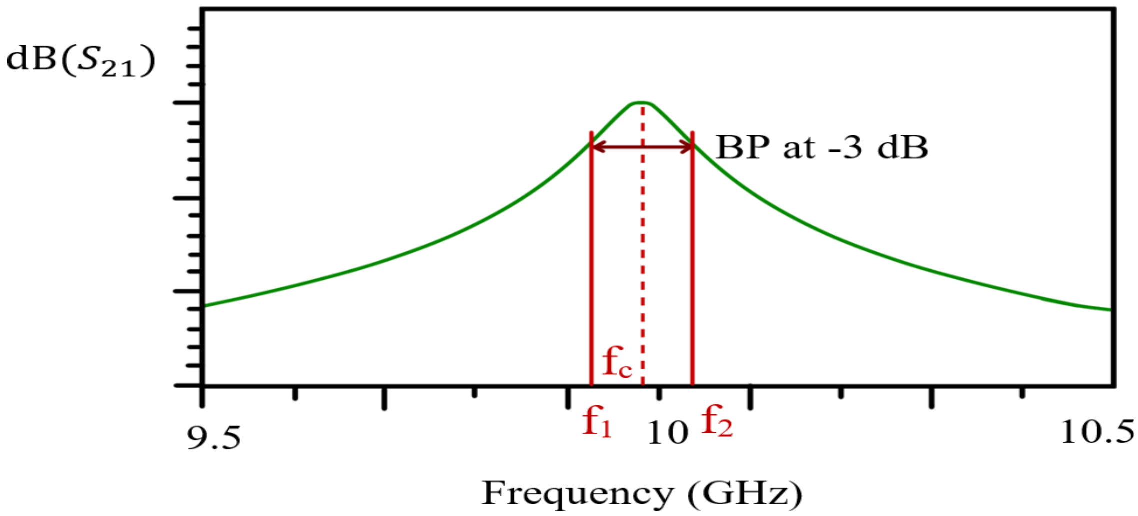

Figure I-23: Extracting the parameters to calculate the loaded quality factor from the electrical response in the transmission of a resonator.

I.5.8.4. Unloaded quality factors

The unloaded quality factor (Q_0) is controlled by three loss mechanisms and defined.

$$\frac{1}{Q_L} = \frac{1}{Q_{est}} + \frac{1}{Q_0} \tag{I.45}$$

The losses associated with the resonator's excitation mechanism are represented by the external quality factor Q_{est} , which can be computed as follows:

$$Q_{est} = \frac{Q_L}{|S_{21(f_r)}|} \tag{I.46}$$

The natural value insertion loss is denoted by S_{21}. The performance of the resonator is well-represented by the unloaded quality factor (Q_0), which is larger when the insertion loss is lower and the rejection level is higher. Equations $(\mathrm{I}.45)$ and $(\mathrm{I}.46)$ allow us to infer [I.51]:

$$Q_0 = \frac{Q_L}{1-|S_{21(f_r)}|} \quad (\mathrm{I}.47)$$

I.6. Reconfigurable microstrip filters

In recent years, several reconfigurable BPFs have been introduced [I.52, I.61]. A reconfigurable microstrip BPF using a varactor diode was designed and analyzed to achieve a constant impedance bandwidth in [I.53]. Reconfigurability is obtained by tuning the resonance frequencies for both the odd and even modes, where there is no mutual coupling between these two modes. Figure I-24 shows the proposed tunable BPF with the obtained performance.

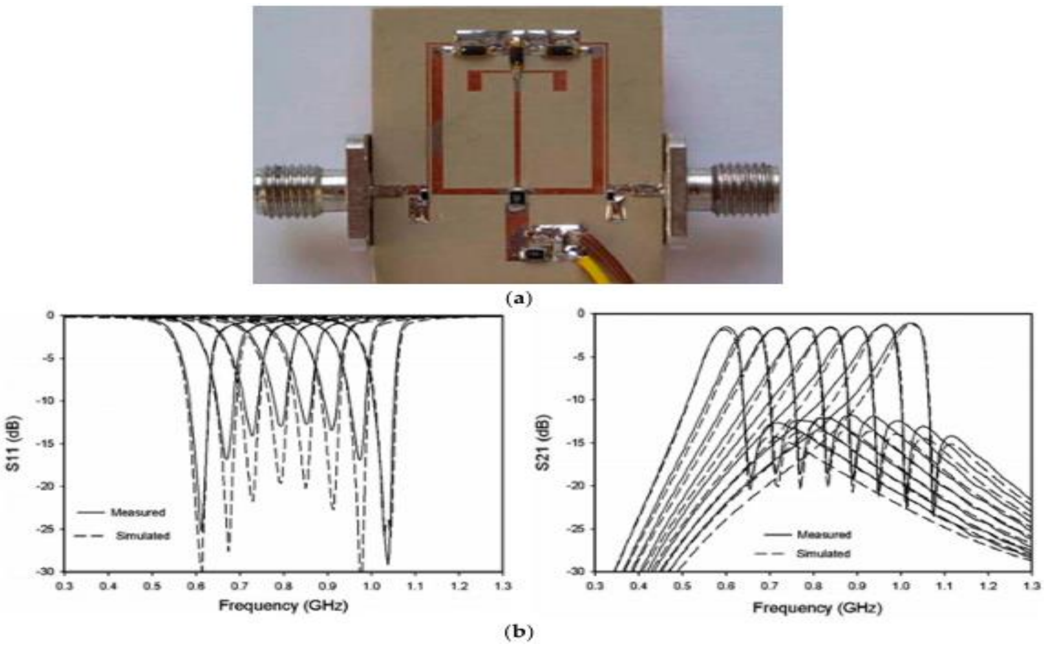

Figure I-24: The reconfigurable filter reproduced from [I.29]. 2020, IEEE: (a) prototype structure; (b) S-parameter performance.

I.6.1. Concepts of reconfigurable microstrip filters using diodes

Several reconfigurable microstrip filter designs have been proposed over the years. Here are a few noteworthy examples:

I.6.1.1. Reconfigurable BPF using one varactor diode

The practical BPF performance depicts a good roll-off skirt on the low edge of the transmission band, with an insertion loss of less than 2.2 dB and a return loss of more than 10 dB. A 2.2–22.0 V reverse bias voltage is applied across the varactor diode to achieve a tuning rate of 40% for the 0.60–1.0 GHz range, with 91 MHz impedance bandwidth for all configurations.

Figure I-24 (a) shows the design of (a) the simulated and measured S-parameters, a and (b) photograph of NWB BPF with controllable notch bandwidth.

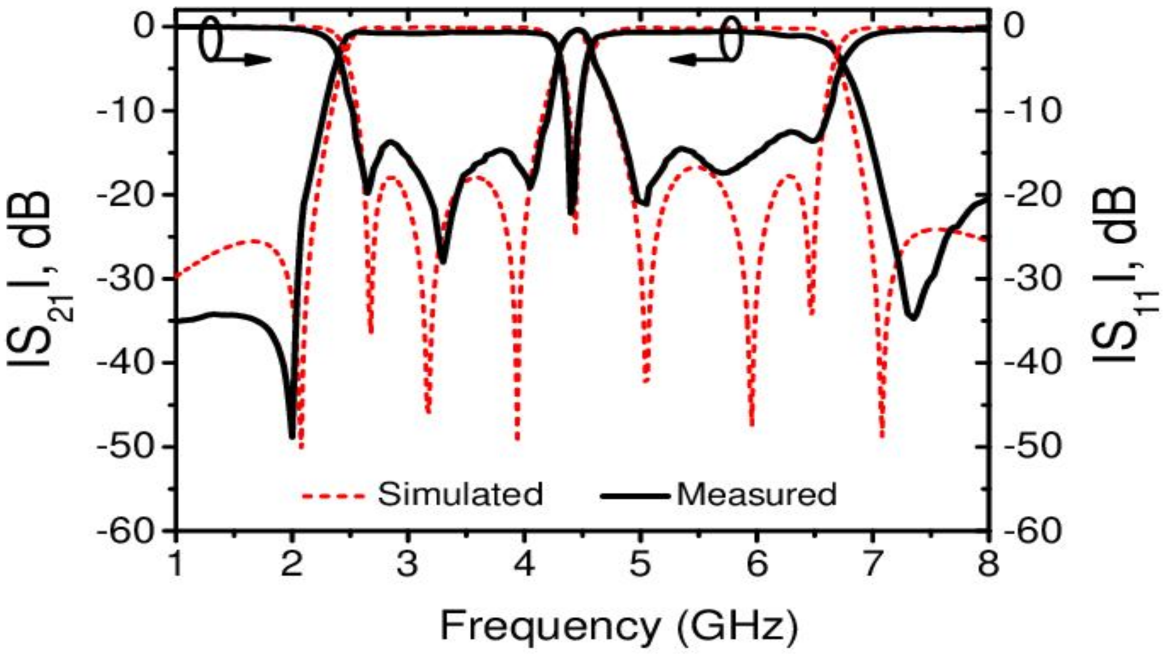

(a)

(b)

Figure I-25: (a) The simulated and measured S-parameters, a and (b) photograph of NWB BPF with controllable notch bandwidth

I.6.1.2. Reconfigurable BPF using two varactor diodes

In [I.54], a reconfigurable microstrip BPF utilizes two varactors to tune two finite transmission zeros (TZs). The center frequency and the bandwidth are controlled to cover a wide range of about 600 MHz (1.4 GHz to 2.0 GHz) by altering the reverse bias voltage across the varactors (as seen in Figure I-26). The measurement results show that the filter has an insertion loss of less than 4 dB, a return loss of more than 18 dB, and a fractional bandwidth of about 10%. A stopband rejection level of more than 25 dB is obtained by using the two transmission zeros. A 0.21–30.02 V bias voltage is applied across the diodes to tune the resonance frequency. In [I.55], a compact tunable planar BPF with a constant fractional bandwidth is introduced. By increasing the reverse bias voltage across the switches, the center frequency of the filter is tuned from 3.4 GHz to 3.8 GHz, with a fractional, with a fractional bandwidth of about 11%. The presented tunable filter has the advantages of having a compact size and simple structure, using only one varactor diode switch

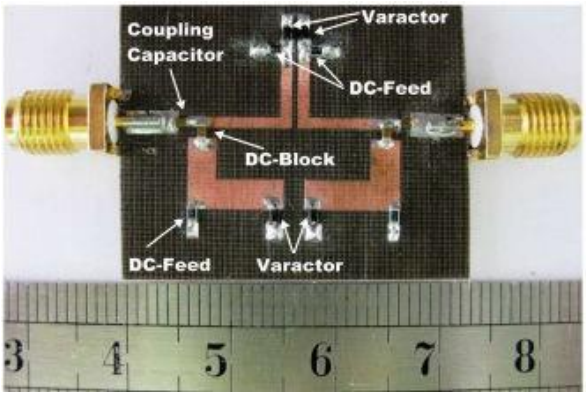

(a)

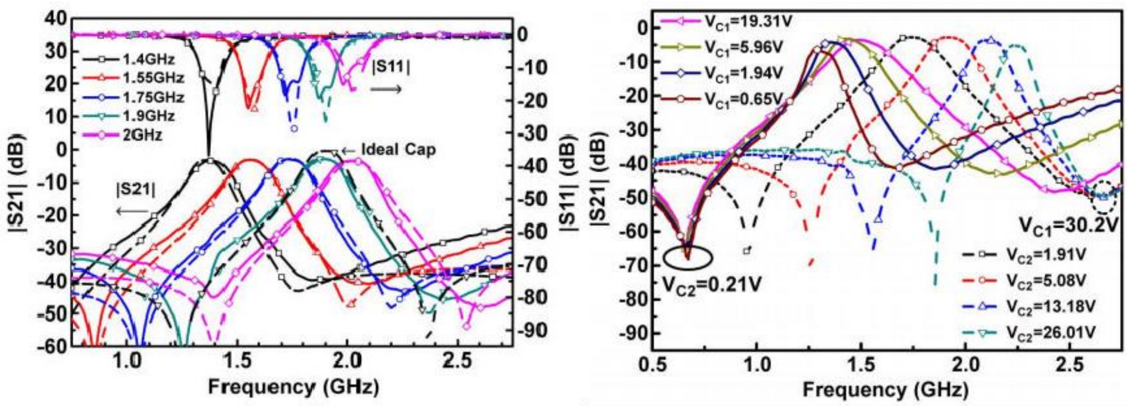

(b)

Figure I-26: (a) the filter's design. (b) the [S11] and [S21] of the different cases obtained.

I.6.1.3. Reconfigurable Band stop filters

Ebrahimi et al. [I.56] proposed a notch dual-mode tunable band stop planar filter using two varactor diodes. The proposed filter is implemented by loading inductive and capacitive coupling into the input and output transmission lines of the microstrip filter. The inductors were designed by using thin inductive strips. As illustrated in Figure 4, the second-order filter has a compact size of 0.13 λg × 0.17 λg and offers a continuous tuning range for the resonance frequency that ranges from 0.8 GHz to 1.1 GHz, with a stopband fractional bandwidth of about 17%. The measurement results show that the filter has a 0.9 dB stopband return loss and 0.6 dB passband insertion loss over the entire tuning range. Apart from the other designs, the inductive coupling is achieved using an inductor in the bottom layer of the patch filter. This configuration avoids the need for a more complicated three-layered structure, provides more degrees of freedom in controlling the coupling coefficient factors, and maintains the top layer configuration, resulting in a more compact design.

(a)

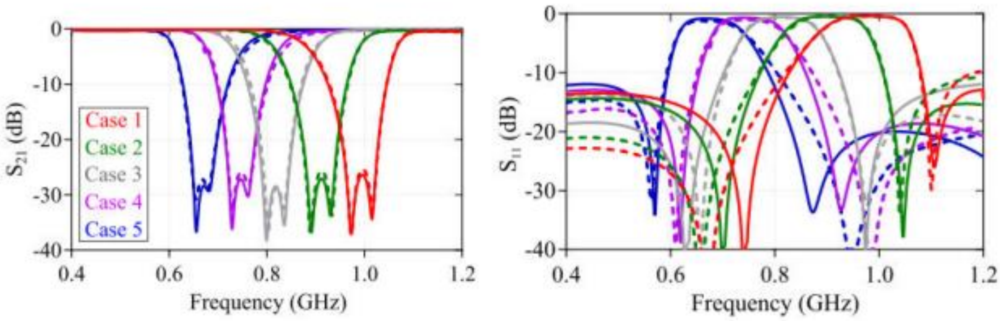

(b)

Figure I-27: (a) The proposed tunable filter upper and bottom layers. (b) the S21 and S11 coefficients of this filter along the tuning range.

I.6.1.4. Compact 2-pole BPF

Moreover, Chen et al. [I.57] introduced a 2-pole fully tunable planar filter with a small structure, continuous frequency tuning range, and constant impedance bandwidth. Two varactors are utilized to tune the resonance frequency between the high and low resonating modes. The tunable filter has a simple configuration that consists of a pair of reversed biased varactor diodes. Each resonator contains two transmission lines, which are connected together via a varactor diode. A 0.4–18 V bias voltage is applied to provide 0.3–2.4 pF capacitance. The tuning range for the resonance frequency was from 1.2 GHz to 1.9 GHz, with an operational impedance bandwidth of about 39 MHz. The proposed filter offers a compact size of 0.06 λg × 0.27 λg, continuous tunability, simple structure, and a wide-tuned spectrum, which make the designed BPF suitable for recent and future wireless communications. The proposed tunable filter with the achieved insertion and return losses is shown in Figure I-28

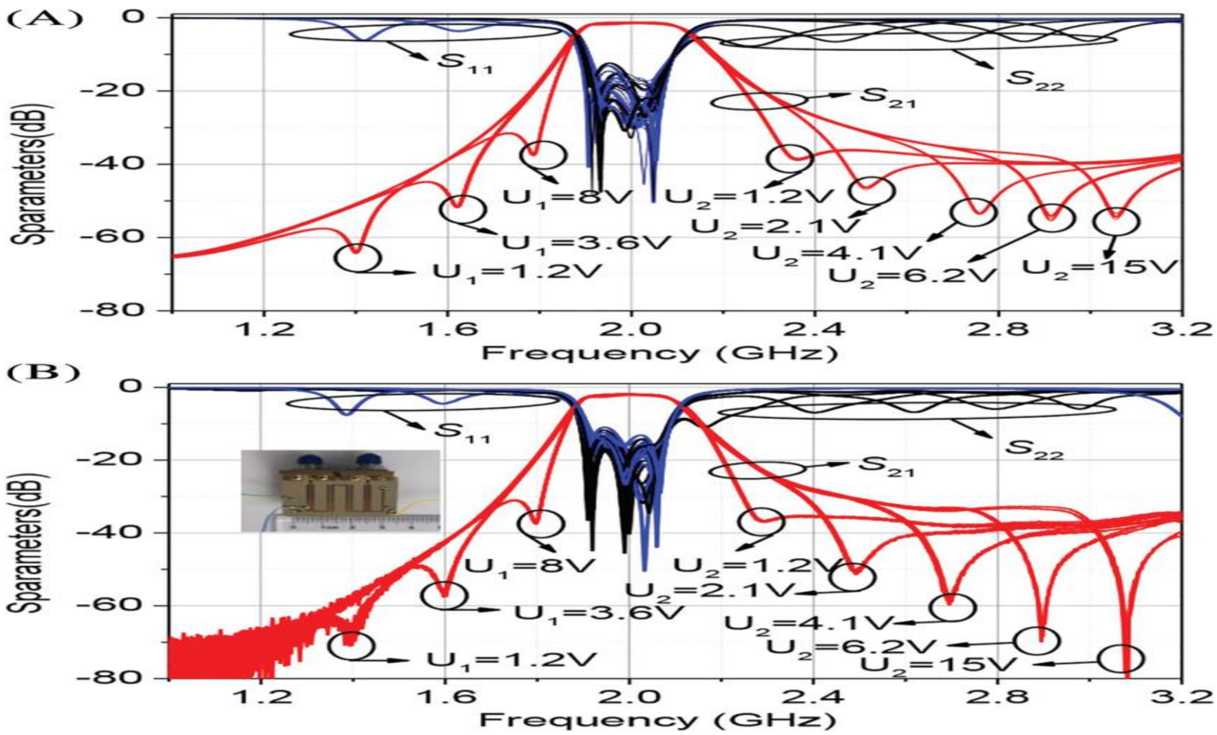

Figure I-28: The S11 and S21 coefficients of the reconfigurable filter proposed, along with a picture of the fabricated model.

I.6.1.5. Tunable microstrip filter for 4G and 5G applications

In [I.60], a very compact microstrip reconfigurable filter for fourth-generation (4G) and sub-6 GHz fifth-generation (5G) systems using a new hybrid co-simulation method is presented. The basic microstrip design uses three coupled line resonators with λ/4 open-circuit stubs. The coupling coefficients between the adjacent and non-adjacent resonators are used to tune the filter at the required center frequency to cover the frequency range of 2.5 GHz to 3.8 GHz. Figure I-29 shows the simulated insertion and return losses of the proposed reconfigurable filter.

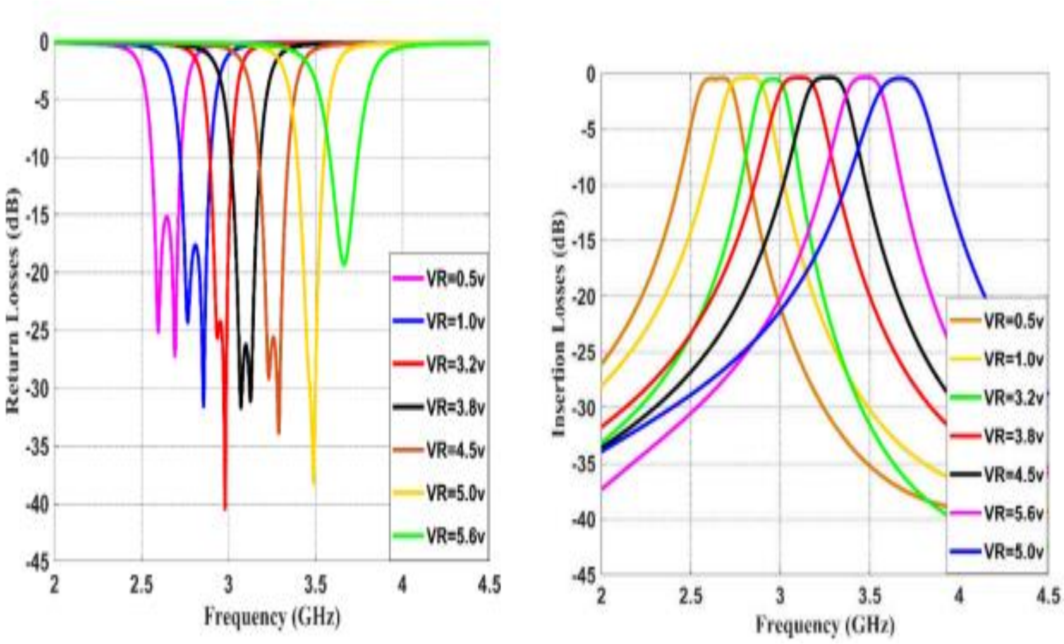

Figure I-29: The obtained simulation results of the proposed filter, featuring the S parameters.

However, with the rapid development of current 4G and 5G applications, compact and reconfigurable planar filters with a wide tuning range are needed. To this end, several tunable filters have offered some attractive features that are essential for current and future wireless communications. Table I-1 shows the comparative performance of the reviewed reconfigurable microstrip BPFs. It is clear that the proposed filter in [I.60] has a wider tuning range, wider impedance bandwidth, smaller insertion losses, and smaller size compared to the designs presented in [I.53, I.54, I.56, I.60]. The tunable filters presented in [I.53, I.57] have an impedance bandwidth of only 40 MHz. additionally, the tunable filter proposed in [I.59, I.60] only use two varactor diode switches and a simple biasing circuit to achieve the tunable frequency and efficient characteristics. As a result, the filter presented in [I.60] has very good performance in terms of the S-parameter group delay and the phase of S21, along with other attractive features, such as its compact size, relatively few tuning diodes, and simple structure; thus, it is a good option for many 5G systems.

Table I-1 Comparison among the tunable microstrip filters.

Ref.	Year	Topology	Tuning Rang (GHz)	BW(MHz)	N^{br}. of Switches	Insertion loss	Filter size (mm3)	Challenges-Limitations
[53]	2010	Dual-Mode	0.6-1.0	85-95	3	2.2	30× 23 × 1.27	Low tuning rang
[54]	2011	Coupled lines	1.5-2.0	110	4	4	36× 30 × 0.80	High loss
[56]	2018	Dual-Mode	0.66-0.99	108	4	0.75	72× 70 × 1.6	Low tuning rang
[57]	2018	Ring-resonator	1.1-2.1	40	7	6	52× 12 × 1.6	Number of switches
[58]	2018	Dual-Mode	1.7-2.9	40	7	4	36× 35 × 0.8	Number of switches
[59]	2018	Multimode	0.76-2	75-150	2	1.2	100× 8 × 0.50	Size
[60]	2019	Coupled lines	2.5-3.8	95-115	2	0.8	13 × 8 × 0.80	Constant bandwith

I.7. Conclusion

An overview of transmission line theory and the electromagnetic spectrum, including an introduction to coplanar and microstrip technologies, kicked off the chapter. An extensive overview of filter theory was given in the second portion, emphasizing the function of filters in diverse systems. Filters were divided into two families and four primary types. Furthermore, the features and design implications of three distinct approximation techniques—Butterworth, Chebyshev, and Elliptic—were examined. The chapter concluded by reviewing the most recent developments in reconfigurable microstrip-based filters, with an emphasis on systems that use diodes to achieve tunability. These reconfigurable filters' performance was contrasted with that of their non-reconfigurable counterparts, highlighting the benefits and drawbacks of each design.

References

[I.1] **Pozar, D. M.** (2012). Microwave engineering

[I.2] **Collin, R. E.** (2001). Foundations for microwave engineering

[I.3] **Matthaei, G. L., Young, L., & Jones, E. M. T.** (1980). Microwave filters, impedance-matching networks, and coupling structures

[I.4] **Jarry, P., & Beneat, J.** (2009). Advanced design techniques and realizations of microwave and RF filters

[I.5] **The Editors of Encyclopedia Britannica.** (2013, September 6). Faraday's law of induction | physics. Encyclopedia Britannica. Retrieved from https://www.britannica.com/science/Faradays-law-of-induction

[I.6] **Lv, H., Yang, Z., Liu, B., & al.** (2021). A flexible electromagnetic wave-electricity *harvester.* Nature Communications, 12(1), 834.

[I.7] **Ball, D. W. (2015).** Faraday and the Electromagnetic Theory of Light

[I.8] **Wu, Z., Cheng, H. W., Jin, C., & al.** (2022). Dimensional design and core–shell engineering of nanomaterials for electromagnetic wave absorption. Advanced Materials, 34

[I.9] **Zhao, Y., Hao, L., Zhang, X., & al.** (2022). A novel strategy in electromagnetic wave absorbing and shielding materials design: Multi-responsive field effect. Small Science, 2(2), 2100077.

[I.10] **Peng, M., & Qin, F.** (2021). Clarification of basic concepts for electromagnetic interference shielding effectiveness. Journal of Applied Physics, 130(22).

[I.11] **Luo, X., Pu, M., Guo, Y., & al.** (2020). Catenary functions meet electromagnetic waves: Opportunities and promises. Advanced Optical Materials, 8.

[I.12] **Wang, T., Chen, G., Zhu, J., & al.** (2021). Deep understanding of impedance matching and quarter wavelength theory in electromagnetic wave absorption. Journal of Colloid and Interface Science, 595, 1-5

[I.13] **Jackson, J. D.** (1999). Classical electrodynamics (3rd ed.). Wiley.

[I.14] **Bertolotti, M., Sibilia, C., & Guzman, A. M.** (2017). *Evanescent waves in optics:* An introduction to plasmonics. Springer International Publishing AG.

[I.15] **Maxwell, J. C.** (1865). VIII. A dynamical theory of the electromagnetic field. Philosophical Transactions of the Royal Society of London, *155*, 459–512. https://doi.org/10.1098/RSTL.1865.0008

[I.16] **Schelkunoff, S. A.** (1955). Conversion of Maxwell's equations into generalized Telegraphist's equations. Bell System Technical Journal, 34(5), 995–1043. https://doi.org/10.1002/j.1538-7305.1955.tb03787.x

[I.17] **Smith, P. H.** (1939). Transmission line calculator. Electronics, 12(1), 29–31.

[I.18] **Smith, P. H.** (1944). An improved transmission line calculator. *Electronics, 17*(1), 130.

[I.19] **Steer, M.** (2021). *Fundamentals of Microwave and RF Design*. LibreTexts Engineering.

[I.20] **Maxwell, J. C.** (1873). A treatise on electricity and magnetism (Vol. 2). Cambridge University Press.

[I.21] **Sengupta, D. L., & Sarkar, T. K.** (2003). Maxwell, Hertz, the Maxwellians, and the early history of electromagnetic waves. IEEE Antennas and Propagation Magazine, 45(2), 13–19.

[I.22] **Kazemipour, A.** (2002). Contribution to the study of coupling between antennas, application to electromagnetic compatibility and the design of antennas and antenna arrays (Doctoral dissertation). École nationale supérieure des télécommunications, Speciality: Communications and Electronics.

[I.23] **Lee, Y.-M., Wang, S. T., Teng, H.-C., & Cherng, S.** (2013). A functional microstrip circuit module for annular slot antenna. Progress in Electromagnetics Research, 136, 255–267.

[I.24] **Wang, D., Song, L., Zhou, H., & Zhang, Z.** (2012). A compact annular ring microstrip antenna for WSN applications. Sensors, 12

[I.25] **Vaudon, P.** (2004). Printed antennas. Master's Research in Telecommunications, High Frequencies, and Optics, IRCOM - University of Limoges.

[I.26] **Simons, R.** (2001). Coplanar waveguide circuits, components, and systems. Wiley.

[I.27] **Heinrich, W.** (1993). Quasi-TEM description of MMIC coplanar lines including conductor loss effect. IEEE Transactions on Microwave Theory and Techniques, 41(1).

[I.28] **Ndiaye, O., Charles, M., Allal, D., & Bocquet, B.** (2013). Caractérisation électromagnétique des matériaux pour des applications industrielles jusqu'à 110 GHz. 16th International Congress of Metrology, 11004. https://doi.org/10.1051/metrology/201311004

[I.29] **Suh, Y.-H., & Chang, K.** (2002). Coplanar stripline resonators modeling and applications to filters. IEEE Transactions on Microwave Theory and Techniques, 50(5), 1289-1295. https://doi.org/10.1109/TMTT.2002.800420

[I.30] **Zermane, A., Sauviac, B., Bayard, B., & Benghalia**, A. (2009). Comparative study of a coplanar line using three methods. SETIT 2009.

[I.31] **Testbook.** (2024, September 23). Transmission line model: Know types of circuit model & uses. Testbook.

[I.32] **Orloff, N. D., Popovic, N., Drisko, J. A., Stelson, A., Little, C. A. E., Booth, J. C., Mateu, J., & Long, C. J.** (2017). How to extract distributed circuit parameters from the scattering parameters of a transmission line. National Institute of Standards and Technology.

[I.33] **Wheeler, H. A.** (1984). Reflection charts relating to impedance matching. IEEE Transactions on Microwave Theory and Techniques, 32(9), 1008–1021.

[I.34] **Smith, P. H.** (1969). Electronic applications of the Smith Chart in waveguide, circuit, and component analysis. McGraw-Hill.

[I.35] **Combes, P. F.** (1997). Microwaves, 2: Passive circuits, propagation, antennas. Dunod.

[I.36] **Vuong, T.** (1999). Contribution to the study of discontinuities in hollow metallic waveguides: Application to antennas and filters (Doctoral dissertation). National Polytechnic Institute of Toulouse.

[I.37] **Nasser, A.** (2008). Contribution to the development of synthesis methods for the design of multi-bandwidth microwave filters (Doctoral dissertation). University of Limoges, High Frequency Electronics and Optoelectronics.

[I.38] **Rhodes, D.** (1976). Theory of electrical filters. John Wiley & Sons.

[I.39] **Boite, R., Hasler, M., & Dedieu, H.** (1997). Nonlinear effects in digital filters. PPUR Polytechnic Presses.

[I.40] **Tran, M. T., Kuwana, A., & Kobayashi, H.** (2020). Design of active inductor and stability test for passive RLC low-pass filter. CS & IT - CSCP, 10, 203–224. https://doi.org/10.5121/csit.2020.101016

[I.41] **Joshi, M.** (2017, March 13). RC and LC filters - Circuit diagram, waveforms, and working principle. MyClassBook.

[I.42] **Hardcastle, J. A., & Steder, H.** (2009). Crystal ladder filters for all. QEX, Nov/Dec., 15–18.

[I.43] **Wanhammar, L.** (2009). Analog filters using MATLAB. Springer.

[I.44] **Nouri, K.** (2008). Design, implementation, and characterization of filters and duplexers in waveguide and SIW technologies: Application to communication systems (Doctoral dissertation). University of Tlemcen, Telecommunications.

[I.45] **Saal, R., & Ulbrich, E.** (1958). On the design of filters by synthesis. IRE Transactions on Circuit Theory, *5*, 284–327.

[I.46] **Vu, T. M.** (2010). Contribution to the implementation of tunable RF MEMS functions in the millimeter wave band on silicon (Doctoral dissertation). University of Toulouse, Microwave Electromagnetism and Optoelectronics.

[I.47] **Chawbet, M.** (1987). Microwave filters with dielectric resonators (Doctoral dissertation). University of Limoges.

[I.48] **Wu, Y., Fourn, E., Besnier, P., & Quendo, C.** (2021). Direct synthesis of multiband bandpass filters with generalized frequency transformation methods. IEEE Transactions on Microwave Theory and Techniques, 69(8), 3820–3831.

[I.49] **Sheta, A.-F. A., & Elshafiey, I.** (2024). A new compact wideband filter based on a coupled stepped impedance resonator. Micromachines, 15(2), Article 259. https://doi.org/10.3390/mi15020259

[I.50] **Bhattacharya, A.** (n.d.). Introduction to insertion loss-based microwave filter design (Lecture No. 6). NPTEL.

[I.51] **Doe, J.** (2025). Measuring the unloaded, loaded, and external factors (Technical report).

[I.52] **Al-Yasir, Y. I. A., Parchin, N. O., Abdulkhaleq, A., Abd-Alhameed, R., & Noras, J.** (2019). Recent progress in the design of 4G/5G reconfigurable filters. Electronics, 8(1), 1–17. https://doi.org/10.3390/electronics8010017

[I.53] **Tang, W., & Hong, J.** (2010). Varactor-tuned dual-mode bandpass filters. IEEE Transactions on Microwave Theory and Techniques, 58(8), 2213–2219. https://doi.org/10.1109/TMTT.2010.2053074

[I.54] **Long, J., Li Cui, C., Huangfu, J., & Ran, L.** (2011). A tunable microstrip bandpass filter with two independently adjustable transmission zeros. IEEE Microwave and Wireless Components Letters, 21(2), 74–76.

[I.55] **Al-Yasir, Y. I. A., Parchin, N. O., Alabdallah, A., Abdulkhaleq, A. M., Abd-Alhameed, R. A., & Noras, J. M.** (2019). Design of bandpass tunable filter for green flexible RF for 5G. In Proceedings of the 2019 IEEE 2nd 5G World Forum

(5GWF), Dresden, Germany, 30 September– 2October 2019. https://doi.org/10.1109/5GWF.2019.8911652

[I.56] **Ebrahimi, A., Baum, T., Scott, J., & Ghorbani, K.** (2018). Continuously tunable dual-mode bandstop filter. IEEE Microwave and Wireless Components Letters, 28(5), 419–421

[I.57] **Chen, C., Wang, G., & Li, J.** (2018). Microstrip switchable and fully tunable bandpass filter with continuous frequency tuning range. IEEE Microwave and Wireless Components Letters, 28(6), 500–502.

[I.58] **Chen, F., Li, R., & Chen, J.** (2018). Tunable dual-band bandpass-to-bandstop filter using p-i-n diodes and varactors. IEEE Access, 6, 46058–46065.

[I.59] **Lu, D., Tang, X., Barker, N., & Feng, Y.** (2018). Single-band and switchable dual/single-band tunable BPFs with predefined tuning range, bandwidth, and selectivity. IEEE Microwave and Wireless Components Letters, 66(12), 1215–1227.

[I.60] **Al-Yasir, Y., Parchin, N. O., Rachman, Z.-A. S. A., Ullah, A., & Abd-Alhameed, R.** (2019). Compact tunable microstrip filter with wide-stopband restriction and wide tuning range for 4G and 5G applications. In Proceedings of the IET's Antennas and Propagation Conference, Birmingham, UK, 11–12 November 2019, pp. 1–6.

[I.61] **Iqbal, A., Tiang, J. J., Lee, C. K., Mallat, N. K., & Wong, S. W.** (2020). Dual-band half-mode substrate integrated waveguide filter with independently tunable bands. IEEE Transactions on Circuits and Systems II: Express Briefs, 67(4), 285–289.

CHAPITRE II:

Metamaterials: an Overview Process, and Applications

II.1. Introduction

Metamaterials (MMTs) possess extraordinary properties that often appear to belong to the realm of science fiction, enabling groundbreaking applications such as microwave filters, invisibility cloaks, and advanced "smart" antennas. What sets these materials apart is their unique structure, which allows them to challenge and redefine conventional electromagnetic principles. As the name implies, metamaterials are artificially engineered materials designed to exhibit physical properties that surpass those found in nature. These materials go "beyond" the limitations of natural substances, offering unprecedented capabilities in electromagnetism and optics. Among their remarkable features are phenomena such as a negative refractive index and the inverted Doppler effect, which have captured the attention of researchers and engineers alike.

This chapter provides a comprehensive overview of metamaterials, serving as a foundation for understanding and implementing the structures discussed in subsequent chapters. It begins with a general introduction to the fundamental concepts of metamaterials, including their defining characteristics, such as the negative refractive index and their unique electromagnetic behavior. Following this, the chapter delves into the theory of metamaterial transmission lines, highlighting the distinctions between right-handed (RH), left-handed (LH), and composite right/left-handed (CRLH) transmission lines. Finally, the chapter concludes with an exploration of various practical applications of metamaterials, showcasing their transformative potential across multiple fields.

II.2. Origins of metamaterials

The concept of artificial materials with tailored electromagnetic properties traces its roots back to the late 19th century. One of the earliest documented efforts in this field was conducted by J.C. Bose in 1898, who performed pioneering experiments on microwave polarization. Bose demonstrated that the polarization of electromagnetic waves could be rotated using twisted synthetic fibers immersed in a liquid medium, such as sugar syrup [II.1]. This groundbreaking work marked the first step toward understanding and manipulating wave propagation in artificial structures.

In the early 20th century, further theoretical advancements were made by H. Lamb and H.C. Pocklington (1904–1905), who explored the behavior of phase velocity and group velocity in mechanical systems. They demonstrated that, under specific conditions, these velocities could propagate in opposite directions, depending on the configuration of charged chains [II.2, II.3]. This discovery laid the groundwork for understanding wave dynamics in structured materials.

In 1914, Lindman expanded on these ideas by investigating chiral artificial media, which consisted of randomly oriented spiral threads embedded within a host medium [II.4]. His work provided early insights into the design of materials with unique electromagnetic responses, particularly in the context of wave polarization and propagation.

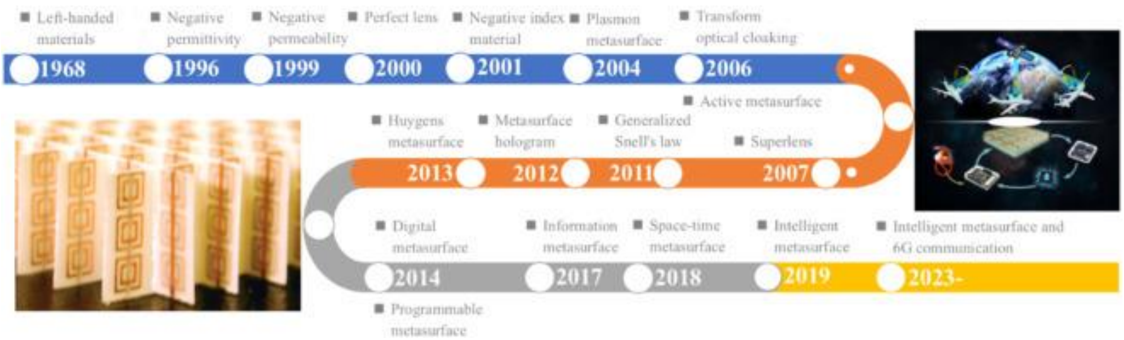

Figure II-1: Evolution of metamaterials and metasurfaces: from fundamental discoveries to intelligent 6G applications.

This figure (II-1) captures the journey of how metamaterials and metasurfaces have evolved over the years. It all began with the discovery of unusual materials that had strange properties like negative permittivity, which opened up new doors in physics [II.5]. Over time, these theoretical ideas turned into real-world applications, such as perfect lenses and optical cloaking technologies [II.6]. Later, researchers developed even smarter metasurfaces capable of precisely controlling electromagnetic waves. Today, the focus has shifted toward combining these surfaces with artificial intelligence to meet the demands of 6G networks, promising a real revolution in smart communications.

A significant milestone in the field was achieved in 1944 when L.I. Mandelshtam conducted the first theoretical study on negative refraction. His work introduced the concept of negative refractive index and included the first diagram illustrating this phenomenon, as shown in Figure (II-2)[II.7]. Mandelshtam's contributions were instrumental in shaping the modern understanding of metamaterials and their potential applications.

These early investigations collectively laid the foundation for the development of metamaterials, which have since revolutionized fields such as optics, electromagnetics, and material science.

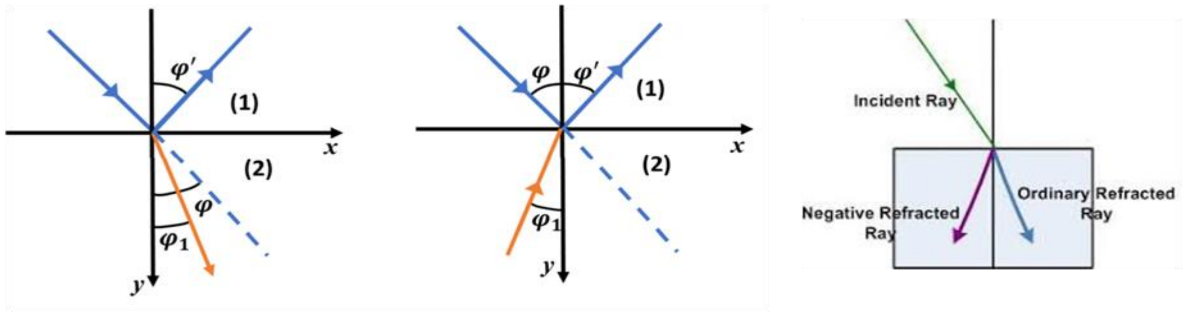

Figure II-2: L.I. Mandelshtam presentation of the first schematic diagram of negative refraction in 1950.

Negative Refraction and Early Developments in Metamaterials According to L.I. Mandelshtam, negative refraction is a phenomenon that arises from the opposition between phase velocity and group velocity, as illustrated in Figure II-2. Mandelshtam argued that, despite its seemingly counterintuitive nature, this phenomenon is physically valid because the phase itself does not carry energy [II.7]. This insight laid the groundwork for understanding the unique behavior of waves in materials with unconventional electromagnetic properties.

The concept of artificial dielectrics was first introduced by W.E. Kock in 1948. Kock proposed the idea of creating lightweight dielectric lenses by embedding conductive spheres, disks, and ribbons in a regular matrix, thereby controlling the effective refractive index of the artificial medium [II.8]. This approach marked a significant step toward engineering materials with tailored electromagnetic responses.

In 1951, Malyuzhinets provided experimental evidence for one-dimensional (1D) infinite periodic structures that supported "backward" waves. These structures consisted of series capacitors connected in parallel with inductors, demonstrating the feasibility of designing materials with unconventional wave propagation characteristics [II.9]. Shortly thereafter, in 1957, Sivukhin explored the relationship between negative permittivity (ε) and permeability (μ) and their role in enabling negative refraction, further advancing the theoretical understanding of these phenomena [II.10].

In 1959, Pafomov published a detailed study on the Doppler effect and Vavilov-Cherenkov radiation in media with negative ε and μ [II.11]. His work provided deeper insights into the behavior of electromagnetic waves in such unconventional materials. Building on these foundations, the Russian physicist Victor G. Veselago conducted a comprehensive theoretical investigation in 1968 into the electromagnetic properties of materials with simultaneously negative ε and μ. Veselago's work established the fundamental principles of wave propagation in these hypothetical media, as depicted in Figure II-3, and laid the theoretical groundwork for the field of metamaterials [II.5].

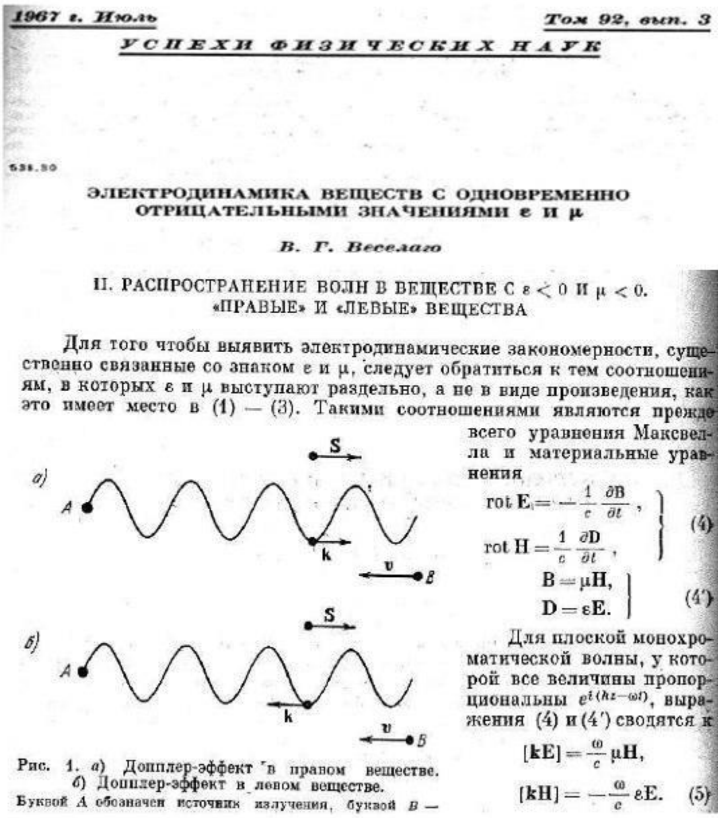

1967 г. Июль *Том 92, вып. 3*

УСПЕХИ ФИЗИЧЕСКИХ НАУК

538.30

ЭЛЕКТРОДИНАМИКА ВЕЩЕСТВ С ОДНОВРЕМЕННО ОТРИЦАТЕЛЬНЫМИ ЗНАЧЕНИЯМИ ε И μ

В. Г. Веселаго

II. РАСПРОСТРАНЕНИЕ ВОЛН В ВЕЩЕСТВЕ С $\varepsilon < 0$ И $\mu < 0$. «ПРАВЫЕ» И «ЛЕВЫЕ» ВЕЩЕСТВА

Для того чтобы выявить электродинамические закономерности, существенно связанные со знаком ε и μ, следует обратиться к тем соотношениям, в которых ε и μ выступают раздельно, а не в виде произведения, как это имеет место в (1) — (3). Такими соотношениями являются прежде всего уравнения Максвелла и материальные уравнения

$$\operatorname{rot} \mathbf{E} = -\frac{1}{c}\frac{\partial \mathbf{B}}{\partial t}, \quad \operatorname{rot} \mathbf{H} = \frac{1}{c}\frac{\partial \mathbf{D}}{\partial t}, \qquad (4)$$

$$\mathbf{B} = \mu \mathbf{H}, \quad \mathbf{D} = \varepsilon \mathbf{E}. \qquad (4')$$

Для плоской монохроматической волны, у которой все величины пропорциональны $e^{i(kz-\omega t)}$, выражения (4) и (4′) сводятся к

$$[\mathbf{kE}] = \frac{\omega}{c}\mu\mathbf{H}, \quad [\mathbf{kH}] = -\frac{\omega}{c}\varepsilon\mathbf{E}. \qquad (5)$$

Рис. 1. *а*) Доплер-эффект в правом веществе. *б*) Доплер-эффект в левом веществе. Буквой *A* обозначен источник излучения, буквой *B* —

Figure II-3: Professor V.G.Veselago's theory of left-hand propagation.

II.3. Early theoretical foundations and the first realization of metamaterials

Until the 1960s, all published works on metamaterials were purely theoretical. While the theoretical foundations of these materials were well understood, no physical realization of a metamaterial had been achieved. This changed when J. Brown and W. Rotman investigated wire networks in the 1960s, which were used to produce RF lenses using artificial dielectric materials [II.12]. Around the same time, S. Schelkunoff explored resonant magnetic rings (loops), which were later improved and utilized in the 1980s and 1990s [II.13].

II.3.1. The first Realization of metamaterials

It was observed that wave propagation is only possible in media that are either doubly negative (negative permittivity and permeability) or doubly positive. Conversely, media with only one negative parameter (either permittivity or permeability) exhibit evanescent behavior. This observation spurred extensive research aimed at creating doubly negative metamaterials capable of operating across the entire electromagnetic spectrum, from microwaves to optics.

In 1999, J. Pendry proposed the concept of a double resonant ring structure, which is widely regarded as the foundation of the first practical metamaterial [II.14]. Shortly after, R.A. Shelby successfully realized the first medium with negative electromagnetic parameters [II.15]. Interestingly, while the individual components of this realization had been understood for some time, no previous attempts had been made to combine them into a functional material.

The quest for a superlens, initiated by J.B. Pendry in 2000, became a major driving force behind metamaterial research [II.6]. The superlens theory, which focuses on resolving details smaller than the wavelength of light, faced challenges due to operational losses. Additionally, achieving isotropic dispersion properties in doubly negative metamaterials proved difficult. To address these challenges, researchers explored the use of simpler negative-index materials.

In 2000, D.R. Smith demonstrated that a composite material consisting of split-ring resonators (SRRs) and continuous metal wires could exhibit negative permittivity and permeability, resulting in a negative refractive index [II.16]. This marked the creation of the Veselago medium, achieved by combining these two structures into a periodic system. The medium displayed a negative refractive index around the resonant frequency of the SRRs. Efforts were also made to extend these metamaterials to the infrared and visible spectra, requiring nanoscale precision. For example, in the visible spectrum (wavelength ~500 nm), the periodicity of the structures had to be on the order of 50 nm, with metallic patterns as small as 10 nm.

In recent years, advances in synthesis and manufacturing techniques have enabled the development of structures and composite materials that either mimic known material responses or exhibit entirely new properties not found in nature. In 2002, C. Caloz, T. Itoh, and Eleftheriades introduced a new class of non-resonant metamaterials, which offered the advantage of minimized losses compared to resonant models (see Figure II-4) [II.17].

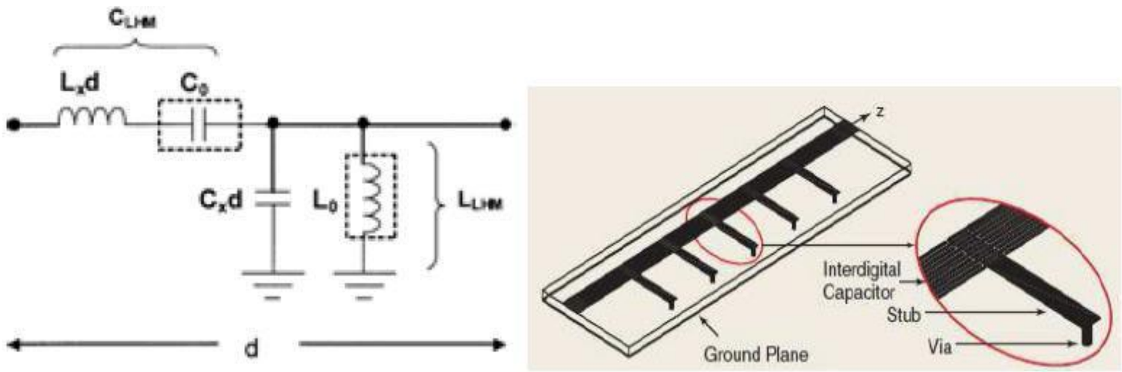

Figure II-4: The non-resonant material structure in the left-hand developed by of C. Caloz .

II.4. Categorization of materials

In the field of microwaves, we classify materials into four groups based on the sign of their permittivity and permeability, as shown in Figure II-5 [II.18].

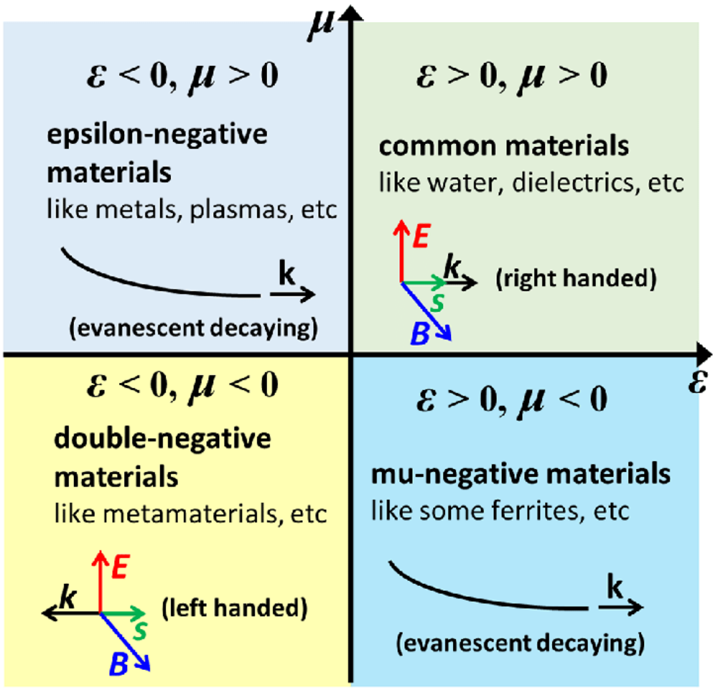

Figure II-5: Permittivity and permeability signsareused to classify materials**.**

The first three materials are not entirely original. Inparticular, right-handedmaterials (RHM), such as isotropic dielectric materials, conform to the zone (+, +) where the media are doubly positive (DPS) [II.5]. Negative permittivity (ENG, (-, +) and permeability (MNG, (+, -) media have also been [II.16,II.19].

II.5. Foundations and classification of metamaterials

The principles underlying metamaterials have been rooted in electromagnetism for decades. The Drude-Lorentz model, which describes the behavior of most natural materials, predicts that permittivity becomes negative below the plasma frequency [II.20]. Similarly, ferrimagnetic materials exhibit regions of negative permeability due to their strong magnetic interactions [II.21]. Natural materials can be classified into three categories based on their electromagnetic properties: double-positive (DPS), epsilon-negative (ENG), and mu-negative (MNG) materials. However, doubly negative media (DNG), characterized by simultaneously negative permittivity and permeability, do not exist in nature. These materials, often referred to as left-handed materials (LHM), are the basis of metamaterials [II.5].

In the literature, several terms are used interchangeably to describe left-handed materials (LHM), each emphasizing a specific property or characteristic [II.22,II.19]:

- ✓ **Left-handed materials (LHM):** This term highlights the unique property of metamaterials where the phase velocity and group velocity propagate in opposite directions
- ✓ **Negative refractive index materials:** These materials exhibit a negative effective refractive index for electromagnetic waves within a specific frequency range.
- ✓ **Double negative materials:** This name refers to the simultaneous negativity of permittivity and permeability in the material.
- ✓ **Veselago medium:** Named after Victor Veselago, who first theorized the concept of materials with negative refractive index, this term pays tribute to his foundational work.
- ✓ **Backward wave materials:** This term emphasizes the backward propagation of waves in such materials.

II.6. Effective homogeneous case

Metamaterials are often described as pseudo-homogeneous artificial materials with electromagnetic properties not found in nature. However, this definition has sparked debate, particularly regarding the terms "artificial" and "not available in nature," as many modern materials are artificially engineered, and their properties may not occur naturally. A. Shivola aptly summarizes the challenges in defining metamaterials, emphasizing the need for a clear and precise description [II.23].

The term "pseudo-homogeneous" implies that the unit cell size (P) of the material must be significantly smaller than the guided wavelength λ_g at the operating frequency. This ensures that the material appears homogeneous to the propagating wave, minimizing diffraction effects. A widely accepted criterion for homogeneity is P < $\lambda_g/4$, this limit guarantees that diffraction phenomena can be ignored.In other words, the size of the basic unit cell "P" must be smaller than the guided wavelengh g in pseudo-homogeneous matrial over a frequency band (see Figure II-6) [II.18].

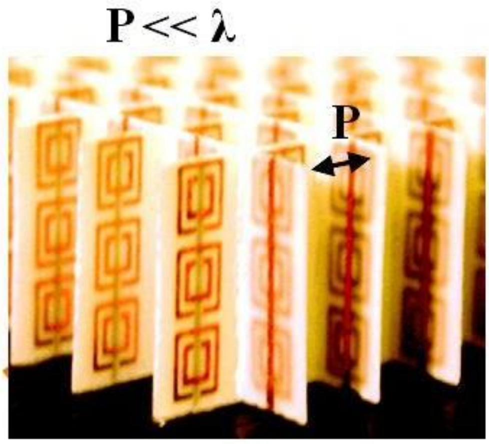

Figure II-6: From article[16], a pseudo homogeneous structure pf a periodic network resonating rings and wires.

When a pencil is partially inserted into a glass of water, the positive refractive index produces a "folded" image [II.21]. Light oran electromagnetic wave of the right frequency will be forced to deflect in the opposite direction by a "metaliquid" [II.15]. While awaiting its experimental synthesis, one can evoke a mental image of a pencil immersed in such a liquid (Figure II-7).

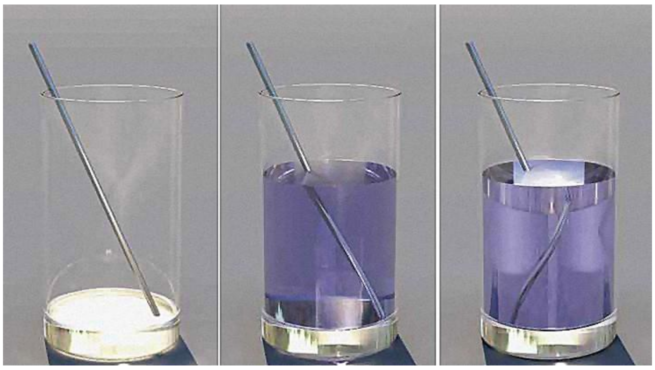

(a) (b) (c)

Figure II-7: (a) an empty cup with no cracks(a normal refractive) (b) A medium with a normal refractive index. (c) a liquid metamaterial with a negative refractive index.

The statement "electromagnetic properties not found in nature" can be somewhat misleading [II.5]. It is possible to envision numerous new structures being categorized as "metamaterials" based solely on this criterion. Since metamaterials are pseudo-homogeneous, it is adequate to characterize their magnetic permeability (μ) and electrical permittivity (ε). The signs of these two parameters, which constitute the refractive index (n), can then be utilized to classify conventional materials. A key characteristic that has garnered significant attention for metamaterials is the simultaneous presence of negative permeability and permittivity. This property is defined by the following relationship for the refractive index [II.5]:

$$n = \sqrt{\varepsilon_r \mu_r} \tag{II.1}$$

When both(μ) and (ε) are negative, the refractive index becomes negative, a phenomenon not observed in naturally occurring materials and a defining feature of metamaterials.

II.7. Negative index materials

The refractive index, denoted as "n", is a fundamental property that characterizes materials [II.21]. According to Snell-Descartes' laws, the refractive index determines the angles of reflection and refraction of an incident light ray [II.19]. In conventional materials, the refractive index is typically greater than or equal to 1 [II.18]. However, in the case of metamaterials, it is possible to achieve a refractive index less than 1, or even 0 [II. 21]. This unique property implies that the transmitted ray may appear on the same side of the normal as the incident ray, a phenomenon not observed in natural materials [II.19].

The refractive index (n) is intrinsically linked to two key material parameters: the magnetic permeability (μ) and the electric permittivity (ε) [II.18].These parameters are related to the refractive index through the following equation:

$$n = \sqrt{(\mu \cdot \varepsilon)} \tag{II.2}$$

In most natural materials, the relative permittivity εr and relative permeability μ_r are complex quantities due to inherent losses, with their real parts being positive. As a result, the sign of the refractive index is typically unambiguous. However, in the case of metamaterials, where both the real parts of (ε) and (μ) can be negative simultaneously, the situation becomes more nuanced. Specifically, when ($(\varepsilon_r) < 0$) and ($(\mu_r) < 0$), the refractive index (n) can take on a negative value,meaning ($n < 0$).

To better understand this, we can represent (ε) and (μ) in the complex plane,as seen in Figure II-8, Let:

$$\varepsilon_r = |\varepsilon_r| \cdot e^{i\varphi_\varepsilon} \quad \text{and} \quad \mu_r = |\mu_r| \cdot e^{i\varphi_\mu} \tag{II.3}$$

Here, (φ_ε) and(φ_μ) represent the phase angles of (ε_r)and (μ_r) , respectively. The refractive index can then be expressed as:

$$n = \sqrt{(|\varepsilon_r| \cdot |\mu_r|) \cdot e^{\frac{1}{2}i(\varphi_\mu + \varphi_\varepsilon)}} \tag{II.4}$$

For passive media, the imaginary parts of (ε_r)and (μ_r) must be positive, which constrains the phase angles (φ_ε) and (φ_μ)to the range [0, π]. Consequently, the phase angle of the refractive index "n" also lies within the same range, [0, π].

In the case of a doubly negative medium, where both ((ε)< 0) and ((μ) < 0), the phase angles (φ_ε)and (φ_μ)are restricted to the range [$\frac{\pi}{2}$, π]. This results in a negative real part for the refractive index "n", as the combined phase angle ((φ_ε)+ φ_μ)/2) falls within [$\frac{\pi}{2}$, π].

To illustrate this, consider the following example where both (ε)and (μ) are negative:

$$\varepsilon_r(\omega) = |\varepsilon_r| \cdot e^{-i\pi} \tag{II.5}$$

$$\mu_r(\omega) = |\mu_r| \cdot e^{-i\pi} \tag{II.6}$$

Substituting these into the expression for the refractive index yields:

$$n = \sqrt{|\varepsilon_r| \cdot |\mu_r|}\, e^{-i\pi} = -\sqrt{(|\varepsilon_r| \cdot |\mu_r|\,)} \tag{II.7}$$

This clearly demonstrates that when both (ε) and (μ) are negative, the refractive index "n" becomes negative. This unique property of negative index materials is a hallmark of metamaterials and has significant implications for their applications in optics and electromagnetics.

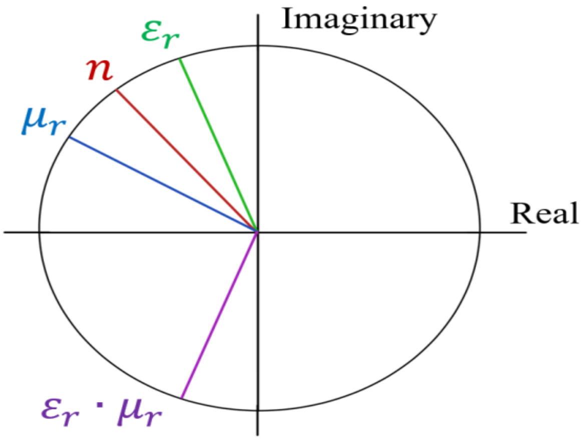

Figure II-8 : The arguments of ε_r, and μ_r, as well as their product, are represented in the complexplane.

II.7.1. Negative refractive index in left-handed materials (LHM)

It is evident from the above discussion that the refractive index of Left-Handed Materials (LHM) is negative relative to that of a vacuum [II.5, II.6]. This unique property results in unconventional electromagnetic wave behavior, as illustrated in Figure II-9 (a). When an electromagnetic (EM) wave interacts with a negative index medium, it refracts at a negative angle relative to the normal, contrary to the positive refraction observed in conventional materials [II.5, II.15].

II.7.2. Reversal of lens functionality

In such materials, the traditional roles of convex and concave lenses are inverted [II.6]. Specifically, a convex lens, which typically converges light in conventional optics, exhibits a diverging effect in a negative index medium. Conversely, a concave lens, known for its diverging properties, demonstrates a converging effect in these materials, as depicted in Figures II-9 (b) and II-9 (c) [II.5, II.6].

II.7.3. Applications in superlenses

This phenomenon has significant implications for overcoming the limitations of traditional optical systems. By leveraging the properties of negative index materials, researchers have developed advanced structures known as superlenses. These superlenses are capable of achieving resolutions beyond the diffraction limit, opening new possibilities in fields such as nanophotonics, microscopy, and medical imaging [II. 24, II. 25, II. 22].

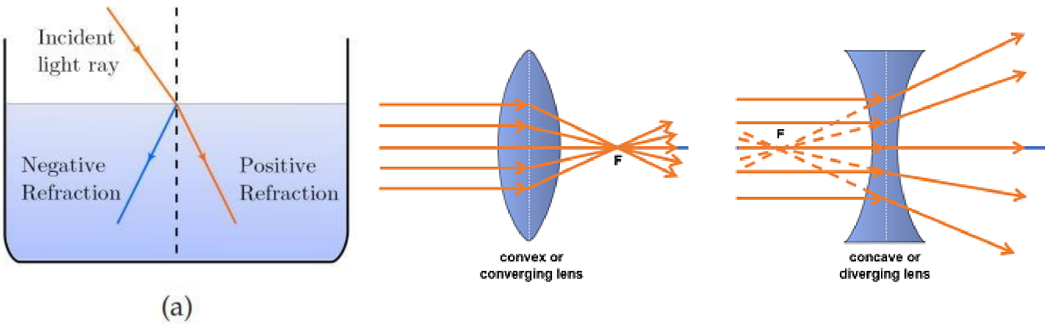

(a) **(b)** **(c)**

Figure II-9: (a) incident EM wave in a medium based on metamaterial. (b) convex lens has a diverging effect. (c) concave lens has a converging effect.

II.8. Electromagnetic propagation in a homogeneous medium

Maxwell's equations can be expressed in the following form for a monochromatic electromagnetic wave propagating in a homogeneous medium [II.21, II.26]:

$$\vec{\nabla}\times \vec{E} = -\frac{\partial \vec{B}}{\partial \vec{t}} \qquad (II.8)$$

$$\vec{\nabla}\times \vec{H} = \frac{\partial \vec{D}}{\partial \vec{t}} \qquad (II.9)$$

Where:

- ✓ $\vec{E}$: represents the electric field.
- ✓ $\vec{H}$: represents the magnetic field.
- ✓ $\vec{B}$:represents the magnetic induction.
- ✓ $\vec{D}$:represents the electric induction.
- ✓ μ:is the magnetic permeability.
- ✓ ε :is the electrical permittivity.

The relationships between these quantities are given by:

$$\vec{B} = \mu \vec{H} \text{ and } \vec{D} = \varepsilon \vec{E} \qquad (II.10)$$

The relative permittivity and permeability of the propagation medium are denoted by ε_r and , μ_r respectively, while the permittivity and permeability of free space (vacum) are represented by ε_0 and μ_0.These are related as follows:

$$\mu = \mu_r \times \mu_0 \quad \text{and} \quad \varepsilon = \varepsilon_r \times \varepsilon_0 \qquad (II.11)$$

For a plane wave propagating in the z-direction, the electromagnetic fields ($\vec{E}$) and ($\vec{H}$) exhibit both temporal ($e^{j\omega t}$)and spatial ($e^{(-j\gamma z)}$) dependencies. The fields can be expressed as:

$$\vec{E} = \vec{E_0} e^{j\omega t} e^{(-j\gamma z)} \quad \text{and} \quad \vec{H} = \vec{H_0} e^{j\omega t} e^{(-j\gamma z)} \qquad (II.12)$$

Here, $\vec{E_0}$ is the amplitude of the electric field, and ω is the angular frequency, defined as:

$$\omega = 2\pi f \qquad (II.13)$$

where f is the frequency of the wave [II.27].

The constant γ is known as the propagation constant and is defined as:

$$\Gamma = \alpha + j\beta \qquad (II.14)$$

Where α represents the attenuation constant, and β represents the phase constant [II.28]. Based on the form of γ ,three distinct cases can be identified:

- Purely Real Propagation Constant $\gamma = \alpha$:

The electromagnetic wave is evanescent, and its amplitude decays exponentially during propagation.

- Purely Imaginary Propagation Constant $\gamma = j\beta$:

The electromagnetic wave propagates without attenuation.

- Complex Propagation Constant $\gamma = \alpha + j\beta$:

The electromagnetic wave propagates with a loss term, characterized by both attenuation and phase shift [II.29].

In the case of a loss less medium, where α the propagation equations simplify to:

$$\vec{E}=\overrightarrow{E_0}\, e^{j\omega t}e^{-jkz} \text{ and } \vec{H}= \overrightarrow{H_0}\, e^{j\omega t}e^{-jkz} \qquad (II.15)$$

These equations describe the propagation of electromagnetic waves in a homogeneous medium, highlighting the interplay between the electric and magnetic fields as governed by Maxwell's equations.

With k the wave vector, knowing that in the hypothesis of a TEM propagation:

$$k = \beta \qquad (II.16)$$

We can rewrite Maxwell's equations in this form using equations (II. 8) , (II. 9)and (II. 10):

$$\vec{K} \times \vec{E} = \omega\mu \vec{H} \quad and \quad \vec{K} \times \vec{H}= -\omega\varepsilon\vec{E} \qquad (II.17)$$

II.9. Electromagnetic wave propagation in double-negative medium (metamaterials)

we can deduce from equations (II.18) that when both the electric permittivity (ε) and magnetic permeability (μ) are positive, the vectors $\vec{E}$, $\vec{H}$ and $\vec{K}$ form a direct or right-handed triplet (as shown in Figure II-10). Here, the vector S represents the Poynting vector, which describes the surface power density of the electromagnetic wave, expressed by the relation:

$$\vec{S}= \frac{1}{2}\vec{E}\times\vec{H}^* \qquad (II\text{-}18)$$

As a result, the vectors $\vec{S}$ and $\vec{K}$ propagate in the same direction.

On the other hand, another scenario that satisfies this equation occurs when both ε and μ are simultaneously negative. In this case, the vectors $\vec{E}$, $\vec{H}$ and $\vec{K}$ form an indirect or left-handed triplet (as illustrated in Figure(II-10). This is known as Veselago's scientific theory, first proposed in 1964 [II.5]. These materials are termed "metamaterials" because the Russian researcher discovered certain physical properties of such substances that do not exist in nature.

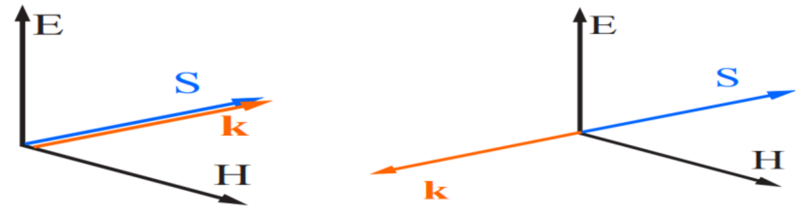

Figure II-10: Vector representation of a plane wave.

Equation (II. 19) defines the phase velocity, while equation (II. 20) defines the group velocity (II. 20)[II.30].

Since the three vectors $\vec{E}$, $\vec{H}$ and $\vec{K}$ form an indirect triplet, the wave's phase and group velocity are in opposite directions (see Figure II-10):

$$v_\varphi = \frac{\omega}{k} \tag{II. 19}$$

$$v_g = \frac{\partial\omega}{\partial k} \tag{II. 20}$$

Since the three vectors , and form an indirect triplet, the wave's phase and group velocity are in opposite directions (see Figure II-11)

$$\begin{cases} \textbf{Right−handed meduim}: v\varphi>0\ (k>0)\ and\ vg>0 \\ \textbf{Left−handed meduim}: v\varphi<0\ (k<0) and\ vg>0 \end{cases} \tag{II. 21}$$

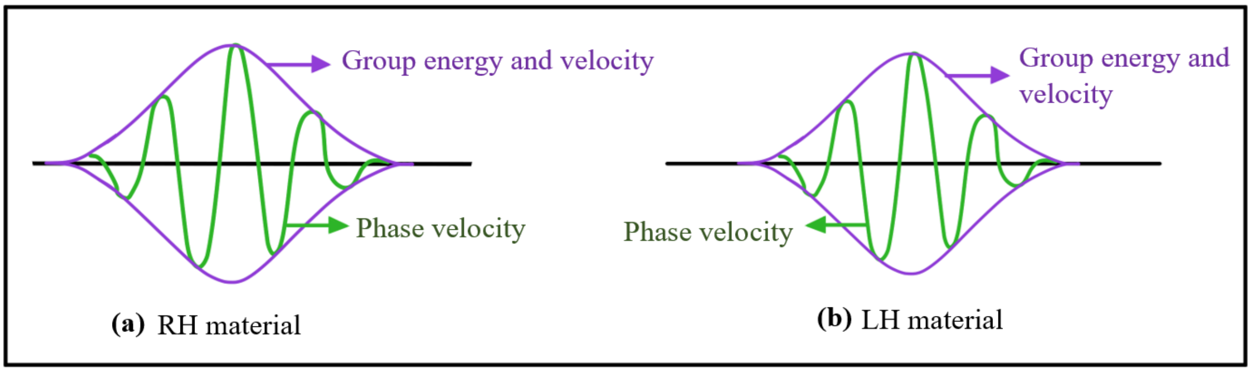

Figure II-11: Phase and energy propagaion in a traditional material and a left-handed material.

Veselago predicted that a medium with simultaneously negative permittivity (ε) and permeability (μ) would exhibit several unique and counterintuitive properties. These include:

- **Reversed doppler effect:** Unlike in conventional materials, the observed frequency of waves in such a medium would shift in the opposite direction relative to the motion of the source.
- **Reversed snell-descartes' law with a negative refractive index:** Light propagating into this medium would refract on the same side of the normal, a phenomenon characterized by a negative refractive index.
- **Reversed cerenkov radiation:** The Cerenkov effect, which describes the emission of electromagnetic radiation when a charged particle moves through a medium at a speed exceeding the phase velocity of light, would also be reversed in a left-handed medium [II.5].

Cerenkov radiation is a visible form of electromagnetic radiation emitted when charged particles travel through a dielectric medium at a velocity greater than the speed of light in that medium[II.21]. In conventional materials (where the refractive index (n > 0), the spherical wavefront generated by the particle lags behind its motion, creating a shockwave directed at an angle (θ< 90°) relative to the particle's velocity. This angle is formed between the Poynting vector of the emitted wave and the direction of the particle's motion. However, in a left-handed medium, this behavior is inverted, as illustrated in Figure II-11 (a) and discussed in [II.31].
The angle (θ) associated with Cerenkov radiation is determined by the following relationship:

$$\cos\theta = \frac{\mathrm{c}}{\mathrm{n(\omega)v}} \qquad (\mathrm{II}.22)$$

Here, (c) represents the speed of light in a vacuum, and (v) denotes the speed of the charged particle.
In a conventional medium with a positive refractive index (n > 0), the Cerenkov radiation wavefront propagates in a direction opposite to the particle's motion, forming an angle (θ < 90°) with the particle's velocity. However, in a medium with a negative refractive index (n < 0), the behavior of Cerenkov radiation is reversed [II.5]. The wavefront retro-propagates, meaning it travels in the same direction as the particle's motion at a speed of ($c/|n|$). Consequently, the angle (θ) between the wavefront and the particle's velocity becomes greater than (90°), as illustrated in Figure II-12 (b) [II.32].
It is important to note that materials exhibiting a negative refractive index are only active within specific frequency ranges [II.31]. Since Cerenkov radiation occurs across a broad spectrum of frequencies, some of which correspond to (n > 0), the wavefronts can propagate either forward or backward relative to the particle's motion, depending on the frequency.

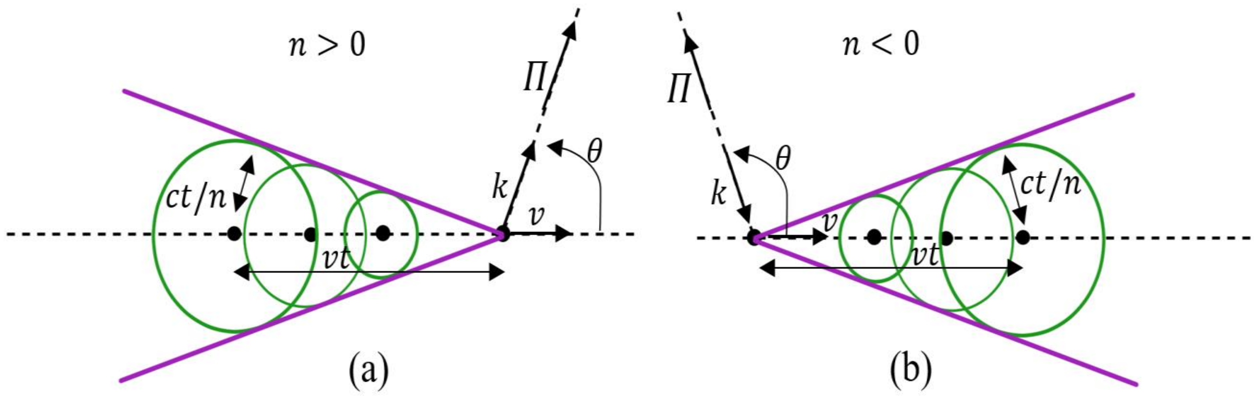

Figure II-12: Illustration of the Cerenkov effect. (a) Conventional medium. (b) Left-handed medium.

II.9.1. The reversed doppler effect

The inversion of the Doppler effect is another remarkable phenomenon observed in the propagation of electromagnetic waves within a left-handed medium, as predicted by Veselago [II.5]. To illustrate this, consider a source S moving along the Oz -axis and emitting an electromagnetic wave with an angular frequency ω_0 as depicted in Figure (II-13). If the source moves at a velocity $v_s = \frac{z}{t}$ in the positive z direction, the observed Doppler frequency ω_{Doppler} can be expressed as:

$$\omega_{\text{Doppler}} = \omega_0 - \Delta\omega \quad with \quad \Delta\omega = \omega_0 \frac{n\, v_s}{c} \qquad (II.23)$$

Here, (c) represents the speed of light in a vacuum, and "n" denotes the refractive index of the medium.

In conventional materials ($n > 0$), the Doppler effect causes the observed frequency to increase when the source moves toward the observer and decrease when it moves away [II.5]. However, in a left-handed medium ($n < 0$), this behavior is inverted [II.6]. Specifically, the frequency observed by a detector positioned in the direction of the source's motion will decrease, while the frequency observed in the opposite direction will increase [II.15]. This reversal is a direct consequence of the negative refractive index, which fundamentally alters the wave propagation dynamics [II.5].

This phenomenon underscores the unique and counterintuitive properties of left-handed media, further validating Veselago's theoretical predictions [II.6].

$$\omega_{\text{observed}} = \omega_0 - \Delta\omega \qquad (II.24)$$

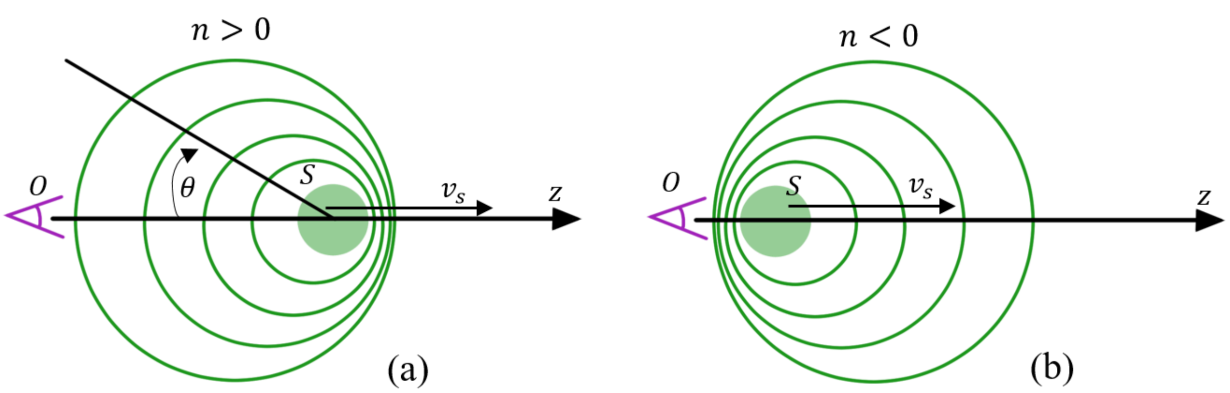

Figure II-13: The doppler effect for: (a) RH media. (b) LH media.

II.9.2. The reversed snell's law with a negative refractive index

The refractive index of a material is calculated using Equation (II.1). The propagation constant is determined as follows

$$k = nk_0 = n\frac{w}{c} \tag{II.25}$$

Given that k < 0,it can be concluded that the refractive index(n) of a double-negative (DNG) material is negative.

As a result of this finding, Snell's law can be generalized to account for the possibility of an interface between a DNG material and a double-positive (DPS) material [II.5]:

$$n_i \sin(\theta_i) = n_t \sin(\theta_t) \tag{II.26}$$

Here:

- n_i are n_t the refractive indices of the materials supporting the incident and transmitted waves, respectively.

- $\theta_i$and θ_t are the angles of incidence and transmission, measured with respect to the normal at the interface between the two materials [II.15].

A distinction can be made between two cases:

Positive refraction: This occurs when both materials have the same sign of refractive index (i.e., both positive or both negative). In this case, the angles θ_i and θ_t, are both positive (see Figure II-14 (a)).

Negative refraction : If the sign softhe two materials vary,the refraction is negative since one of the two angles, θ_i and θ_t would be negative [II.32], as displayed in Figure II-14 (b).

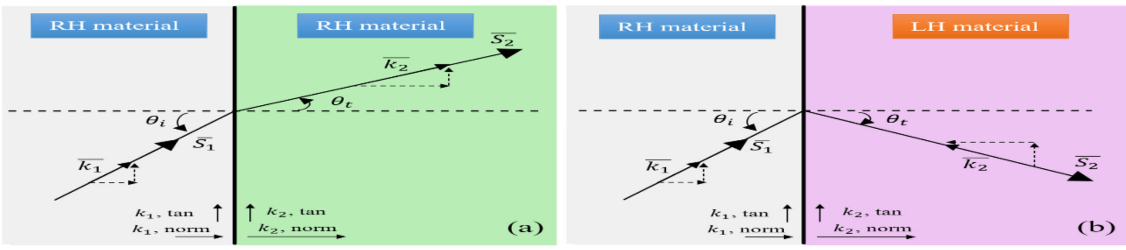

Figure II-14: Electromagnetic wave refraction at the interface between two different materials. (a) positive refraction. (b) negative refraction.

II.10. Theory of the metamaterial transmission line

Most naturally occurring materials exhibit positive permittivity (ε) and permeability.(μ) Conventional right-handed materials (RHMs), such as standard transmission lines, inherently support these positive electromagnetic parameters. In contrast,metamaterial transmission linesrepresent a class of one-dimensional artificial structures engineered to achieve unique properties, including negative refractive indicesor left-handed (LH) behavior, which are not observed in natural media [II.18].

II.10.1. Mathematical modeling of transmission lines

A transmission line supporting transverse electromagnetic (TEM) wave propagation can be modeled as a distributed parameter system [II.5]. For a differential line segment (Δz):

- Series impedance: $\frac{z}{\Delta z}$ includes inductance L and resistance R.
- Shunt admittance: $\frac{y}{\Delta y}$ includes capacitance C and conductance G .

In anideal lossless system (R = 0), (G = 0), the governing telegrapher's equations simplify to:

$$\frac{\partial v}{\partial z} = -L\frac{\partial I}{\partial t} \text{ and } ,\frac{\partial I}{\partial z} = -C\frac{\partial v}{\partial t} \qquad (II.27)$$

where V and I represent the voltage and current along the line, respectively [II.30].

II.10.2. Significance of metamaterial transmission lines

- ✓ **Negative refractive index:** Achieved when both (ε) and (μ) are negative, enabling phenomena like:backward wave propagation [II.5].
- ✓ **Miniaturization:** LH transmission lines allow compact device designs by exploiting phase-advance properties [II.33].
- ✓ **Frequency selectivity:** Tunable resonant frequencies enable applications in filters, sensors, and antennas [II.34].

Vesgalo reveals in his paper that the cerenkov effect is also revesed in a left-hand meduim[II.5]. additionally there are other studies that have presented theories and experiments on negative refraction,such as the work of pendry [II.6] and shelby [II.15].

This framework bridges conventional transmission line theory with advanced metamaterial concepts, paving the way for innovative electromagnetic devices.

II.10.3. Right-handed transmission line

To better understand the properties and characteristics of metamaterials in the microwave domain, C. Caloz, T. Itoh [II.35, II.18], and G. Eleftheriades [II.36] proposed a novel approach in 2002 based on transmission line theory. This method utilizes a network of unit cells to model a standard transverse electromagnetic (TEM) mode propagation line or a lossy right-handed transmission line (RHTL). For simplicity, the ideal case (lossless scenario) is presented below (see Figure II-15).

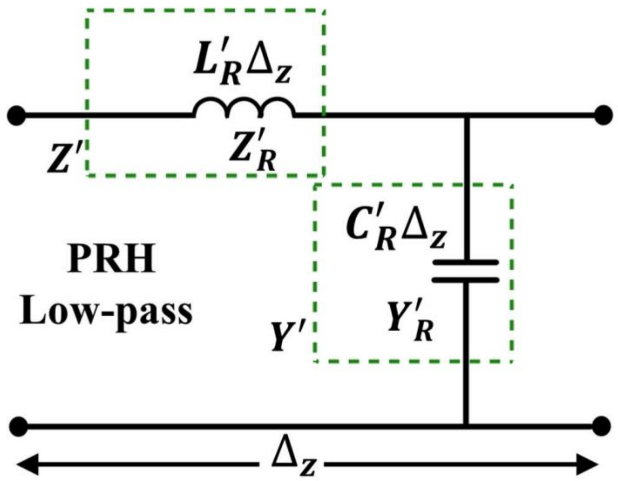

Figure II-15: Pure right-handed transmission line model [II.37].

A unit cell of a typical right-handed transmission line consists of:

- A series inductance (L)
- A shunt capacitance (C)

In practical scenarios (with losses), additional elements are introduced:

- A series resistance (R) to account for metallic losses.
- A shunt conductance (G) to represent dielectric losses.

From the equivalent circuit, the following relationships can be derived:

$$\gamma = \alpha + j\beta = \pm\sqrt{ZY} \qquad (II.28)$$

For a lossless line, Equation (II. 28) simplifies to:

$$\gamma = j\beta = \pm\sqrt{ZY} \qquad (II.29)$$

Where:

- Z is the impedance of the series elements:

$$Z = j\omega L \tag{II.30}$$

- Y is theadmittanceof the shunted elements

$$Y = j\omega C \tag{II.31}$$

- $\beta = \omega\sqrt{LC}$ is the phase constant.

- The phase velocity v_{ph} and the group velocity v_g are given by:

$$v_{ph} = \sqrt{\frac{1}{LC}} > 0 \tag{II.32}$$

$$v_g = \sqrt{\frac{1}{LC}} > 0 \tag{II.33}$$

In this case, the phase velocity and group velocity are equal and share the same signindicating a right-handed medium[II.30] . The phase constant β of the pure right-handed transmission line, as a function of frequency, is always positive and follows the relationship: $\beta = \omega\sqrt{LC}$ [II.30].

II.10.4. Left-hand transmission line

In 2002, a research team from the University of Toronto introduced the transmission line technique for creating left-handed materials (LHMs) [II.38, II.18]. This approach is based on mapping electromagnetic field components (E and H) to their equivalent voltage and current distributions in a distributed LC network. As established in the literature [II.18], dielectric properties such as permittivity and permeability can be effectively represented using distributed LC networks. Figure II-16 illustrates a two-dimensional (2D) distributed LC network, demonstrating how these material properties correspond to the network's series impedances and distributed shunt admittances. The network consists of a series impedance X' per unit length in the X and Z' directions, as well as a shunt admittance Y' [II.18]. per unit length in the Y direction. This configuration provides a practical framework for realizing negative refractive index materials through engineered circuit elements [II.15].

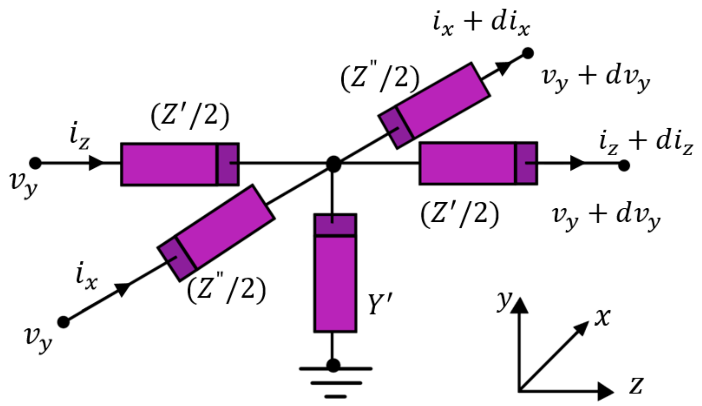

Figure II-16: Unit cell for a distributed L-C 2D network.

Since left-handed materials (LHMs) exhibit effective homogeneity, they can be accurately modeled using one-dimensional (1D) transmission lines. While wave propagation in such materials can occur in any direction, the defining feature of LHMs is the reversal of wave propagation compared to conventional materials. Drawing from the fundamental principles of transmission line theory, the essential characteristics of left-handed transmission lines can be derived straightforwardly. In an ideal scenario, the left-handed transmission line circuit, as depicted in Figure II-17, represents a dual topology of the conventional right-handed transmission line. This duality arises from the interchange of capacitive and inductive elements in the electrical model, leading to the emergence of negative permittivity and permeability—key properties that define LHMs [II.18, II.39].

The unique behavior of LHMs, including their ability to support backward wave propagation and negative refraction, makes them highly valuable for applications such as subwavelength imaging, cloaking devices, and advanced antenna design [II.22]. Furthermore, the 1D transmission line model provides a simplified yet powerful framework for analyzing and designing these materials, enabling researchers to explore their exotic electromagnetic properties with greater precision [II.40].

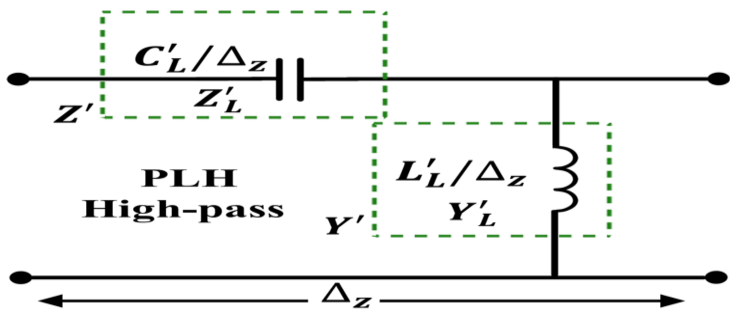

Figure II-17: Pure left-hand transmission line model [II.37].

Negative Permittivity and Permeability in Left-Handed Metamaterials (LHMs)

The unique properties of left-handed metamaterials (LHMs), such as negative permittivity (ε) and permeability (μ), raise an important question: Can the network representation's impedance (Z') and admittance (Y') parameters also be rendered negative? The answer lies in the fundamental behavior of the equivalent circuit elements. By interchanging the roles of inductance (L) and capacitance (C), it is possible to achieve negative values for these components. Specifically, the series inductor is replaced by a series capacitor, and the shunt capacitor is replaced by a shunt inductor. From an impedance perspective, this transformation results in the following relationships [II.33]:

$$Z' = \frac{1}{j\omega C} \rightarrow \mu = \frac{Z'}{j\omega} = -\frac{1}{\omega^2 C} \quad \text{(II. 34)}$$

$$Y' = \frac{1}{j\omega L} \rightarrow \varepsilon = \frac{Y'}{j\omega} = -\frac{1}{\omega^2 L} \quad \text{(II. 35)}$$

Here, Z' and Y' represent the series reactance and shunt susceptance per unit length, respectively. The negative values of L' and C' are a direct consequence of the unconventional electromagnetic properties of LHMs.

The propagation constant (β) of the left-handed transmission line can be derived as:

$$\beta = -\sqrt{-Z'Y'} = \frac{1}{\omega\sqrt{LC}} \quad \text{(II. 36)}$$

From the propagation constant, the phase velocity vph and group velocity vg can be expressed as:

$$V_{ph} = \frac{\omega}{\beta} = -\omega^2\sqrt{LC} \quad \text{(II. 37)}$$

$$V_g = \frac{\partial\omega}{\partial\beta} = \frac{1}{\frac{\partial\beta}{\partial\omega}} = \omega^2\sqrt{LC} \quad \text{(II. 38)}$$

The opposite signs of the phase velocity and group velocity indicate the presence of backward wave propagation in the left-handed transmission line network. This phenomenon is a hallmark of LHMs and is directly linked to their negative refractive index (n), which is given by:

$$n = \frac{C_0}{V_{ph}} = -\frac{C_0}{\omega^2\sqrt{LC}} < 0 \quad \text{(II. 39)}$$

C_0: is the speed of light in a vacuum.

Here, C_0 represents the speed of light in a vacuum. The negative refractive index is a defining characteristic of LHMs and enables unique applications such as subwavelength imaging and superlenses [II.5, II.6].

The ability to achieve opposite phase and group velocities, along with a negative refractive index, underscores the transformative potential of LHMs in fields such as telecommunications, optics, and microwave engineering. These materials challenge conventional electromagnetic principles and open new avenues for innovation in wave manipulation and control [II.16].

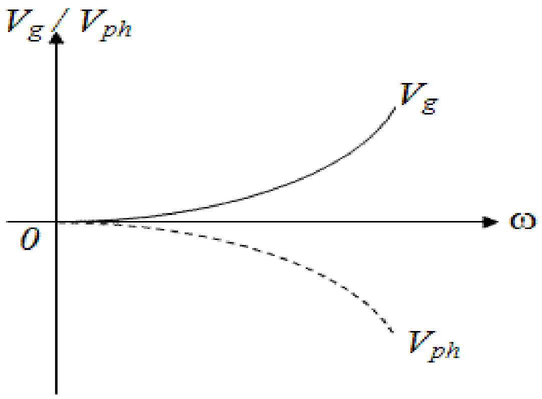

Figure II-18: group and phase velocity diagram as a function of the frequency of a metamaterial transmission line.

II.10.5. Phase constant and frequency dependence in left-handed transmission line

The phase constant (β) of a purely left-handed transmission line exhibits a negative slope across the entire frequency range, as illustrated in(Figure II-18). This behavior is derived from the equation $\beta = \frac{1}{\omega\sqrt{LC}}$, where ω is the angular frequency, and L' and C' represent the equivalent inductance and capacitance per unit length, respectively. This negative phase constant is a direct consequence of the unique electromagnetic properties of left-handed metamaterials (LHMs), which support backward wave propagation and negative refractive index [II.5].

In [II.41], a two-dimensional (2D) network of left-handed transmission lines was demonstrated to exhibit negative refraction and subwavelength focusing. The study included the fabrication of the structure, full-wavefield simulations confirming negative refraction, and the first experimental verification of focusing using transmission line implementations. For instance, an antenna design presented in [II.42] experimentally validated the existence of backward waves, a hallmark of LHMs. Additionally, applications such as leaky-wave antennas [II.42, II.43], power dividers [II.44, II.45], couplers [II.46], and other devices leveraging left-handed transmission lines have been proposed and demonstrated.

Building on the physical implementation of the symmetric condensed node in transmission line matrix modeling, the 2D network shown in Figure II-19 has been extended to a three-dimensional (3D) isotropic metamaterial transmission line topology. This advancement enables free-space excitation and further expands the potential applications of LHMs in practical scenarios [II.74].

II.10.6. Composite right/left-handed (CRLH) transmission line

In 2003, a more generalized model known as the composite right/left-handed (CRLH) transmission line was introduced [II.48]. This model provides a comprehensive framework for analyzing and optimizing practical left-handed transmission lines. As depicted in (Figure II-19), the CRLH transmission line consists of a series impedance per unit length Z'(Ω/m) and a shunt admittance per unit length $\mathrm{L}'\,R(\mathrm{H/m})$. The series impedance Z' is composed of an inductance per unit length $\mathrm{L}'\,\mathrm{R}(\mathrm{H/m})$. in series with a capacitance per unit length $\mathrm{CL}'(\mathrm{F}\cdot\mathrm{m})$, while the shunt admittance Y' includes a capacitance per unit length $\mathrm{CR}'(\mathrm{F/m})$, in parallel with an inductance per unit length in time $\mathrm{L}'\mathrm{L}(\mathrm{H}\cdot\mathrm{m})$.

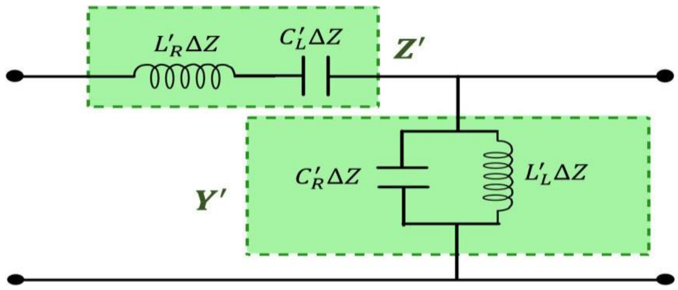

Figure II-19: A unit cell of the equivalent circuit for a composite right-hand / left-hand transmission line.

The propagation constant (γ) of the CRLH transmission line is given by:

$$\gamma = \alpha + j\beta = \sqrt{Z'Y'} \qquad (\mathrm{II}.40)$$

Here, (α) represents the attenuation constant, and (β) is the phase constant. The series impedance Z' and shunt admittance Y' are defined as:

$$\mathrm{Z'} = \mathrm{j}\left(\omega \mathrm{L'}_\mathrm{R} - \frac{1}{\omega \mathrm{C'}_\mathrm{L}}\right) \qquad (\mathrm{II}.41)$$

$$Y' = j\left(\omega C'_R - \frac{1}{\omega C'_L}\right) \tag{II.42}$$

For simplicity, the following resonant frequencies are introduced:

$$\omega'_R = \frac{1}{\sqrt{L'_R C'_R}} \quad \text{rad} \cdot \text{m/s} \tag{II.43}$$

$$\omega'_L = \frac{1}{\sqrt{L'_L C'_L}} \quad \text{rad} \cdot \text{m/s} \tag{II.44}$$

These frequencies characterize the transition points between right-handed and left-handed behavior in the CRLH transmission line. The CRLH model provides a versatile platform for designing metamaterial-based devices with tailored electromagnetic properties, enabling applications such as broadband antennas, filters, and phase shifters [II.49, II.34].

II.10.7. Series and shunt resonance frequencies in CRLH transmission lines

The behavior of a composite right/left-handed (CRLH) transmission line is governed by its series and shunt resonance frequencies, which are defined as follows:

$$\omega_{se} = \frac{1}{\sqrt{L'_R C'_L}} \quad \text{rad/s} \tag{II.45}$$

$$\omega_{sh} = \frac{1}{\sqrt{L'_L C'_R}} \quad \text{rad/s} \tag{II.46}$$

Here, ω_{se} and ω_{sh} represent the series and shunt resonance frequencies, respectively. These frequencies are critical in determining the transition between right-handed (RH) and left-handed (LH) behavior in the CRLH transmission line.

By integrating Equations (II.41) to (II.46) into Equation (II.40) and considering the sign change of the phase velocity for left-handed materials, the complex propagation constant γ can be expressed as:

$$\gamma = js(\omega)\sqrt{\left(\frac{\omega}{\omega'_R}\right)^2 + \left(\frac{\omega'_L}{\omega'_R}\right)^2 - \left(\frac{C'_R}{C'_L} + \frac{L'_R}{L'_L}\right)} \tag{II.47}$$

The function s(ω) determines the sign of the propagation constant and is defined as:

$$s(\omega) = \begin{cases} +1\ if\ \omega < \max\ (\omega_{se}, \omega_{sh})\ the\ righ\ hand\ band \\ -1\ if\ \omega < \min\ (\omega_{se}, \omega_{sh})\ the\ left\ hand\ band \end{cases} \tag{II.48}$$

This sign function ensures the correct phase velocity direction for both RH and LH modes.

II.10.8. Stopband and dispersion characteristics

Even in a lossless CRLH transmission line, when the angular frequency ω satisfies $\min(\omega_{se}, \omega_{sh}) < \max(\omega_{se}, \omega_{sh})$, the propagation constant γ becomes purely real $\gamma = \alpha$, indicating the presence of a stopband. Within this frequency range, wave propagation is prohibited, and the transmission line exhibits attenuation rather than propagation [II.34].

Figure II-20 illustrates the dispersion and attenuation characteristics of the CRLH transmission line [II.16]. The curves in the figure represent the phase constants for the right-hand β_{RH} and left-hand β_{LH} bands, as well as the pure phase constants for the right-hand β_{PRH} and left-hand β_{PLH} lines.

These parameters are defined as follows:

- **β_{RH}**:Phase constant of the right-hand band of the CRLH transmission line.
- **β_{LH}**: Phase constant of the left-hand band of the CRLH transmission line.
- **β_{PRH}**:Pure phase constant of the right-hand transmission line.
- **β_{PLH}**:Pure phase constant of the left-hand transmission line.

The dispersion diagram highlights the unique dual-band behavior of CRLH transmission lines, where the transition between RH and LH modes occurs at the resonance frequencies ω_{se} and ω_{sh} [II.18]. This behavior was experimentally verified in [II.52] through detailed S-parameter measurements.

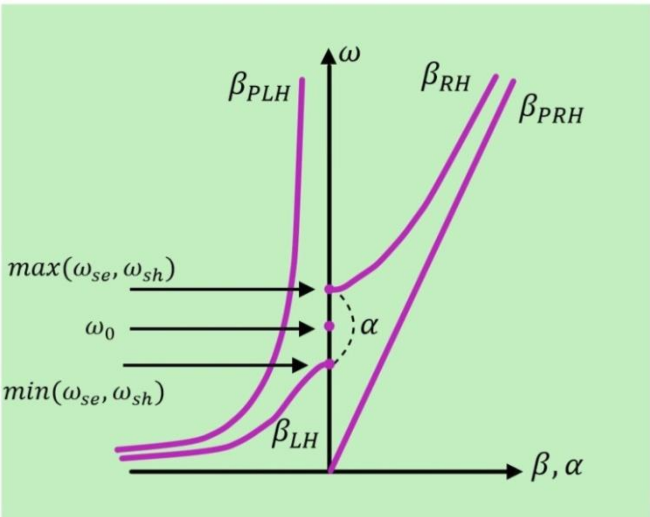

Figure II-20: The CRLH line dispersion / attenuation chart, when the energy propagation is along the z-axis.

II.10.9. Low-frequency and high-frequency behavior of CRLH transmission lines

At low frequencies, the impedance of the series inductance L'_R is significantly lower than hat of the series capacitance C'_L, and the admittance of the shunt capacitance C'_R is much less than that of the shunt inductance L'_L. Under these conditions, the series impedance Z'and shunt admittance Y' can be approximated as: $Z' \approx -\frac{1}{j\omega C'_L}$ *and* $Y' \approx -\frac{1}{j\omega L'_L}$,This implies that the right-handed (RH) contribution is negligible, and the transmission line behaves almost entirely as a left-handed (LH) line, exhibiting a hyperbolic dispersion pattern.

At high frequencies, the behavior of the CRLH transmission line shifts dramatically. Here, the series impedance Z' and shunt admittance Y' are dominated by the inductive and capacitive components, respectively: $Z' \approx j\omega L'_R$ *, and* $Y' \approx j\omega C'_R$.

In this regime, the CRLH transmission line behaves like a pure right-handed transmission line, displaying a linear dispersion diagram.

II.10.10. Balanced and unbalanced CRLH transmission lines

The performance of the CRLH transmission line at intermediate frequencies is determined by the combined contributions of the LH and RH components. A CRLH transmission line is said to be "balanced" when the series and shunt resonance frequencies are equal (ω_{se} = ω_{sh}) [II.50]. In this case, the zeros of Z' and Y' occur at the same frequency, resulting in the disappearance of the stopband. The characteristic impedance of the balanced CRLH transmission line becomes frequency-independent, allowing for impedance matching over an infinite bandwidth [II.53].

The characteristic impedance Z_C of the CRLH transmission line is given by:

$$Z_C = \frac{Z'}{\gamma} = \sqrt{\frac{Z'}{Y'}} = \sqrt{\frac{L'_L}{C'_L}} \cdot \sqrt{\frac{\left(\frac{\omega}{\omega_{se}}\right)^2 - 1}{\left(\frac{\omega}{\omega_{sh}}\right)^2 - 1}} = Z_R = Z_L \qquad (II.49)$$

When (ω_{se} = ω_{sh}), the characteristic impedances for the pure right-handed $Z_R$and left-handed Z_L transmission lines simplify to:

$$Z_R = \sqrt{\frac{Z'}{Y'}} = \sqrt{\frac{L'_R}{C'_R}} \qquad (II.50)$$

$$Z_L = \sqrt{\frac{Z'}{Y'}} = \sqrt{\frac{L'_L}{C'_L}} \qquad (II.51)$$

II.10.11. Applications of CRLH transmission lines

The unique phase response of CRLH transmission lines, including dual-band operation, enhanced bandwidth, nonlinear frequency dependency, and the existence of a critical frequency with zero phase velocity, has led to numerous innovative applications [II.54]. These include:

- Guided Wave Applications: CRLH transmission lines are used in phase shifters, filters, and couplers with improved performance and miniaturized designs [II.55].
- Radiated Wave Applications: Examples include frequency-swept leaky-wave antennas, electronically scanned antennas, and zero-order resonant antennas [II.43].

II.11. Progression in realizing metamaterials

The realization of metamaterials followed a three-step progression:

- Creating a Medium with Negative Permittivity: This involves designing structures that exhibit plasma-like behavior at specific frequencies [II.54].
- Realizing a Medium with Negative Permeability: This step requires the design of magnetic resonators that produce a negative magnetic response [II.55].
- Combining Both Media: By superimposing the two media, a doubly negative medium (with both negative permittivity and permeability) is achieved [II.43].

II.11.1. Metamaterials with negative permittivity

Negative permittivity is a property influenced by plasma physics and has been extensively studied in optics, infrared, and electromagnetics. Pendry and colleagues demonstrated that an array of parallel metal rods with radius r and periodicity α exhibits an electromagnetic response similar to that of a low-density plasma [II.56]. This behavior arises due to the interaction of electrons in the metallic structures at high frequencies.

When the excitation frequency matches the plasma frequency f_p, the applied field acts as a restoring force on the charges, leading to an oscillation phenomenon described by:

$$f_p{}^2 = \frac{nq^2}{4\pi^2 \varepsilon_0 m_{eff}} \qquad (II.52)$$

q is the elementary charge, n is the electron density, m_{eff} is the effective mass of the electrons, and ε_0 is the permittivity of free space. The plasma permittivity is only observable for frequencies below the plasma frequency.

The permittivity dispersion of the plasma is given by:

$$\varepsilon(\omega) = 1 - \frac{{\omega_p}^2}{\omega^2} \quad (II.53)$$

The plasma frequency is calculated as:

$$ {\omega_p}^2 = \frac{nq^2}{\varepsilon_0 \, m_{eff}} \quad (II.54)$$

With q indicating the charge of the electron and meff denoting the effective mass of the electron.

The approach consisted in making a network of heavier metal inclusions with a lower electron density. The chosen configuration consists of a network of metal rods of radius r ,with a pitch of the network a (Figure II-21).

For this setting, the plasma frequency is:

$$ {\omega_p}^2 = \frac{2\pi {C_0}^2}{a^2 \ln(a/r)} \quad (II.55)$$

Here, C_0 is the speed of light, a is the lattice constant, and r is the radius of the metal rods.

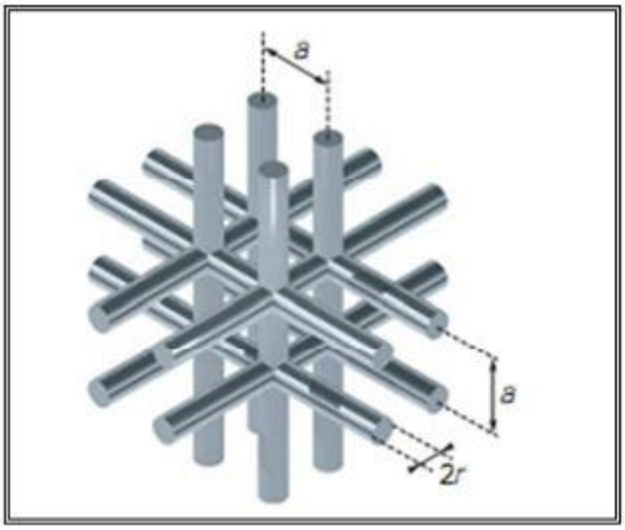

Figure II-21: Network of cylindrical metal wires with negative permittivity.

II.11.2. Metamaterials with negative permeability

In the microwave domain, materials such as ferromagnetic and antiferromagnetic composites MgF_2 and FeF_2 can exhibit negative permeability [II.51]. However, these materials have significant drawbacks, including high weight and substantial magnetic losses, which limit their practical applications. As a result, there has been considerable interest in developing nonmagnetic media that can achieve negative permeability without relying on traditional magnetic materials [II.15].

In 1999, J. Pendry proposed an innovative solution to this challenge by introducing a novel configuration based on a network of metallic structures shaped like Swiss rolls (Figure II-22) [II.51]. This structure creates an artificial magnetic resonance without the need for any magnetic material[II.51, II.16]. The Swiss roll consists of a series of conductive spirals, each wound around a cylindrical core of radius R.

The spirals are insulated from each other by a dielectric layer N, and the turns are spaced by a distance of d_C[II.51].

When a magnetic field is applied along the axis of the cylinder, it induces a current in the conductive spirals[II.16]. This current flows through the capacitive gaps between the turns, creating a resonant circuit. The resonance of this circuit generates a circulating current, which mimics the behavior of a magnetic dipole[II.51, II.16]. As a result, the Swiss roll structure exhibits an effective negative permeability at frequencies near its resonance[II.51].

The "Swiss roll" structure is considered a homogeneous medium because its largest dimension is much smaller than the wavelength of the excitation signal [II.16]. This property allows it to be treated as a bulk material with effective electromagnetic properties, making it suitable for use in metamaterial designs[II.51, II.16].

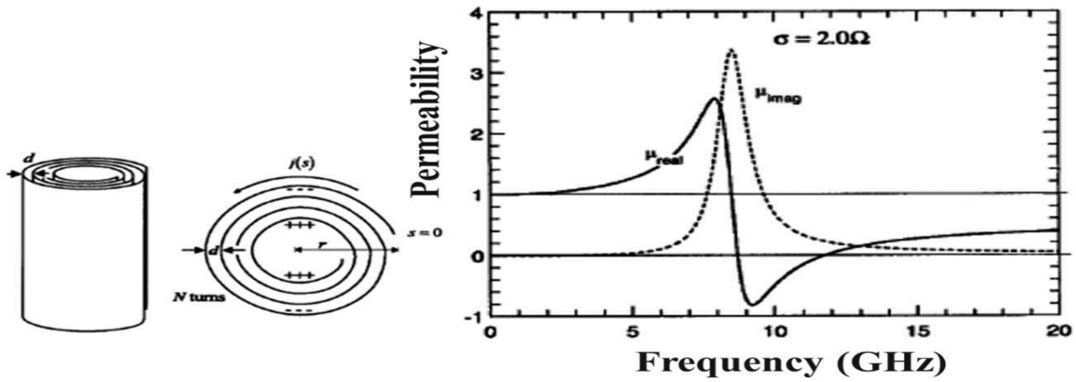

Figure II-22: The Swiss-Roll structure introduced by pendry, (a) front view and profile view (b) the calculated and measured Permeability for a Swiss 35-turn roller.

II.12. Effective permeability of swiss roll structures

Based on the pioneering work of Pendry et al. [II.51], the effective permeability μ_{eff} of a Swiss roll structure can be determined using the following relationship:

$$\mu_{eff} = 1 - \frac{F}{1+\frac{2\sigma_i}{\omega r \mu_0 (N-1)} - \frac{d C_0{}^2}{2\pi^2\omega^2 r^3 (N-1)}} \qquad (II.56)$$

Here, C_0 represents the speed of light in a vacuum, and ω is the angular frequency. The conductivity of the spiral is denoted by σ, while ε represents the permittivity of the insulating material between the conductive layers. The filling rate of the active material is given by F.
The effective permeability can also be expressed in a simplified form as:

$$\mu_{\text{eff}} = 1 - \frac{F\omega^2}{\omega^2 - {\omega_0}^2 + i\Gamma\omega} \tag{II.57}$$

Here, ω_0 is the resonance frequency of the structure, and γ accounts for losses in the system. The resonance frequency ω_0 is given by:

$$\omega_0 = \sqrt{\frac{dC_0{}^2}{2\pi^2 r^3 (N-1)}} \tag{II.58}$$

In this equation, r is the radius of the Swiss roll, and N is the number of turns in the spiral

II.12.1. Resonance damping in swiss roll structures

The resonance damping gamma in a Swiss roll structure is a critical parameter that accounts for energy losses within the system. It is given by the following relation:

$$\Gamma = \frac{2\sigma}{\omega r \mu_0 (N-1)} \tag{II.59}$$

Here, (σ) is the conductivity of the spiral, (ω) is the angular frequency, (ε_0) is the permittivity of free space, and (N) is the number of turns in the spiral. This damping factor influences the sharpness of the resonance and the overall performance of the structure [II.15].
Figure II-22 illustrates the measured and estimated effective permeability of the Swiss roll structure. The structure exhibits resonance only when the magnetic field is applied along the axis of the roll [II.15]. In other directions, the structure does not resonate, leading to anisotropic behavior [II.16]. Additionally, for transverse waves incident on a network of these structures, where the electric field is parallel to the cylinders, significant absorption is observed [II.18]. This anisotropic behavior can be undesirable in some applications, as it limits the versatility of the structure [II.19].

II.13. Metamaterials with negative permittivity ε and permeability μ

To achieve a material with a negative refractive index, both the relative permittivity ε and permeability (μ) must be negative simultaneously. While natural materials can exhibit negative permittivity (e.g., plasmas and metals in the infrared range) or negative permeability (e.g., ferromagnetic materials at gyromagnetic resonance), no natural material exhibits both properties at the same time [II.5].

The first practical example of a doubly negative composite medium was introduced by D. Smith in 2000 [II.16]. Inspired by the work of J. Pendry [II.57], Smith combined a network of metal rods (to achieve negative permittivity) with split-ring resonators (SRRs) (to achieve negative permeability) (Figure II-23). This composite structure demonstrated transmission in a frequency band where both (ε) and (μ)were negative, effectively realizing a left-handed medium [II.16].

This ground breaking experiment provided the first experimental validation of Veselago's theory [II.6], which predicted the propagation of electromagnetic waves through a medium with simultaneously negative permittivity and permeability. Smith's work marked the birth of the first practical metamaterial, opening the door to a wide range of applications in electromagnetics and optics [II.16].

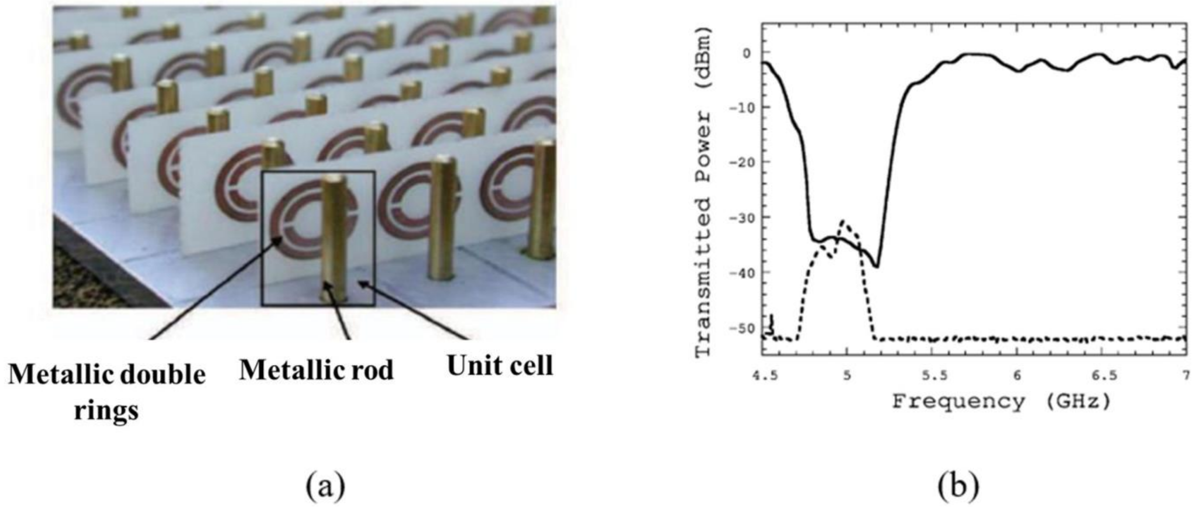

Figure II-23: Association of a network of rods with periodic SRRs. (b) the measured transmission power of the SRR array.

II.14. Evolution of resonator designs: Ω-shaped and S-shaped resonators

The development of resonator designs has played a crucial role in advancing metamaterial technology. The first Ω-shaped resonator was introduced by Saadoun [II.58], while the S-shaped resonator was originally proposed by Prosvirnin for bi-anisotropic structures (BIP) [II.59] (Figure II-24). These resonator designs are unique because they incorporate both a magnetic dipole in the ring and an electric dipole in the arms, enabling them to interact with both electric and magnetic fields simultaneously.

According to the authors of [II.60], the appeal of these resonator designs lies in their simplicity and versatility. They can be easily arranged in a periodic structure, allowing for polarization in two orthogonal directions. This property makes them ideal for creating two-dimensional (2D) metamaterials by stacking multiple layers of dielectric substrates. The ability to control both electric and magnetic responses in a single structure opens up new possibilities for designing compact and efficient metamaterials.

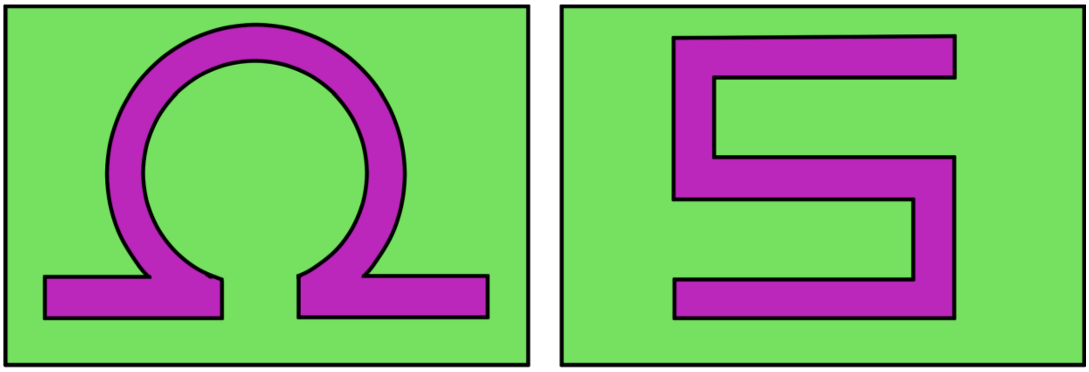

Figure II-24: Structure of resonators with negative refractive index. (a) "S" resonator. (b) "Ω" resonator.

II.15. Areas of application

II.15.1. Metamaterial superlens

Metamaterials have revolutionized the concept of lenses by enabling negative refraction, which allows electromagnetic waves to converge at a focal point rather than diverging outward. Unlike traditional convex lenses, which rely on curvature to focus light, a metamaterial lens can achieve focusing using a flat plate with a negative refractive index [II.5]. This groundbreaking idea was first proposed by J. Pendry in 2000, who suggested the realization of Veselago's "flat lens" a simple plate with a refractive index of (-1) [II.6]. Pendry's work demonstrated the practical realization of Veselago's theoretical optical medium, albeit limited to a specific frequency range [II.5, II.6].

In 2005, a significant breakthrough was achieved by the team of Xiang Zhang at the University of California, Los Angeles [II.61]. They developed a metamaterial superlens composed of a thin film of silver sandwiched between two semiconductor layers. This superlens demonstrated a resolution greater than one-fifth of the wavelength for frequencies in the visible spectrum [II.61]. Figure II-25 illustrates the imaging process using a convex lens (left-handed medium) and a right-handed (RH) plate. While conventional lenses heavily attenuate evanescent waves, preventing them from reaching the image plane, Pendry showed that a left-handed (LH) medium could reconstruct the amplitude of these evanescent waves, enabling subwavelength resolution [II.6].

II.15.2. Overcoming the diffraction limit

Superlenses leverage the unique properties of metamaterials to overcome the diffraction limit, a fundamental constraint in conventional optics. Ramakrishna and others have demonstrated that superlenses can achieve resolutions beyond those of ordinary microscopes [II.62]. Traditional optical materials transmit only the propagating components of light, while non-propagating components and evanescent waves are lost. These evanescent waves carry fine details of an object's structure, but they decay rapidly and do not contribute to the image formed by conventional lenses.

One approach to improving resolution is to increase the refractive index of the lens material. However, this is limited by the availability of high-index materials. Metamaterial superlenses address this limitation by significantly enhancing and recovering evanescent waves, which carry information at subwavelength scales [II.24]. This capability makes superlenses invaluable for applications requiring ultra-high resolution, such as nanoscale imaging and microscopy.

Despite these advancements, no superlens has yet been able to fully reconstruct all evanescent waves emitted by an object. The future challenge lies in designing superlenses capable of capturing and reconstructing all evanescent waves to achieve a perfect image [II.63].

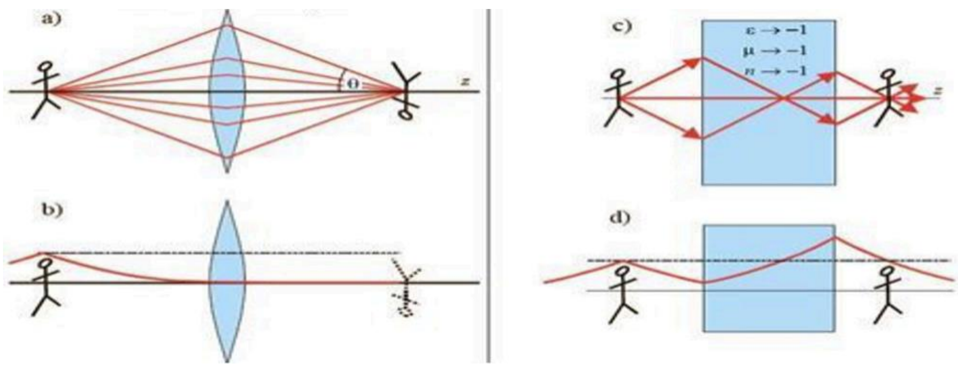

Figure II-25: Case of the classic lens: (a) to focus the waves, it must be convex. (b) the image.

Clarity is low, and the evanescent waves are diminishing. Case of the super lens: (c) A planar lens is used to focus the object. (d) The image resolution improves as the evanescent waves amplify in the lens.

Depending on Figure II-25 we can conclude that the focusing happens for the RH lens with incident propagated waves, and the information does not reach the source when focusing the lens for incident evanescent waves. On the other hand, for incident propagated waves on the LH plate, $\varepsilon = \mu = -1$, focusing occurs, and the information reaches the source due to a rise in energy within the plate [II.6].

II.15.3. Modeling microwave components

In recent years, metamaterials have been widely utilized to design and model advanced microwave components, offering significant advantages over traditional designs. These components include antennas [II.64], absorbers [II.65], sensors [II.66], filters [II.67], and more. One of the key benefits of metamaterial-based devices is their compact size. For example, metamaterial phase shifters are much smaller than their conventional counterparts. Additionally, left-handed (LH) transmission lines provide enhanced coupling at comparable spacing, making them ideal for couplers and other coupling-based devices.

Metamaterial components are characterized by their ability to exhibit simultaneously negative permittivity ε and permeability μ . The design of these structures often relies on split-ring resonators (SRRs) and complementary split-ring resonators (CSRRs). These resonators are typically integrated into various transmission lines, such as coplanar waveguides and microstrip lines, to achieve miniaturization and improved electromagnetic properties. In some cases, the reconfigurability of devices is also achieved using these structures.

The focus of this thesis is on microwave filters. Depending on the design, geometry, and parametric architecture of the metamaterial structures, various types of filters can be realized, including: Stopband filters, Bandpass filters, Ultra-wideband filters, and High-selectivity filters [II.68].

II.15.4. Cloaking metamaterials

One of the most fascinating applications of metamaterials is the concept of invisibility cloaking. This technology aims to render an object invisible by surrounding it with a network of metamaterials that deflect electromagnetic waves, reconstructing the wavefronts downstream of the object. This approach has significant potential, particularly in defense applications for stealth and camouflage.

The first experimental realization of an invisibility cloak was demonstrated by Schurig et al. [II.69], as shown in Figure II-26 (a). The results of this study clearly illustrate how electromagnetic radiation (denoted by black lines) is not reflected by the cloaked object (Figure II-25 (b)). Furthermore, the wave propagation in front of and behind the object remains nearly identical, effectively achieving invisibility.

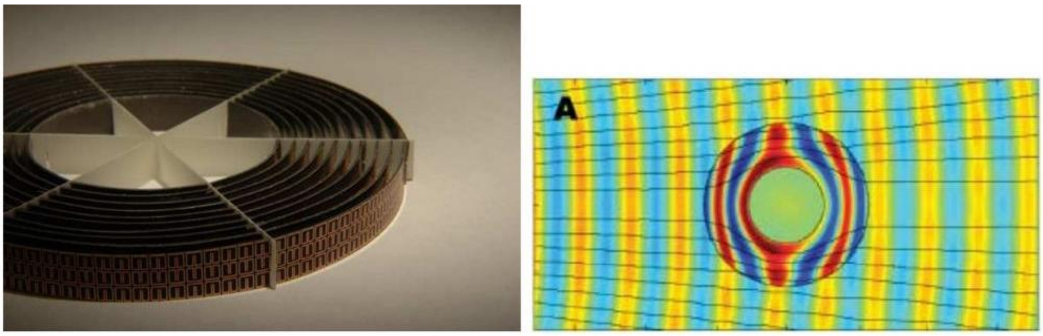

(a) **(b)**

Figure II-26: (a) A photo of the first metamaterial cloaking device. (b) the simulation result of the clocking device.

II.16. Conclusion

This chapter has provided an in-depth exploration of metamaterials, from their theoretical foundations to their groundbreaking applications. We began by defining metamaterials as artificially engineered structures capable of exhibiting electromagnetic properties not found in nature, particularly negative permittivity (ε)and permeability We then classified materials based on the signs of (ε)and (μ), and discussed the implications of these properties on Maxwell's equations, emphasizing the significance of a negative refractive index as a defining characteristic of metamaterials.

We delved into the fundamental concepts of transmission lines, highlighting the distinctions between right-handed (RH), left-handed (LH), and composite right/left-handed (CRLH) transmission lines. These structures serve as the building blocks for designing advanced microwave components, enabling miniaturization and enhanced performance in devices such as antennas, filters, and couplers.

Furthermore, we explored the realization of metamaterials with negative (ε) or (μ), detailing the design and functionality of structures like split-ring resonators (SRRs) and Swiss rolls. These innovations paved the way for the development of doubly negative materials, where both (ε)and (μ)are negative, leading to the creation of the first practical metamaterials.

The chapter also showcased several transformative applications of metamaterials, including:

- Superlenses: Overcoming the diffraction limit to achieve subwavelength resolution, revolutionizing fields such as nanoscale imaging and microscopy.
- Microwave components: Enhancing the performance of devices like antennas, filters, and phase shifters through compact and efficient designs.
- Invisibility cloaks: Demonstrating the potential of metamaterials to manipulate electromagnetic waves, rendering objects invisible and opening new possibilities in stealth technology.

Despite these remarkable advancements, challenges remain, such as minimizing losses, improving efficiency, and expanding the operational bandwidth of metamaterials. However, the rapid progress in this field promises continued innovation, with the potential to redefine the boundaries of science and technology.

In conclusion, metamaterials represent a paradigm shift in electromagnetics and optics, offering unprecedented control over electromagnetic waves and enabling applications that were once considered science fiction. As research and development in this field continue to advance, we can anticipate even more groundbreaking discoveries that will shape the future of technology.

References

[II.1] **J. C. Bose**, "On the rotation of plane of polarisation of electric waves by a twisted structure," Proc. Roy. Soc. London, 1898.

[II.2] **H. Lamb**, "On group-velocity and wave-propagation in dispersive media," Proc. London Math. Soc., 1904.

[II.3] **H. C. Pocklington**, "Growth of a wave-group when the group-velocity is negative," Nature, 1905.

[II.4] **K. F. Lindman**, "Über eine durch ein isotropes System von spiralförmigen Resonatoren erzeugte Rotationspolarisation der elektromagnetischen Wellen, » Ann. Phys., 1914.

[II.5] **V. G. Veselago**, "The electrodynamics of substances with simultaneously negative values of ε and μ," Sov. Phys. Usp. , vol. 10, no. 4, pp. 509-514, 1968.

[II.6] **J. B. Pendry**, "Negative refraction makes a perfect lens," Phys. Rev. Lett. , vol. 85, no. 18, pp. 3966-3969, 2000.

[II.7] **L. I. Mandelshtam,** Lectures on Optics, Relativity, and Quantum Mechanics, 1944.

[II.8] **W. E. Kock**, "Metallic delay lenses," Bell Syst. Tech. J, 1948.

[II.9] **G. D. Malyuzhinets**, "On the theory of artificial periodic structures," Sov. Phys. Tech. Phys, 1951.

[II.10] **D. V. Sivukhin**, "The energy of electromagnetic waves in dispersive media," Sov. Phys. Usp. , 1957.

[II.11] **V. E. Pafomov**, "On radiation in media with negative ε and μ," Sov. Phys. JETP, 1959.

[II.12] **J. Brown and W. Rotman**, "Wire networks for RF lenses," J. Appl. Phys., 1961.

[II.13] **S. Schelkunoff,** "Resonant magnetic rings and their applications," IEEE Trans. Antennas Propag. , 1962.

[II.14] **J. Pendry**, "Double resonant ring structures for metamaterials,"Phys. Rev. Lett. , vol. 83, no. 20, pp. 4184-4187, 1999.

[II.15] **R. A. Shelby, D. R. Smith, and S. Schultz**, "Experimental verification of a negative index of refraction," Science, vol. 292, no. 5514, pp. 77-79, 2001.

[II.16] **D. R. Smith et al.,** "Composite medium with simultaneously negative permeability and permittivity," Phys. Rev. Lett. , vol. 84, no. 18, pp. 4184-4187, 2000.

[II.17] **C. Caloz, T. Itoh, and G. V. Eleftheriades**, "Non-resonant metamaterials for loss minimization," IEEE Trans. Microw. Theory Tech., vol. 50, no. 12, pp. 2702-2712, 2002.

[II.18] **C. Caloz and T. Itoh**, Electromagnetic Metamaterials: Transmission Line Theory and Microwave Applications. Hoboken, NJ: Wiley-IEEE Press, 2005.

[II.19] **N. Engheta and R. W. Ziolkowski**, Metamaterials: Physics and Engineering Explorations. Hoboken, NJ: Wiley-IEEE Press, 2006.

[II.20] **P. Drude**, "Zur Elektronentheorie der Metalle," Ann. Phys. , vol. 306, no. 3, pp. 566-613, 1900.

[II.21] **J. D. Jackson**, Classical Electrodynamics, 3rd ed. New York: Wiley, 1999.

[II.22] **D. R. Smith, J. B. Pendry, and M. C. K. Wiltshire**, "Metamaterials and negative refractive index," Science , vol. 305, no. 5685, pp. 788-792, 2004.

[II.23] **A. Shivola**, Electromagnetic Mixing Formulas and Applications. London, U.K.: IET, 1999.

[II.24] **N. Fang et al.,** "Sub-diffraction-limited optical imaging with a silver superlens, Science, vol. 308, no. 5721, pp. 534-537, 2005.

[II.25] **F. Medina, F. Mesa, and R. Marqués**, "Near-field enhanced imaging by a magnetized ferrite slab," Appl. Phys. Lett. , vol. 86, no. 2, p. 023505, 2005.

[II.26] **C. A. Balanis**, Advanced Engineering Electromagnetics, 2nd ed. Hoboken, NJ: Wiley, 2012.

[II.27] **D. K. Cheng**, Field and Wave Electromagnetics, 2nd ed. Reading, MA: Addison-Wesley, 1989.

[II.28] **C. A. Balanis**, Antenna Theory: Analysis and Design, 4th ed. Hoboken, NJ: Wiley, 2016.

[II.29] **J. D. Kraus and D. A. Fleisch**, Electromagnetics with Applications, 5th ed. New York: McGraw-Hill, 1999.

[II.30] **D. M. Pozar**, Microwave Engineering, 4th ed. Hoboken, NJ: Wiley, 2012.

[II.31] **C. Caloz and T. Itoh**, "Reversed Cerenkov radiation in left-handed metamaterials," Phys. Rev. Lett. , vol. 92, no. 1, p. 013903, 2004.

[II.32] **J. Luo and P. Yu**, "Reversed Cerenkov radiation in a left-handed metamaterial," Phys. Rev. Lett. , vol. 110, no. 2, p. 023902, 2013.

[II.33] **C. Caloz and T. Itoh**, "Transmission line approach of left-handed (LH) structures and implementation of a microstrip LH line," IEEE Trans. Antennas Propag. , vol. 53, no. 1, pp. 144-153, 2005.

[II.34] **G. V. Eleftheriades**, "Enabling RF/microwave devices using negative-refractive-index transmission lines," IEEE Microw. Mag. , vol. 8, no. 4, pp. 34-50, 2007.

[II.35] **C. Caloz and T. Itoh**, "Application of the transmission line theory of left-handed (LH) materials to the realization of a microstrip LH transmission line," IEEE Trans. Antennas Propag. , vol. 52, no. 5, pp. 1159-1166, 2004.

[II.36] **G. V. Eleftheriades**, "A generalized negative-refractive-index transmission-line (NRI-TL) metamaterial for free-space and guided-wave applications," in IEEE MTT-S Int. Microw. Symp. Dig. , vol. 3, pp. 1399-1402, 2002.

[II.37] **C. Caloz and H. V. Nguyen**, "Novel broadband conventional- and dual-composite right/left-handed (C/D-CRLH) metamaterials: Properties, implementation and double-band coupler application," Appl. Phys. A, vol. 87, no. 2, pp. 309-316, 2007.

[II.38] **G. V. Eleftheriades, A. K. Iyer, and P. C. Kremer**, "Planar negative refractive index media using periodically L-C loaded transmission lines," IEEE Trans. Microw. Theory Tech., vol. 50, no. 12, pp. 2702-2712, 2002.

[II.39] **G. V. Eleftheriades and K. G. Balmain**, Negative-Refraction Metamaterials: Fundamental Principles and Applications. Hoboken, NJ: Wiley, 2005.

[II.40] **A. Lai et al.,** "Backward wave propagation in left-handed transmission lines," IEEE Trans. Microw. Theory Tech, vol. 52, no. 12, pp. 2779-2785, 2004.

[II.41] **A. Grbic and G. V. Eleftheriades**, "Experimental verification of backward-wave radiation from a negative refractive index metamaterial," J. Appl. Phys. , vol. 92, no. 10, pp. 5930-5935, 2002.

[II.42] **C. Caloz et al.,** "A novel composite right-/left-handed coupled-line directional coupler with arbitrary coupling level and broad bandwidth," IEEE Trans. Microw. Theory Tech., vol. 52, no. 3, pp. 980-992, 2004.

[II.43] **A. Lai et al**., "Infinite wavelength resonant antennas with monopolar radiation pattern based on periodic structures," IEEE Trans. Antennas Propag. , vol. 55, no. 3, pp. 868-876, 2007.

[II.44] **M. A. Antoniades and G. V. Eleftheriades**, "A broadband series power divider using zero-degree metamaterial phase-shifting lines," IEEE Microw. Wireless Compon. Lett. , vol. 15, no. 11, pp. 808-810, 2005.

[II.45] H. V. Nguyen and C. Caloz, "Generalized coupled-mode approach of metamaterial coupled-line couplers: Coupling theory, experimental verification, and applications," IEEE Trans. Microw. Theory Tech., vol. 54, no. 12, pp. 3990-4000, 2006.

[II.46] **J. Zhu et al**., "Dual-band metamaterial-inspired couplers for MIMO antenna systems," IEEE Antennas Wireless Propag. Lett. , vol. 12, pp. 1176-1179, 2013.

[II.47] **T. Ueda et al**., "Three-dimensional isotropic metamaterial transmission lines for free-space excitation," IEEE Trans. Microw. Theory Tech. , vol. 60, no. 12, pp. 3879-3888, 2012.

[II.48] **C. Caloz and T. Itoh**, "Novel microwave devices and structures based on the transmission line approach of meta-materials," in IEEE MTT-S Int. Microw. Symp. Dig. , vol. 1, pp. 195-198, 2003.

[II.49] **C. Caloz**, "Dual composite right/left-handed (D-CRLH) transmission line metamaterial, " IEEE Microw. Wireless Compon. Lett. , vol. 16, no. 11, pp. 585-587, 2006.

[II.50] **C. Caloz and T. Itoh**, "Balanced composite right/left-handed transmission line metamaterials," IEEE Trans. Microw. Theory Tech., vol. 54, no. 4, pp. 1512-1522, 2006.

[II.51] **J. B. Pendry et al.,** "Magnetism from conductors and enhanced nonlinear phenomena," IEEE Trans. Microw. Theory Tech., vol. 47, no. 11, pp. 2075-2084, 1999.

[II.52] **G. V. Eleftheriades et al**., "Experimental verification of backward-wave radiation from negative refractive index metamaterials," IEEE Trans. Antennas Propag. , vol. 53, no. 1, pp. 367-379, 2005.

[II.53] **G. V. Eleftheriades**, "A generalized negative-refractive-index transmission-line metamaterial for dual-band applications," IEEE Trans. Microw. Theory Tech. , vol. 55, no. 12, pp. 2546-2556, 2007.

[II.54] **C. Caloz**, "Dual-band CRLH transmission line metamaterials with multi-section stubs," IEEE Trans. Microw. Theory Tech., vol. 54, no. 1, pp. 29-41, 2006.

[II.55] **M. A. Antoniades and G. V. Eleftheriades**, "Compact linear metamaterial phase shifters for broadband applications," IEEE Antennas Wireless Propag. Lett. , vol. 2, pp. 103-106, 2003.

[II.56] **J. B. Pendry et al**., "Low frequency plasmons in thin-wire structures," J. Phys. Condens. Matter, vol. 10, no. 22, pp. 4785-4809, 1998.

[II.57] **J. B. Pendry et al.,** "Extremely low frequency plasmons in metallic mesostructures," Phys. Rev. Lett. , vol. 76, no. 25, pp. 4773-4776, 1996.

[II.58] **M. M. I. Saadoun and N. Engheta**, "A reciprocal phase shifter using novel pseudochiral or Ω medium," Microw. Opt. Technol. Lett. , vol. 5, no. 4, pp. 184-188, 1992.

[II.59] **S. L. Prosvirnin and S. A. Tretyakov**, "Polarization transformers based on bi-anisotropic particles," in Proc. Eur. Microw. Conf., 2001, pp. 1-4.

[II.60] **C. R. Simovski and S. A. Tretyakov**, "Model of isotropic resonant magnetism in the visible range based on core-shell clusters," Phys. Rev. B , vol. 79, no. 4, p. 045111, 2009.

[II.61] **S. A. Ramakrishna et al**., "Near-field focusing with a metamaterial superlens at visible wavelengths," Phys. Rev. Lett. , vol. 96, no. 6, p. 063901, 2006.

[II.62] **J. B. Pendry and D. R. Smith**, "The quest for the superlens," Sci. Amer. , vol. 295, no. 1, pp. 64-65, 2006.

[II.63] **A. Erentok and R. W. Ziolkowski,** "Metamaterial-inspired efficient electrically small antennas," IEEE Trans. Antennas Propag. , vol. 56, no. 3, pp. 691-707, 2008.

[II.64] **N. I. Landy et al.,** "Perfect metamaterial absorber,"Phys. Rev. Lett. , vol. 100, no. 20, p. 207402, 2008.

[II.65] **J. Naqui et al**., "Metamaterial sensors for microwave applications,"IEEE Sensors J, vol. 14, no. 6, pp. 1985-1993, 2014.

[II.66] **J. Bonache et al.,** “Novel compact metamaterial filters,”IEEE Microw. Wireless Compon. Lett. , vol. 16, no. 10, pp. 543-545, 2006.

[II.67] **J. Bonache et al**., "Novel compact left-handed coplanar waveguide components, IEEE Microw. Wireless Compon. Lett. , vol. 16, no. 10, pp. 543-545, 2006.

[II.68] **D. Schurig et al.,** "Metamaterial electromagnetic cloak at microwave frequencies," Science , vol. 314, no. 5801, pp. 977-980, 2006.

[II.69] **J. B. Pendry et al**., "Controlling electromagnetic fields," Science , vol. 312, no. 5781, pp. 1780-1782, 2006.

[II.70] **R. A. Shelby, D. R. Smith, and S. Schultz**, "Experimental verification of a negative index of refraction," Science, vol. 292, no. 5514, pp. 77-79, 2001.

CHAPITRE III:

Reconfigurable Metamaterial Stopband Filter

III.1. Introduction

Microwave filters are essential components in modern communication systems, responsible for selecting desired signals and rejecting interference. Stopband filters, in particular, are vital for eliminating specific unwanted frequencies. The relentless drive towards smaller, more integrated wireless devices necessitates significant miniaturization of these components. Metamaterials, especially designs based on Split-Ring Resonators (SRRs), offer a powerful solution, enabling compact filter designs by leveraging their sub-wavelength resonant properties.

A longside miniaturization, adaptability is increasingly crucial. Reconfigurable filters, capable of dynamically adjusting their frequency response, enhance system flexibility. While early reconfigurable designs used mechanical switches, the advent of semiconductor technology allows for efficient, high-speed electronic tuning using active components like PIN and varactor diodes integrated directly into the filter structure.

This chapter presents the design and analysis of a novel, miniaturized stopband filter featuring both frequency and mode reconfigurability. Central to this work is a newly developed metamaterial unit cell, derived from the SRR concept but engineered for enhanced electrical length and superior compactness compared to traditional designs. This optimized cell forms the basis of a stopband filter incorporating six strategically placed PIN diodes. These diodes act as switches, enabling dynamic control over the filter's resonant characteristics.

To present this research clearly, the chapter is structured into two primary sections. The first section delves into the design evolution of the novel metamaterial unit cell, explaining its operational principles and inherent advantages over conventional designs. It will also detail the subsequent steps taken to integrate these cells into the final multi-resonator stopband filter architecture. The second section focuses explicitly on the reconfigurability aspect. It introduces how the PIN diodes are incorporated as switching elements, explains the mechanism by which frequency and mode reconfigurability are achieved through different diode biasing states, and presents a detailed analysis of the filter's performance across its various operational configurations.

III.2. Resonant-type CRLH transmission lines

The first split-ring resonator (SRR) had a circular shape and was introduced by Pendry [III.1]. Since then, various other shapes have been proposed in subsequent studies. In that initial study, the metamaterial's properties were examined, particularly its negative effective permeability. The basic design of an SRR unit cell consists of two concentric rings, one nested inside the other, with each ring featuring a gap positioned opposite to the gap in the other ring. The gap between the rings, the ring widths, and the sizes of the openings are all precisely calculated, as they significantly influence the SRR's performance. Moreover, due to the positioning of the splits in the rings, the resulting displacement currents flow from the inner ring to the outer one. Consequently, the SRR can be modeled as an equivalent LC circuit [III.2].

III.2.1. The extraction techniques for effective parameters

The crucial component of the rest of our study is to demonstrate that these metamaterial devices have a negative refractive index around or at the resonant frequency. The permittivity and permeability may be calculated using a variety of methods based on the reflection and transmission coefficients. Each conversion technique has its own set of benefits and drawbacks. The used method is determined by a number of criteria, such as the simulated or measured S parameters (S_{11}, S_{21}), sample length, required dielectric characteristics, conversion rate, and converted result accuracy. The [S] parameters are generated by a wave normally incident on a metamaterial slab, assuming that the slab boundaries are well defined and that the Fresnel formulas for reflection and transmission hold at the air-metamaterial interface, with S_{11} representing the reflection coefficient and S_{21} representing the transmission coefficient:

$$S_{11} = M_{11}e^{-i\varphi_{11}} \tag{III.1}$$

$$S_{21} = M_{21}e^{-i\varphi_{21}} \tag{III.2}$$

The moduli and phases of reflection and transmission are represented by M_{11}, M_{21}, φ_{11}, and φ_{21}, respectively. The Nicolson-Ross-Weir (NRW) technique calculates the permittivity and the permeability directly from S parameters [III.3,III.4]. The four coefficients (S_{11}, S_{21}, S_{12}, S_{22}) or a pair (S_{11}, S_{21}) of the coefficients of the material under test must be simulated or measured in order to extract the reflection coefficient and transmission coefficient. We will go through the NRW method's premise as well as its limitations in the following sections.

III.2.1.1. Extraction by the Nicolson-Ross-Weir method

The Nicolson-Ross-Weir (NRW) extraction method is based on inverting the Fresnel equations that describe the normal-incidence reflection and transmission coefficients of a composite medium, using its wave impedance and refractive index. From these quantities, the average permittivity and permeability of the material can be calculated. Also known as the distributed impedance method, the NRW technique is used to characterize both natural materials and composite (granular) materials with densely packed grain structures, through both numerical simulations and experimental measurements [III.3, III.4]. Smith et al. were the first to apply this method in the context of metamaterials [III.5]. One limitation of the NRW method is that it requires the existence of only a single propagating mode at the frequency of interest. Additionally, accurate extraction of effective parameters is only feasible when the incident wavelength is significantly larger than the size and spacing of the individual elements within the composite medium.

The NRW method is based on a simple interference calculation that determines the transmission and reflection of a layer of material as a function of its effective index, effective impedance, and thickness. Smith proved that by inverting the Fresnel equations we can obtain the values of n_{eff} and z_{eff} as a function of the simulated layer thickness d at the coefficients of transmission $t' = s_{21}$ and reflection $r = s_{11}$ [III.5]:

$$Re(n_{eff}) = \pm Re\left(\frac{\arccos\left(\frac{1}{2t'}\left[1-\left(r^2-t'^2\right)\right]\right)}{kd}\right) + \frac{2\pi m}{kd} \qquad (III.3)$$

$$Im(n_{eff}) = \pm Im\left(\frac{arccos\left(\frac{1}{2t'}\left[1-\left(r^2-t'^2\right)\right]\right)}{kd}\right) \qquad (III.4)$$

$$z_{eff} = \pm\sqrt{\frac{(1+r)^2-t'^2}{(1-r)^2-t'^2}} \qquad (III.5)$$

Where m is an integer, the thickness of the material is represented by d, and the vacuum wave vector of the incident plane wave is represented by $k = {}^{\omega}/_{c}$.

The effective parameters ε_{eff} and μ_{eff} can be calculated from the effective index and impedance using the following equation:

$$\varepsilon_{eff} = \frac{n_{eff}}{z_{eff}} \qquad \text{(III.6)}$$

$$\mu_{eff} = n_{eff} \cdot z_{eff} \qquad \text{(III.7)}$$

III.2.2. Magnetically active resonator

III.2.2.1. Circular SRR

The circular split ring resonator (SRR) introduced by Pendry, was designed for X-band operations [8.2 GHz; 12.4 GHz] [III.1]. As presented in Figure III-1, the radius of the outer ring is r=3 mm, the width of the rings is c=0.33 mm, the opening width of the rings is g=0.33mm, and the spacing between the two rings is d=0, 33 mm. The simulation was conducted using ROGERS RO4003C substrate, which has a relative permittivity of 3.38, tangential losses on the order of 0.0027, and a thickness of h=0.81 mm.

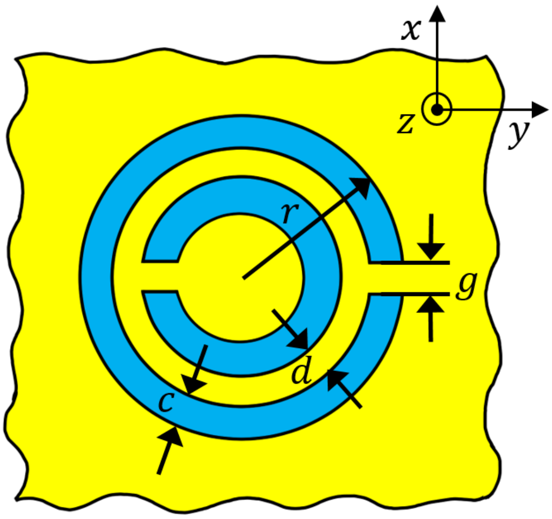

Figure III-1: A circular split-ring resonator [III.5].

The inductance L and capacitance C can be used to describe a subwavelength Split-Ring resonator (Figure III-2) [III.6].

The resonant frequency is:

$$f_r = \frac{1}{2\pi\sqrt{LC}} \qquad \text{(III.8)}$$

$$L = \mu_0 r_m \left(\ln\left(\frac{8\, r_m}{h+c}\right) - 0.5\right) \qquad \text{(III.9)}$$

Where μ_0 denotes vacuum permeability, and r_m the ring's mean radius.

$$r_m = r + \frac{w}{2} \tag{III.10}$$

Where r is the inner radius of the ring.

The surface capacity (C_{surf}) and the gap capacity (C_{gap}) are the two capacities used in this study. Where the gap capacitance is the result of the charges in the gap, which can be used as a parallel plate capacitance. Meanwhile, the surface capacity is provided by loads on the surface of the ring [III.6].

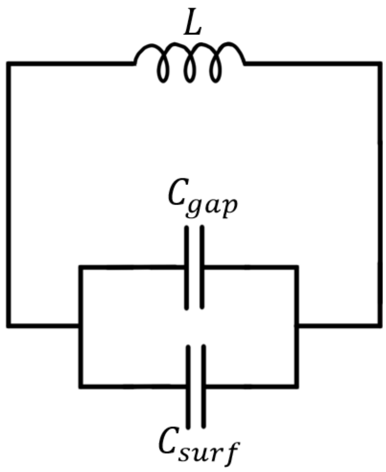

Figure III-2: The circular SRR equivalent circuit.

$$C_{gap} = \varepsilon_0 \left[\frac{wh}{g} + \frac{2\pi h}{\ln\left(\frac{2.4h}{w}\right)} \right] \tag{III.11}$$

$$C_{surf} = \frac{2\varepsilon_0 h}{\pi} \, ln\left(\frac{4R}{g}\right) \tag{III.12}$$

Assuming that the gap and surface capacitances are parallel, the total capacitance is:

$$C = C_{gap} + C_{surf} \tag{III.13}$$

The conducted Simulations are for obtaining the S parameters of a network of SRR systems using the HFSS simulator. The parameters S_{11} and S_{21} will be used for the extraction of the effective parameter μ_{eff}. Moreover, before starting the simulation, it is necessary to fix the boundary conditions on the ends of this structure, to this end, the electric and magnetic walls are applied along the y-axis and x-axis, respectively, and the direction of the wave propagates along the z-axis. The magnetic field must be parallel to the axis of the rings to ensure magnetic activity in the SRR; thus, periodicity conditions are applied to the presented unit cell. On the other hand, Rogers 4003C dielectric substrate is an important raw material in the production of multi-layer electronic board, this kind of product is mainly used for double-sided PCB. For this design, only one layer of the structure is considered for electromagnetic wave propagation.

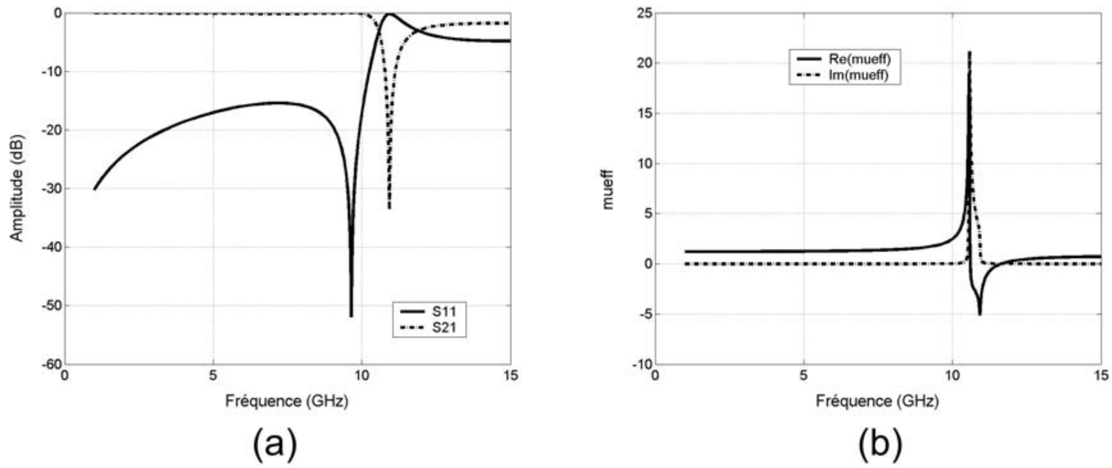

Figure III-3: The E-field along the z-axis: (a) the parameters S of the circular SRR structure and (b) Real and imaginary parts of the effective permeability.

Where the electric field along the z-axis and the propagation wave along the y axis, the S parameters simulation results are shown in Figure III-3 (a) where the resonance frequency is at 10.925 GHz, which reaches a level of -34 dB. Around the resonant frequency, the real part of the permeability is negative in a narrow band, and takes values varying from 0 to -5, while outside this band, Re (μ_{eff}) is positive (Figure III-3 (b)).

For the case of the polarization of the electric field along the z-axis, the E-field respects the symmetry of the structure, and it does not excite the openings of the rings of SRR, therefore, exists only the magnetic resonance of the structure. We note that in the case of double resonance (electric and magnetic), the resonance frequency is slightly higher than when only magnetic resonance exists.

III.2.3. Electrically active resonator (metal line)

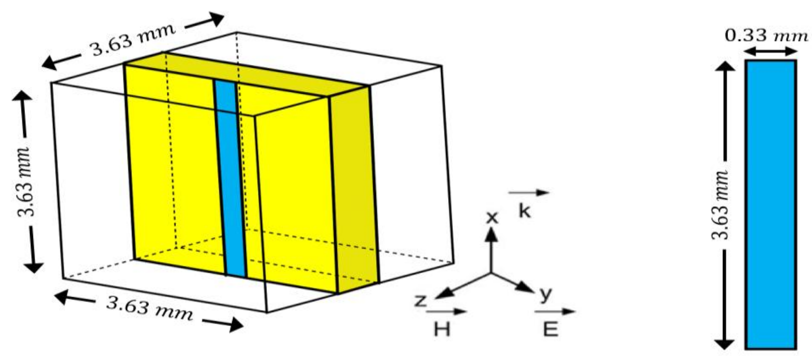

Figure III-4: The structure of metal line unit cell.

The electromagnetic response of a metal line cell unit is comparable to that of a low-density plasma, resulting in a negative effective permittivity [III.7]. The boundaries are subjected to the following conditions: electric walls are applied to the two faces perpendicular to the z-axis, while magnetic walls are applied perpendicular to the x-axis on both sides (Figure III-4).

The line is 3.63 mm long, which corresponds to the height of the radiation box as well as the periodicity, and 0.33 mm width, which corresponds to the gap or opening of the magnetic activity resonator rings.

The transmission and reflection coefficients of the metallic line are displayed Figure III-5. The plasma frequency of the metallic line investigated is 20.9 GHz at -3 dB for high-pass type transmission. This figure also shows that the analyzed structure exhibits complete rejection below the plasma frequency.

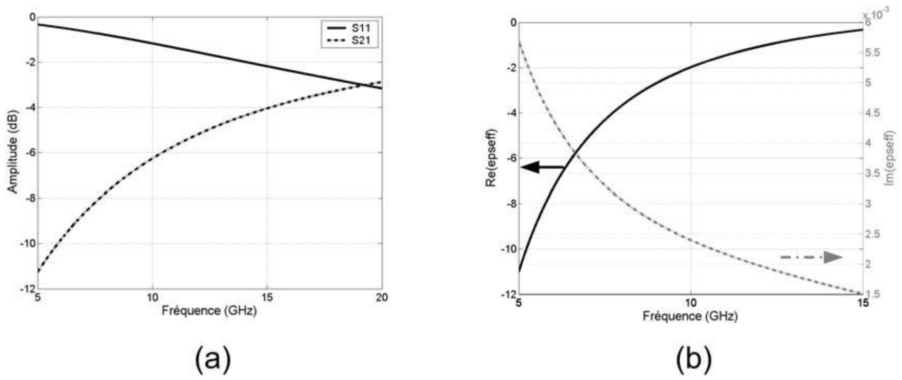

Figure III-5: The simulated results of the metal line: (a) Reflection and transmission in dB. (b) Real and imaginary parts of the effective permittivity [III.7].

III.3. Frequency and mode reconfigurable microstrip stopband filter using PIN diodes loaded with new metamaterial cells

In this section, a new SRR design is proposed. This SRR is used to structure a reconfigurable stopband filter. This SBF is designed and optimized to resonant with three important wireless communication bands. Furthermore, the reconfigurability is achieved by loading six PIN diodes onto the filter structure. This method allowed the achievement of SBF with seven different cases, in terms of the resonant frequency and the number of rejected bands (triple, dual, or single-mode stopband filter).

Besides the above, the presented SBF model has a small size compared to similar papers that have been reported, and this is thanks to the new SRR. Moreover, the PIN diodes are loaded in such a way that the design is simple. The measured results showed minimum losses and good electromagnetic properties.

III.3.1. The new split-ring resonator

The proposed planar metamaterial unit cell, shown in Figure III-6 (a), is implemented on a dielectric substrate (shown in blue) and incorporates a conductive pattern (depicted in orange). The design features two primary concentric resonating elements that exhibit vertical symmetry. The outer element is a large, nearly circular ring serving as the primary split-ring resonator (SRR), characterized by a narrow vertical split positioned at the apex (12 o'clock).

Nested within this ring is a smaller, elliptic inner structure that also includes a vertical split at its apex. This inner gap is precisely aligned with that of the outer ring and is electrically connected via two conductive rectangular stubs—one on each side of the splits—thereby enabling strong capacitive coupling between the two resonators. Notably, the lower segment of the inner structure (near the 6 o'clock position) deviates significantly from a continuous arc. Instead, it comprises two parallel vertical rectangular stubs extending upward from the ends of the semi-elliptic inner segments. These stubs are separated by a narrow, vertically oriented gap centered along the vertical axis of symmetry, introducing an additional capacitive gap within the inner resonator.

This innovative unit cell design offers several advantages:

- ✓ **Enhanced miniaturization**: The modification of the inner resonator increases the effective electrical path within a compact footprint. By directing current along the semi-elliptic contours and the vertical stubs, the structure achieves a lower fundamental resonant frequency compared to conventional double SRRs with comparable overall dimensions (Figure III-6 (b)). This results in effective size reduction, supporting the development of miniaturized metamaterial-based devices.
- ✓ **Improved tuning flexibility**: The resonant frequency and electromagnetic response of the unit cell are highly sensitive to the geometry of the modified inner structure. Adjustments to the length or width of the vertical stubs, or to the elliptic curvature of the inner ring, provide independent tuning parameters. This flexibility facilitates the design of devices tailored to specific operational frequencies or bandwidths.
- ✓ **Simplified fabrication**: Replacing the traditionally curved lower section of the inner ring with straight vertical stubs can simplify certain fabrication steps. This design may reduce

manufacturing complexity and enhance tolerance or yield, especially when compared to structures involving intricate curved features.

- ✓ **Enhanced coupling control**: The central gap between the vertical stubs introduces an additional capacitive element that impacts the intra-resonator coupling within the inner structure. This alters the overall coupling dynamics and electromagnetic field distribution relative to standard double SRRs. The gap also becomes a focal point for strong electric field concentrations at resonance, which can be exploited for engineering specific filter responses.

In this study, three target frequencies—2.0 GHz, 2.5 GHz, and 3.6 GHz—are investigated. The corresponding unit cell dimensions required to achieve resonance at each of these frequencies are detailed in Table III-1.

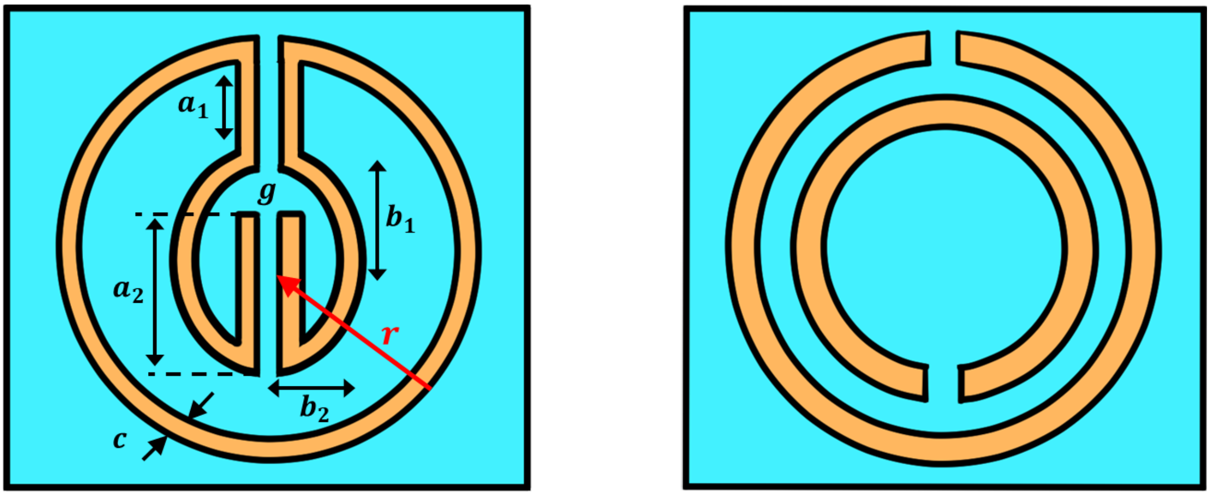

(a) (b)

Figure III-6: (a): The layout of the proposed split-ring resonator. (b) The layout of a traditional circular split-ring resonator.

Table III-1 The different dimensions of the SRR for each case according to the target frequencies.

Variables	Dimensions (mm)		
	2.0 GHz SRR	**2.5 GHz SRR**	**3.6 GHz SRR**
a_1	1.9	1.3	0.6
a_2	3.1	2	1.9
b_1	2.7	2.5	1.8
b_2	2	2	1.5
c	0.5	0.5	0.5
g	0.5	0.5	0.5
r	10	8.4	6.2

III.3.2. The effective refractive index

To investigate the metamaterial characteristics of the proposed filter, the real part of the effective refractive index n is extracted from the simulated S-parameters obtained using CST Microwave Studio. This analysis is performed for the three targeted resonant frequencies: 2.0 GHz, 2.5 GHz, and 3.6 GHz. For each frequency, the SRR pair in the single-mode stopband filter (illustrated in Figure III-7) is modified accordingly, using the dimensions provided in Table III-1.

The process, summarized below, was described in detail in Chapter Two of this dissertation:

1. Export the simulation results for the S11 and S21 coefficients from CST.
2. Import the exported data into MATLAB as column vectors.
3. Apply the Nicolson-Ross-Weir (NRW) retrieval method in MATLAB using the imported S-parameters.
4. Analyze the real part of the resulting effective refractive index.

The plotted results, shown in Figure III-7, clearly demonstrate that the real part of the refractive index is negative at each of the targeted frequencies. This negative behavior is a hallmark of metamaterial properties and confirms the metamaterial nature of the proposed SRR-based filter at the specified resonant points.

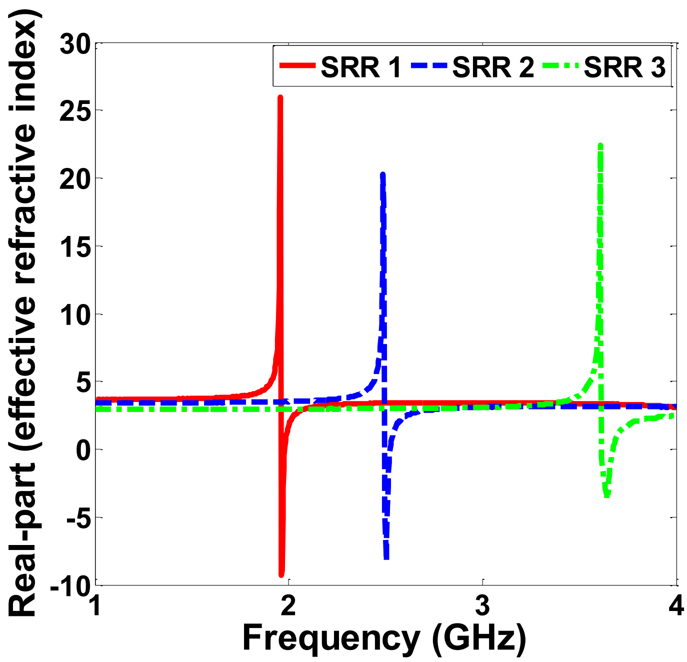

Figure III-7: Real-part of the effective refractive index n_{eff} of the different SRRs.

III.3.3. The triple-mode metamaterial stopband filter

III.3.3.1. Step one: stopband filter loaded with one SRR pair

The developed unit cell design is utilized to propose a stopband filter configuration. The design process involves three key steps to arrive at the final filter structure. The first step is the implementation of an initial stopband filter, illustrated in Figure III-8. This configuration consists of a 50 Ω microstrip transmission line, measuring L = 18 mm in length and S = 1.75 mm in width. Symmetrically placed on either side of this line are two identical split-ring resonators (SRRs) based on the newly proposed design. These resonators, tuned to operate at 2.0 GHz, are designated as SRR1 for future reference.

The spacing between each SRR and the microstrip line plays a crucial role in determining the filter's performance. Following a series of simulations and adjustments, the optimal distance was selected to ensure effective electromagnetic coupling between the line and the resonators. The filter is fabricated on a Rogers 6002 substrate, characterized by a relative permittivity of $\varepsilon_r = 2.94$, a loss tangent of $\tan\delta = 0.0012$, and a thickness of h = 0.76 mm. This substrate will be used consistently throughout the remainder of this chapter.

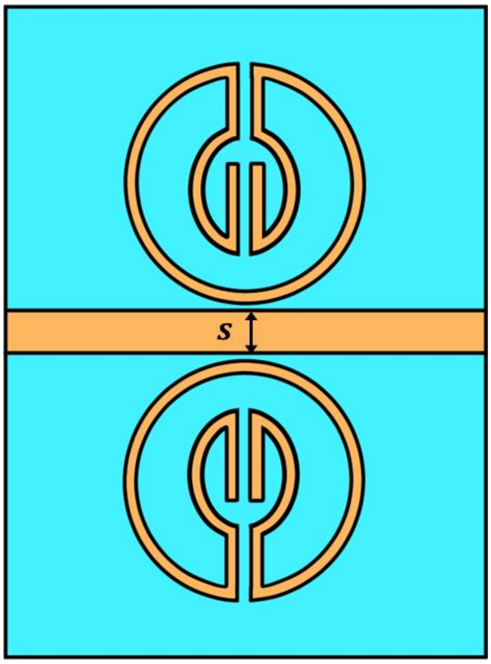

Figure III-8: Top view of the SBF loaded with one SRR pair (step one).

The S-parameter results for this stopband filter are presented in Figure III-9, highlighting the transmission coefficient S_{21} (in blue) and the reflection coefficient S_{11} (in red) across the frequency range of 1 to 4 GHz. A sharp attenuation is observed in S_{21} at the center frequency of 2.0 GHz, with a rejection level of approximately –16 dB, indicating strong suppression within the stopband. Outside of this range, S_{21} remains relatively flat, reflecting minimal disruption in the passband. Correspondingly, S_{11} shows a sharp peak at 2.0 GHz, where S_{21} dips, confirming that the majority of the incident signal is reflected—an expected characteristic of a well-designed single-mode stopband filter.

This filtering behavior validates the design's ability to effectively block targeted frequencies while allowing others to pass, aligning well with the intended performance goals for applications requiring selective frequency rejection. Furthermore, considering the compact size of the filter and the relatively low target frequency, the results underscore the advantages of the newly developed SRR structure over traditional double-ring SRR unit cells, which typically require larger dimensions to achieve comparable performance.

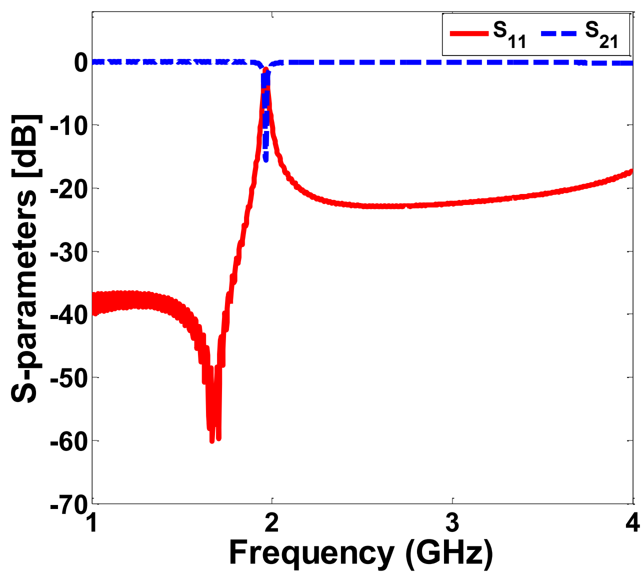

Figure III-9: Simulation results of the transmission and reflection coefficients of step one (one SRR pair).

III.3.3.2. Step two: stopband filter loaded with two SRR pairs

The upper layer of the second design step is illustrated in Figure III-10. In this configuration, the microstrip line, substrate, and ground plane are extended to a total length of L = 20 mm to accommodate an additional pair of split-ring resonators (SRRs). This new pair, designated as SRR2, is designed using unit cell dimensions tuned to resonate at 2.5 GHz.

The spatial separation between the SRR1 pair (resonating at 2.0 GHz) and the newly introduced SRR2 pair is a critical design parameter. It is carefully adjusted to ensure minimal to negligible coupling between the two resonator pairs. This isolation is essential to maintain distinct and independent resonant responses from each SRR set, allowing each frequency to be influenced solely by its corresponding resonator pair. At the same time, the design must remain compact, so the spacing is optimized to prevent interaction while minimizing the overall footprint.

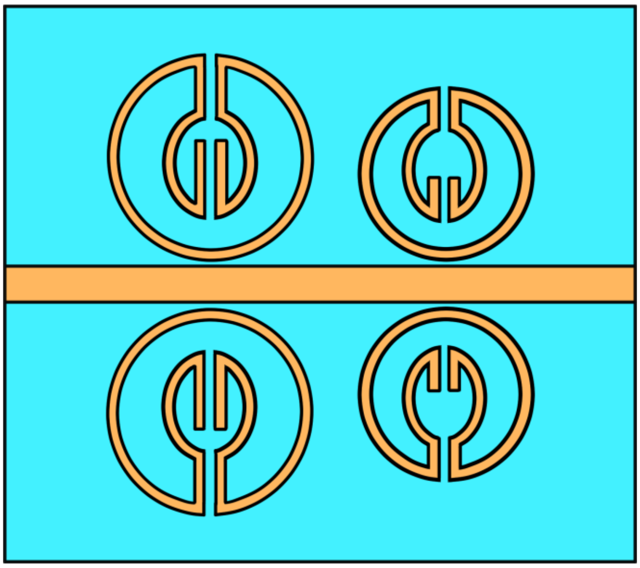

Figure III-10: Top view of the SBF loaded with two SRR pairs (step two).

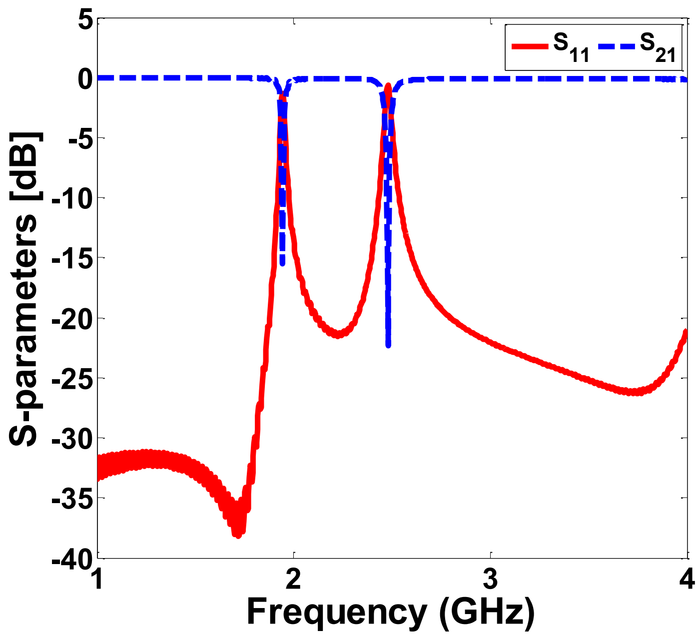

Figure III-11: Simulation results of the transmission and reflection coefficients of step two (two SRR pair).

The S-parameter results for the second-step structure, as shown in Figure III-11, reveal a transition from a single-mode to a dual-mode stopband filter. The transmission coefficient S_{21} exhibits two distinct attenuation dips, indicating effective rejection at two frequencies: approximately 2.0 GHz with a rejection level of –15 dB, and 2.5 GHz with a deeper rejection of about –22 dB. These results confirm the successful implementation of dual-band stopband behavior. As in the previous step, strong stopband characteristics are observed, demonstrating the effectiveness of the multi-resonator configuration in achieving multi-frequency suppression within a compact design.

III.3.3.3. Step three: stopband filter loaded with three SRR pairs

In the final design step, a third pair of split-ring resonators (SRRs), designated as SRR3, is added to the structure. This newly introduced pair is designed with dimensions tuned to resonate at 3.6 GHz, and it follows the same design methodology as in the previous steps (Figure III-12). It is important to note that with each successive step, the previously placed SRR pairs undergo minimal dimensional adjustments to maintain resonance at their designated frequencies. This is necessary because the microstrip line, substrate, and ground plane are progressively extended, and the increased length of the microstrip line can influence the resonant behavior.

The final filter structure measures 37 mm × 27 mm × 0.76 mm. The complete three-stage design has been optimized and simulated using CST Microwave Studio to ensure precise performance.

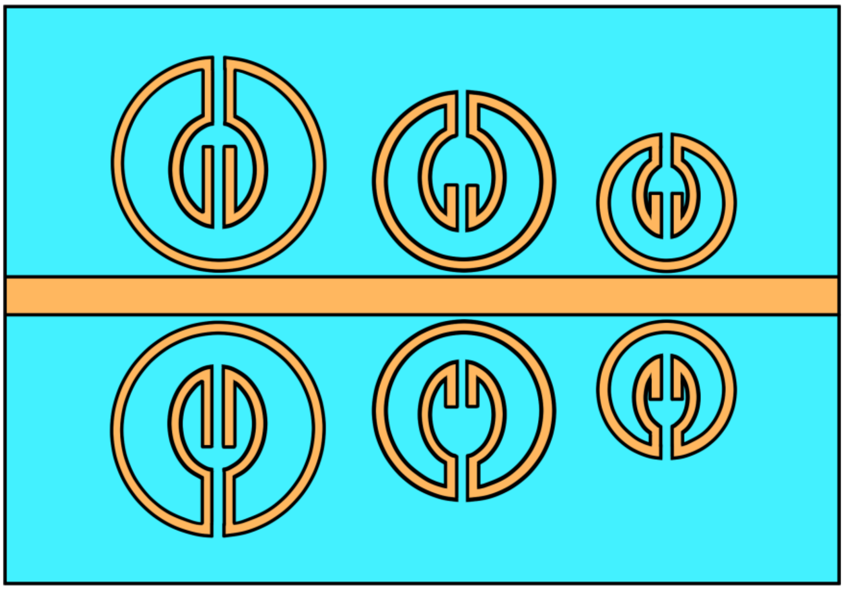

Figure III-12: Top view of the SBF loaded with three SRR pairs (step three).

The S-parameter results for the final configuration are presented in Figure III-13. As expected, the addition of SRR3 results in a triple-mode stopband filter. The transmission coefficient S_{21} reveals three well-defined attenuation notches at 2.0 GHz, 2.5 GHz, and 3.6 GHz, with corresponding rejection levels of approximately –17 dB, –23 dB, and –26 dB, respectively.

This clearly demonstrates the filter's ability to effectively suppress signals at multiple frequencies while preserving a relatively flat response outside the stopband.

Correspondingly, the reflection coefficient S_{11} exhibits sharp peaks at the same frequencies where S_{21} dips, indicating strong reflection of incident signals—an expected behavior for an efficient stopband filter. This triple-mode operation significantly enhances the filter's selectivity, offering sharp rejection across multiple frequency bands. Such a response is particularly beneficial for applications that require precise and simultaneous suppression of multiple frequencies.

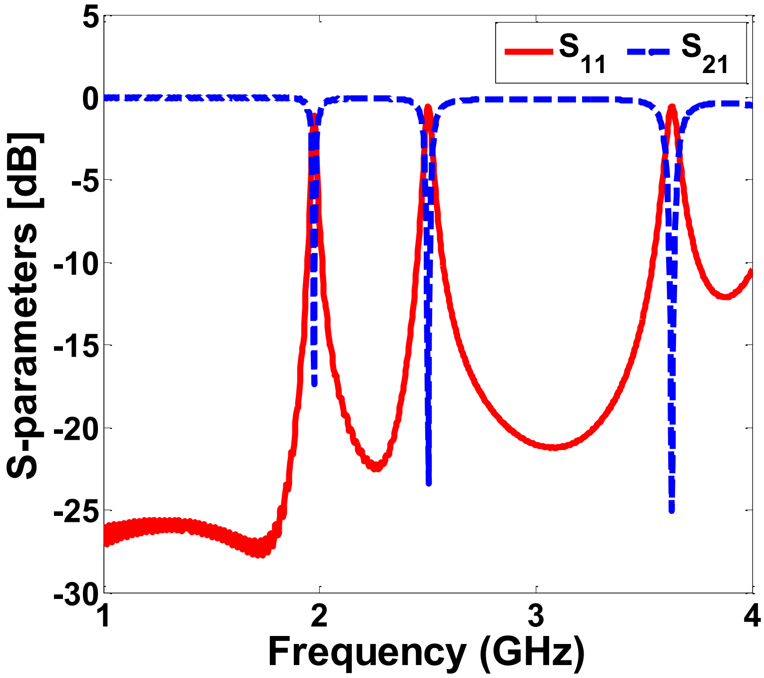

Figure III-13: Simulation results of the transmission and reflection coefficients of step three (three SRR pair).

III.3.3.3.1. The E-field distribution

Figure III-14 illustrates the electric field (E-field) distribution simulated using CST, highlighting how the field is confined to and concentrated around a specific pair of SRRs, depending on the corresponding resonant frequency. This observation confirms the successful minimization of coupling effects between the different SRR pairs. Each pair resonates independently, with negligible influence on the frequencies rejected by the other pairs.

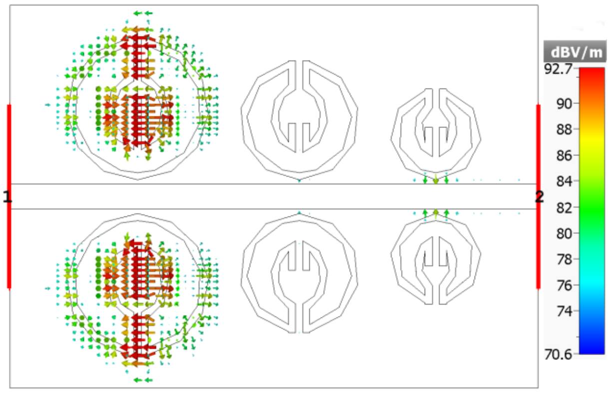

(a)

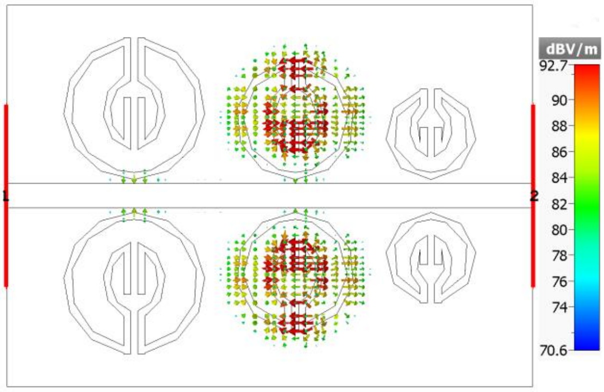

(b)

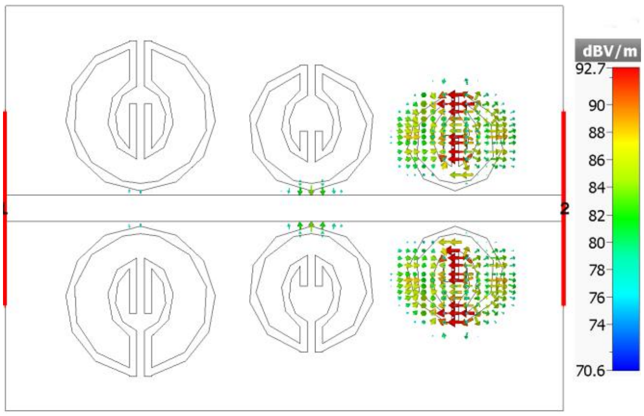

(c)

Figure III-14: The E-field distribution of the triple-mode stopband filter at: (a) 2.0 GHz; (b) 2.5 GHz; (c) 3.6 GHz.

This result was achieved through the careful selection of optimal spacing between the three SRR pairs, ensuring effective isolation. Such behavior is particularly important for the next phase of the study — reconfigurability — where the goal is for each SRR pair to operate independently at its designated frequency, without interference or undesired coupling from adjacent resonators. This property lays a solid foundation for flexible, frequency-selective filter design.

III.4. Frequency and mode reconfigurable metamaterial stopband filter using PIN diode

This section introduces the design of an electronically reconfigurable stopband filter (SBF). The reconfigurability is realized by integrating PIN diodes into the triple-mode stopband filter described previously. As shown in Figure III-15, one PIN diode is inserted across the split of the outer ring of each SRR, allowing control over the filter's characteristics. This configuration enables dynamic tuning of both the resonant frequency and the operational mode (single-mode, dual-mode, or triple-mode), depending on the state of the diodes.

PIN diodes function as voltage-controlled switches in microwave and radiofrequency systems. Their behavior is dictated by the applied bias voltage [III.8]:

- In the forward-biased (ON) state, the diode exhibits low impedance, effectively shorting the SRR gap and suppressing resonance.
- In the reverse-biased (OFF) state, the diode presents high impedance and low capacitance, allowing the SRR to behave as a resonant structure.

To achieve full reconfigurability, six BAR50-02 PIN diodes from Infineon are used—one for each SRR. The diodes are placed at the outer ring splits, a location proven optimal for switching and for ease of physical placement. Due to the metamaterial nature of the SRRs, when exposed to an external magnetic field, each SRR induces a circulating current, resulting in resonance—but only when the diode is OFF. When the diode is ON, the SRR ceases to resonate, thereby removing its influence on the stopband response. Importantly, each SRR pair (SRR1, SRR2, SRR3) must be switched simultaneously for consistent filter behavior.

This configuration yields seven distinct reconfigurable cases, summarized in Table III-2. The PIN diodes controlling the SRR1 pair are labeled P1, while those on SRR2 and SRR3 are labeled P2 and P3, respectively. These labels reflect the fact that the diodes in each pair switch together.

Table III-2 Possible different cases of the SBF based on ON/OFF PIN diodes combinations.

Cases	P1	P2	P3
011	OFF	ON	ON
101	ON	OFF	ON
110	ON	ON	OFF
001	OFF	OFF	ON
010	OFF	ON	OFF
100	ON	OFF	OFF
000	OFF	OFF	OFF

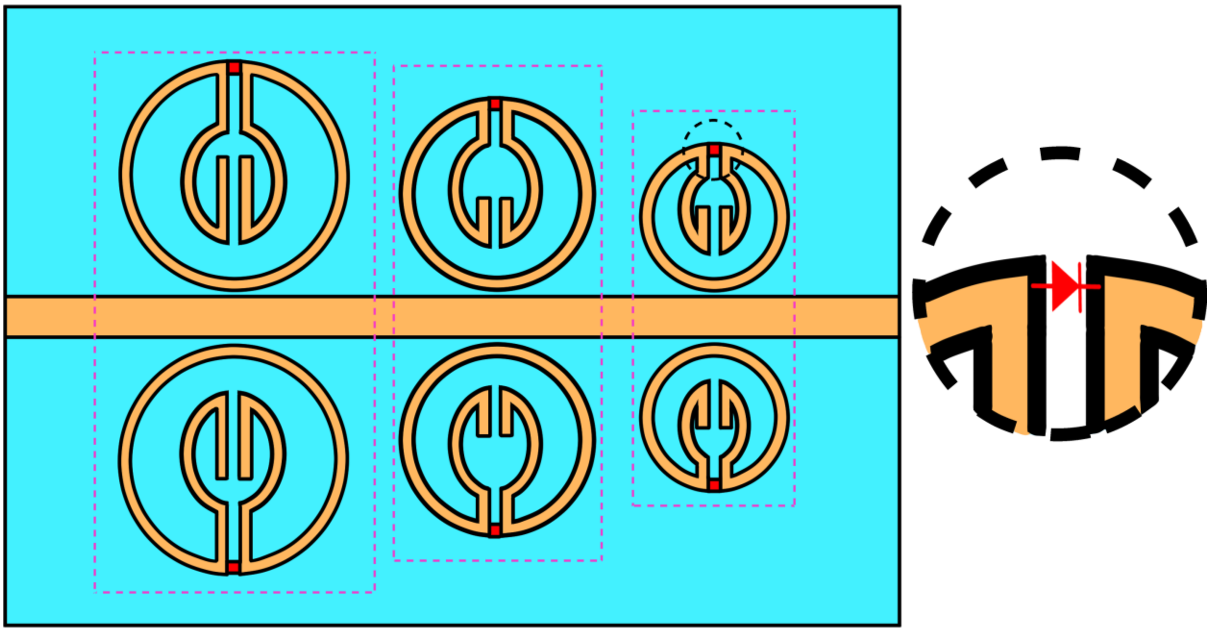

Figure III-15: Top view of the proposed reconfigurable SBF structure loaded with SRR pairs and PIN diodes.

Each pair of SRR unit cells, corresponding to one of the stopbands, can be modeled as an LC resonant circuit. Since inter-pair coupling is negligible, the equivalent circuit of the reconfigurable triple-mode stopband filter (SBF) is shown in Figure III-16.

$$C = \frac{1}{2\pi Z(f_{U-10} - f_{L-10})} \tag{III-14}$$

$$L = \frac{1}{4\pi^2 f_r^2 C} \tag{III-15}$$

Where f_{U-10} and f_{L-10} represent the upper and lower frequencies of the -10 dB stopband bandwidth, respectively. The input impedance of the filter is denoted by Z.

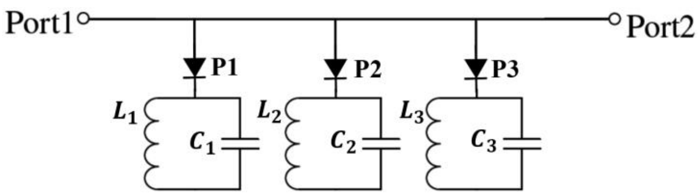

Figure III-16: The equivalent circuit of the proposed tunable SBF.

In addition, the PIN diodes are modeled using their equivalent lumped element representations:

- In the ON state, each diode is represented by a series connection of a resistance and an inductance, reflecting its low-impedance behavior.
- In the OFF state, the diode is modeled by an inductance in series with a parallel RC network, accounting for its high impedance and parasitic effects.

III.4.1. Discussion of the results obtained for the different cases of SBF.

The simulation results presented in Figure III-17, Figure III-18, and Figure III-19 illustrate the performance of the reconfigurable stopband filter across the seven switching cases, as defined in Table III-3. These results confirm the expected stopband behavior of the filter in all configurations, demonstrating its reliable and stable performance.

Importantly, the resonant frequencies remain consistent across all modes—2.0 GHz, 2.5 GHz, and 3.6 GHz—indicating that the reconfigurability does not introduce frequency shifts, and the filter maintains frequency stability during mode switching.

The seven switching cases are grouped into three categories:

1. Single-mode stopband: Achieved when only one SRR pair is active (i.e., one pair of PIN diodes is OFF while the other two are ON). These are cases 011, 101, and 110.
2. Dual-mode stopband: Occurs when two SRR pairs are active (i.e., two PIN diode pairs are OFF and one is ON). These are cases 001, 010, and 100.
3. Triple-mode stopband: Occurs when all three SRR pairs are active (i.e., all PIN diodes are OFF), corresponding to case 000. This is effectively the base state of the filter, equivalent to the configuration without PIN diodes.

Additionally, there's a special case—111—where all diodes are ON, effectively disabling all SRRs. As a result, no stopband behavior is observed in this configuration, confirming the full reconfigurability of the design.

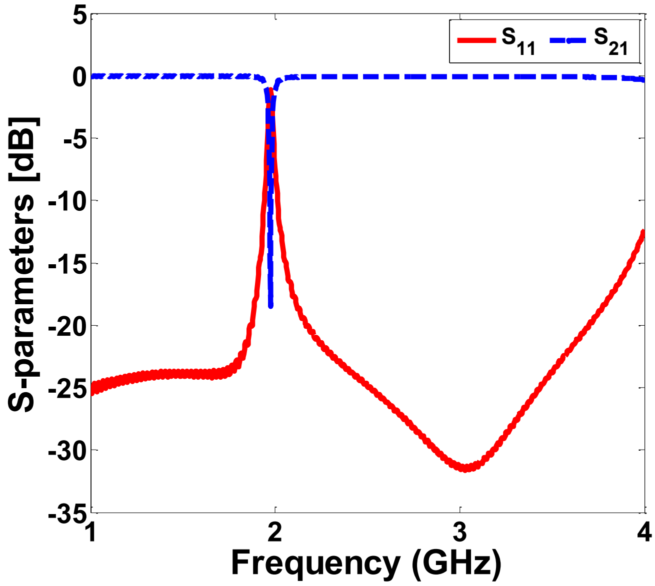
S11
S21
S-parameters [dB]
Frequency (GHz)
5
0
-5
-10
-15
-20
-25
-30
-35
1
2
3
4

(a)

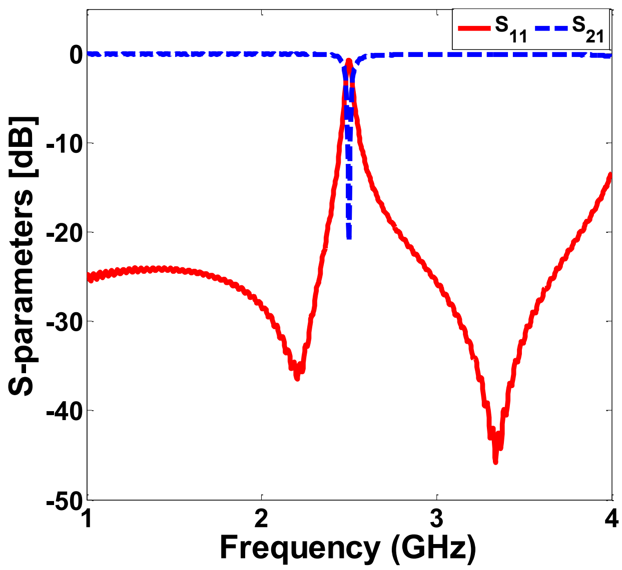
S11
S21
S-parameters [dB]
Frequency (GHz)
0
-10
-20
-30
-40
-50
1
2
3
4

(b)

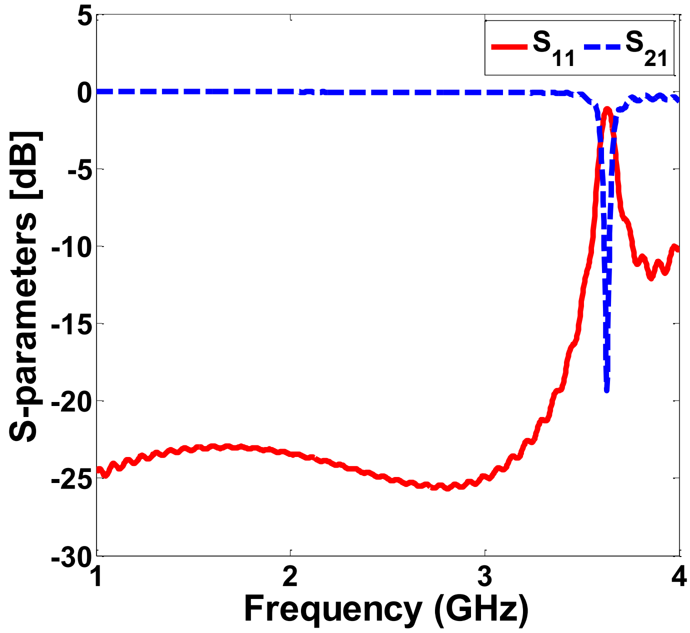

(c)

Figure III-17: Simulated S-parameters of the reconfigurable filter in its single-modes: (a) case 011; (b) case 101; (c) case 110.

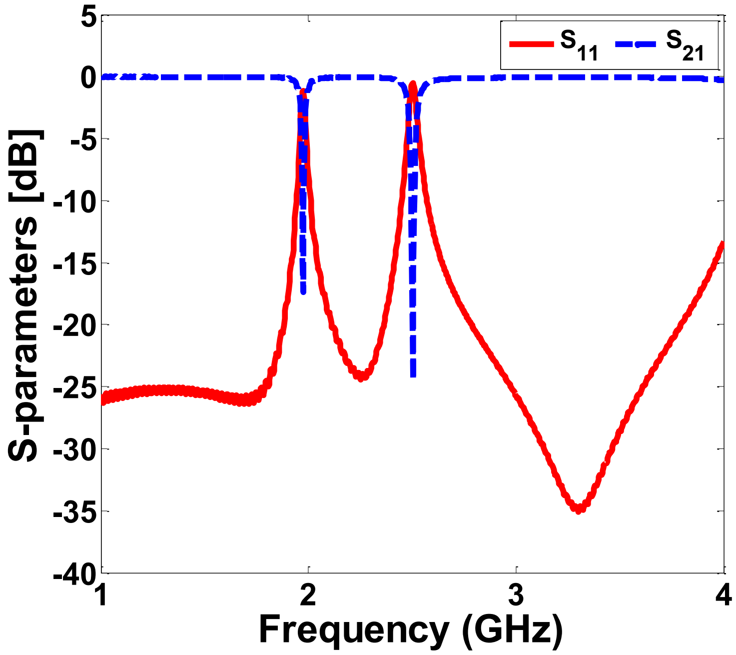

(a)

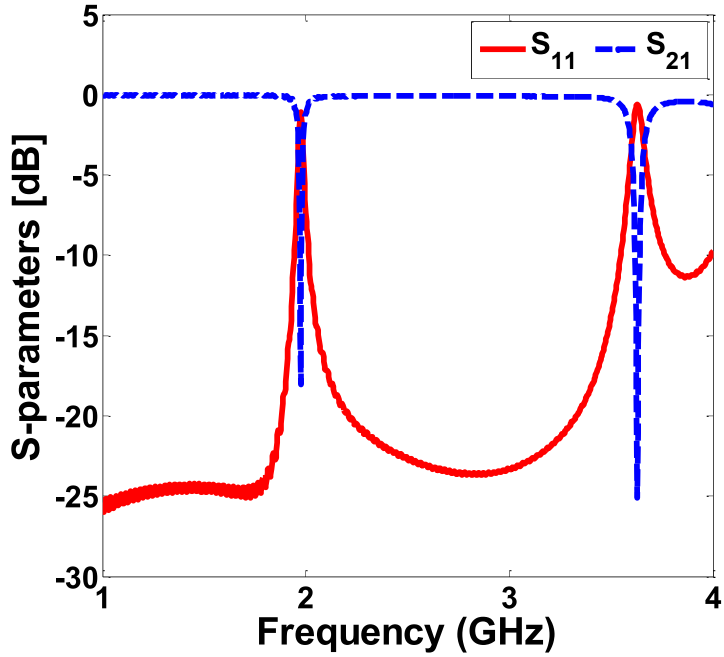

(b)

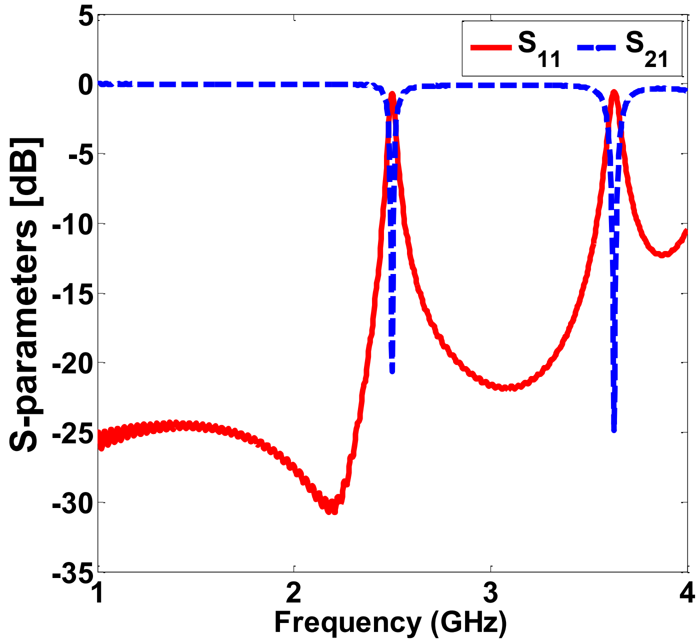

(c)

Figure III-18: Simulated S-parameters of the reconfigurable filter in its dual-modes: (a) case 001; (b) case 010; (c) case 100.

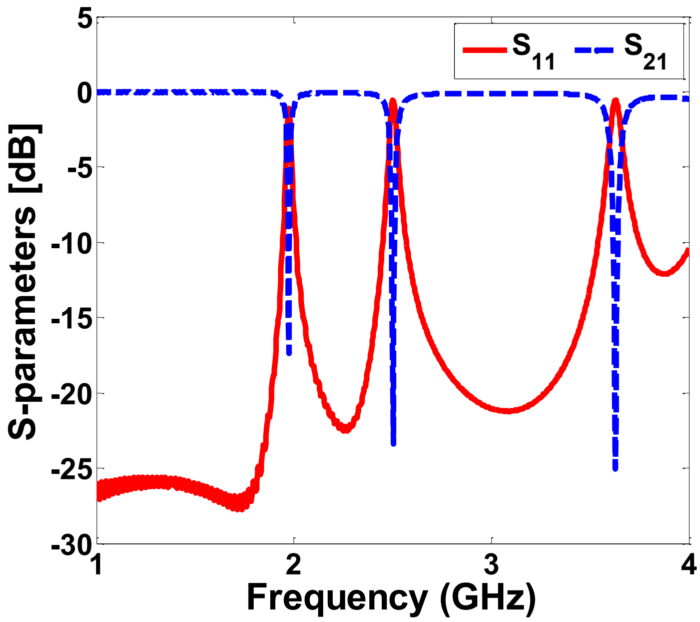

Figure III-19: Simulated S-parameters of the reconfigurable filter in its triple-mode: case 000.

Table III-3 The extracted parameters of the seven cases.

Cases	Resonant frequency (GHz)	Rejection level (dB)	Mode of the filter
011	2.0	-19	Single-band-rejection
101	2.5	-22	Single-band-rejection
110	3.6	-20	Single-band-rejection
001	2.0/2.5	-17 / -24	Dual-band-rejection
010	2.0/3.6	-18 / -25	Dual-band-rejection
100	2.5/3.6	-21 / -25	Dual-band-rejection
000	2.0/2.5/3.6	-17 / -24 / -25	Triple-band-rejection

III.5. Conclusion

In this chapter, a reconfigurable and miniaturized microstrip stopband filter was successfully proposed and analyzed. The compactness of the design was achieved through the integration of novel metamaterial-based SRR (Split Ring Resonator) unit cells, while reconfigurability was realized by incorporating six PIN diodes strategically placed on the filter structure.

The filter was thoroughly optimized, simulated, and evaluated using CST Microwave Studio, targeting three distinct rejection frequencies: 2.0 GHz, 2.5 GHz, and 3.6 GHz. As a result of the reconfiguration mechanism, the filter exhibited seven distinct operating cases, classified into three categories: Three single-mode stopband configurations, three dual-mode stopband configurations, and one triple-mode stopband configuration

Across all these cases, the filter consistently demonstrated excellent electromagnetic performance, maintaining stable resonant frequencies and high selectivity. These characteristics make the proposed filter highly suitable for modern and emerging wireless communication systems that demand compact, flexible, and frequency-agile solutions.

References

[III.1] **J. B. Pendry, A. J. Holden, D. J. Robbins, and W. J. Stewart**, "Magnetism from conductors and enhanced nonlinear phenomena," IEEE Trans. Microw. Theory Tech., vol. 47, no. 11, pp. 2075–2084, 1999, doi: 10.1109/22.798002.

[III.2] **R. Marqués, F. Medina, and R. Rafii-El-Idrissi**, "Role of bianisotropy in negative permeability and left-handed metamaterials," Phys. Rev. B, vol. 65, no. 14, p. 144440, Apr. 2002, doi: 10.1103/PhysRevB.65.144440.

[III.3] **A. M. Nicolson and G. F. Ross**, "Measurement of the Intrinsic Properties Of Materials by Time-Domain Techniques," IEEE Trans. Instrum. Meas., vol. 19, no. 4, pp. 377–382, 1970, doi: 10.1109/TIM.1970.4313932.

[III.4] **W. B. Weir**, "Automatic Measurement of Complex Dielectric Constant and Permeability at Microwave Frequencies," Proc. IEEE, vol. 62, no. 1, pp. 33–36, 1974, doi: 10.1109/PROC.1974.9382.

[III.5] **D. R. Smith, S. Schultz, P. Markoš, and C. M. Soukoulis**, "Determination of effective permittivity and permeability of metamaterials from reflection and transmission coefficients," Phys. Rev. B, vol. 65, no. 19, p. 195104, Apr. 2002, doi: 10.1103/PhysRevB.65.195104.

[III.6] **J. D. Baena et al.,** "Equivalent-circuit models for split-ring resonators and complementary split-ring resonators coupled to planar transmission lines," IEEE Trans. Microw. Theory Tech., vol. 53, no. 4 II, pp. 1451–1460, Apr. 2005, doi: 10.1109/TMTT.2005.845211.

[III.7] **S. N. Burokur, M. Latrach, and S. Toutain**, "Study of the effect of dielectric split-ring resonators on microstrip-line transmission," Microw. Opt. Technol. Lett., vol. 44, no. 5, pp. 445–448, Mar. 2005, doi: 10.1002/MOP.20662.

[III.8] **J. Huangfu et al**., "Experimental confirmation of negative refractive index of a metamaterial composed of Ω-like metallic patterns," Appl. Phys. Lett., vol. 84, no. 9, p. 1537, Feb. 2004, doi: 10.1063/1.1655673.

General conclusion:

General conclusion

This dissertation presents a comprehensive investigation into the design, optimization, and application of novel metamaterial unit cells, culminating in the development of an electronically reconfigurable microstrip stopband filter. The core innovation lies in the proposed metamaterial cells, engineered to offer superior performance characteristics compared to existing structures. Reconfigurability of the filter's operational frequency and mode is achieved through the strategic integration of PIN diodes onto these cells. This approach enables dynamic adjustment of the filter's response while maintaining high performance metrics across various operational states, all within a compact physical footprint. The developed filter demonstrates significant potential for integration into modern wireless communication systems, such as 5G and the Internet of Things (IoT), as well as sophisticated applications including radar and satellite communications.

The research is systematically presented across three chapters. Chapter One lays the foundational groundwork, providing an essential overview of microwave filter theory, common guiding technologies employed in filter design, and a survey of existing techniques for implementing reconfigurable filters. Chapter Two delves into the domain of metamaterials, exploring their historical origins, fundamental classifications (e.g., (ENG), (MNG), (DNG)), and diverse application areas.

Chapter Three constitutes the primary original contribution of this work. It commences with the detailed design and characterization of the novel metamaterial unit cell. Subsequently, it elaborates on the design concept and systematic development steps leading to the final electronically reconfigurable stopband filter incorporating PIN diodes. Each stage of the design process and the underlying operational principles are analyzed in depth. The chapter culminates with the presentation and discussion of simulation results for seven distinct operational cases of the reconfigurable filter, demonstrating its ability to target different frequency bands (specifically 2.0 GHz, 2.5 GHz, and 3.6 GHz) through various diode switching combinations.

Future perspectives and areas for improvement:

The results obtained in this dissertation validate the efficacy of the proposed reconfigurable stopband filter, which successfully leverages metamaterial cells and PIN diodes to achieve dynamic control over its operating mode and resonant frequencies. Nevertheless, several avenues for further enhancement and future research can be identified to advance its performance and expand its applicability:

- **Optimization of reconfiguration mechanisms:** While PIN diodes have proven effective for discrete state switching, the integration of varactor diodes could offer continuous tuning capabilities. This would allow for finer, more granular adjustments of the filter's resonant frequency, enhancing its adaptability to varying signal environments.
- **Development of multi-band filters with enhanced performance:** The current configurations demonstrate single-band, dual-band, and triple-band functionality. Future work could focus on extending this to quad-band or even penta-band operation. This would significantly increase the filter's versatility for complex communication networks and multi-frequency systems, potentially enabling simultaneous operation across a wider array of standards.
- **Application to other reconfigurable microwave components:** The design principles and metamaterial concepts developed herein are not limited to stopband filters. They could be adapted for the design of other critical reconfigurable devices, such as bandpass filters, phase shifters, and elements for smart antenna arrays. Exploring these avenues could lead to compact, high-performance solutions for next-generation telecommunication systems.
- **Extension to millimeter-wave and terahertz frequencies:** As wireless communication technologies advance towards higher frequency spectra, particularly for 5G, future 6G networks, and advanced radar systems, adapting these reconfigurable filter designs for operation in the millimeter-wave (mmWave) and terahertz (THz) bands is a critical next step. This will necessitate careful optimization of cell dimensions, substrate materials, and switching element selection to ensure efficient electromagnetic response and low-loss performance at these higher frequencies.